Crystallization of Complex Inorganic Systems within the Confinement of Miniemulsion Droplets

Dissertation

zur Erlangung des Grades
„Doktor der Naturwissenschaften"
im Promotionsfach Chemie

am Fachbereich Chemie, Pharmazie und Geowissenschaften
der Johannes Gutenberg-Universität Mainz

vorgelegt von

Alice Antonello

geboren in Busto Arsizio, Italien

Mainz, Mai 2017

Dekanin:

1. Berichterstatterin

2. Berichterstatterin

Tag der mündlichen Prüfung: 29.06.2017

Abstract

Nanometric confinement strongly affects crystallization processes. In the small volume of miniemulsion droplets, precursor concentrations are limited and, consequently, the crystal growth is slowed down and smaller crystals are obtained. In an ideal case, each miniemulsion droplet can act as an independent "nanoreactor" because it is stable against molecular diffusion and, therefore, without exchange of material among the droplets, the particles grow only from the initial quantity of precursors. Furthermore, confinement controls the particle size by delimiting the maximum space where the crystallization can occur. This dissertation demonstrates this control of growth and size through the crystallization of ferrites, ammonium phosphomolybdates (APM), and manganites within miniemulsion droplets. All the materials were obtained as nanoparticles with dimensions below 100 nm. Especially, APM nanostructures were three orders of magnitude smaller than analogous samples produced in bulk solution synthesis. Ferrites and manganites were achieved at much lower temperature (i.e., 80 °C and 100 °C, respectively) than generally required and without post-synthesis thermal treatment, most likely because of the combination of nucleation–growth control and of the high Laplace pressure within droplets, consequences of the miniemulsion confinement. To achieve highly crystalline spinel ferrites, the miniemulsion technique was performed under solvothermal conditions. In this case, a synergy between colloidal confinement and higher pressures yielded products with higher crystallinity when compared to the corresponding one synthesized in miniemulsion at ambient pressure and in bulk. The high crystallinity and the controlled particle size influenced positively the functional properties of the materials. Ferrites are well-known ferrimagnetic materials and, in the present work, display superparamagnetic behavior as a result of their nanometric size. Ferrites and ammonium phosphomolybdates were used as active catalysts for epoxidation reactions in organic media because of their enhanced dispersibility in organic solvents and their high specific surface area and porosity. APM catalysts produced in miniemulsion were compared to analogous synthesized from bulk solution, showing much higher values of precursor conversion after only 1 h and better recyclability. Ferrites were also magnetically recoverable from the reaction medium and reusable for several cycles without losing activity.

Kurzfassung

Die Begrenzung im Nanometerbereich wirkt sich stark auf Kristallisationsvorgänge aus. Dank des kleinen Volumens der Miniemulsionströpfchen sind die Vorläuferkonzentrationen begrenzt und dies führt somit zu einem verlangsamten Wachstum der Kristalle, was in kleineren Kristallen resultiert. Im Idealfall kann jedes Miniemulsionströpfchen als eigenständiger „Nanoreaktor" wirken, da es gegen molekulare Diffusion stabil ist. Somit wachsen die Partikel nur aus der Anfangsmenge der Vorläufer, ohne dass es zu einem Materialaustausch zwischen den Tröpfchen kommt. Weiterhin steuert die Begrenzung des Raumes, wo die Kristallisation stattfindet, die Teilchengröße. Diese Dissertation beschreibt diese Kontrolle von Wachstum und Größe durch die Kristallisation von Ferriten, Ammoniumphosphomolybdaten (APM) und Manganiten in Miniemulsionströpfchen. Alle Materialien wurden als Nanopartikel mit einer Größe von unter 100 nm erhalten. Insbesondere waren APM-Nanostrukturen um drei Größenordnungen kleiner als analoge Proben, die „in Bulk" hergestellt wurden. Ferrite und Manganite wurden bei deutlich niedrigerer Temperatur (d.h. 80 °C bzw. 100 °C) und ohne thermische Nachbehandlung erzeugt, wie es normalerweise erforderlich ist. Die Ursache hierfür liegt vermutlich in der Kombination aus der Kontrolle über das Keimbildungswachstum und des hohen Laplace-Drucks innerhalb der Tröpfchen, eine Konsequenz der räumlichen Beschränkung innerhalb der Miniemulsion. Um hochkristalline Spinell-Ferrite zu erhalten, wurde die Miniemulsionstechnik unter solvothermalen Bedingungen durchgeführt. In diesem Fall lieferte die Synergie zwischen kolloidaler Begrenzung und höheren Drücken Partikel mit höherer Kristallinität im Vergleich zu den entsprechenden Produkten einer reinen Miniemulsion bei Umgebungsdruck oder „in Bulk". Des Weiteren hatten die hohe Kristallinität und die kontrollierte Partikelgröße einen positiven Einfluss auf die funktionellen Eigenschaften der Materialien. Ferrite sind als ferrimagnetische Materialien bekannt, zeigen aber in der vorliegenden Arbeit ein superparamagnetisches Verhalten als Ergebnis ihrer nanometrischen Größe. Außerdem wurden diese Ferrite und Ammoniumphosphomolybdate, aufgrund ihrer erhöhten Dispergierbarkeit in organischen Lösungsmitteln, ihrer hohen spezifischen Oberfläche und Porosität als aktive Katalysatoren für Epoxidierungsreaktionen verwendet. Die APM-Katalysatoren, die in

Miniemulsion produziert wurden, zeigten im Vergleich zur analogen Synthese „in Bulk" nach bereits einer Stunde deutlich höhere Werte der Vorläuferumwandlung und eine bessere Wiederverwertbarkeit. Ebenso wurden die Ferrite magnetisch aus dem Reaktionsmedium zurückgewonnen und verloren ihre Aktivität auch nicht nach mehreren Wiederholungszyklen.

Table of Contents

1. Motivation

Crystallization is one of the simplest examples of naturally occurring self-assembly: a highly ordered solid is formed from the infinite, tridimensional, and periodic repetition of units (e.g., atoms, molecules, and ions), from the nanometric to the macroscopic scale.[1]

The ordering process of crystallization creates beautiful structures, such as snowflakes, stalactites and stalagmites, minerals, and gemstones. The artistic beauty of these entities has always fascinated the humankind. Also, the everyday laboratory practice can provide wonderful examples of crystal structures, as it is the case of the crystallization of rhombic dodecahedral ammonium phosphomolybdates (Figure 1.1), described in one of the following sections of this dissertation.
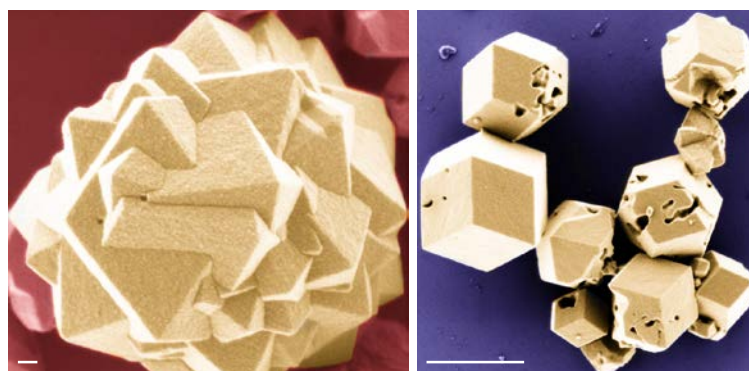
Figure 1.1. Scanning electron microscopy (SEM) images of the ammonium phosphomolybdates samples synthesized by bulk solution synthesis. The scale bar in the left image corresponds to 100 nm and the one in the right image to 1 μm.

Of course, aesthetical value has not been the main reason why crystallization of materials has been pursued and why it is one of the most investigated scientific topics. Important features of the materials are strongly related to crystallinity, as it is the case of mechanical, electronic, magnetic, optical, and catalytic properties.[2] Inorganic materials are generally a clear example of the relation between crystallinity and functional characteristics. In the present dissertation, the synthesis of crystalline complex inorganic systems was pursued to achieve magnetic and/or catalytic properties.

The investigation and the understanding of the crystallization process is decisive to achieve and customize the functional properties of the materials. Although systematic studies on crystallization have been carried out since the 18th century and a set of

"classical" theories is well established, exploring crystallization is still challenging, especially when referring to colloidal systems.[1]

The term *colloid*, according to IUPAC's *Gold Book*, "refers to a state of subdivision, implying that the molecules or polymolecular particles dispersed in a medium have at least in one direction a dimension roughly between 1 nm and 1 μm or that in a system discontinuities are found at distances of that order".[3] From the point of view of crystallization, colloidal systems are significant for different reasons: they can either occur as nanocrystalline products of a reaction, or act as additives (often polymer colloids), playing a role as templates and/or structure-directing agents to control the crystallization of materials. Colloidal systems can be exploited as: (i) hard templates, in which the colloidal particles offer their surface to support the crystallization, and (ii) soft templates, in which colloidal structures (e.g., micelles or emulsion droplets) confine spaces where the crystallization occurs.[4] Regarding the latter templating effect, water droplets of inverse miniemulsions confine nanometric spaces (e.g., average radius of a droplet 100 nm) in which reactions such as reduction of metal salts or precipitation of inorganic compound, and their crystallization take place.[5] Miniemulsion droplets are kinetically stable against coalescence and they are stable against molecular diffusion; therefore, no exchange of material occurs among them and they can be ideally considered "nanoreactors"[6, 7] (Figure 1.2).
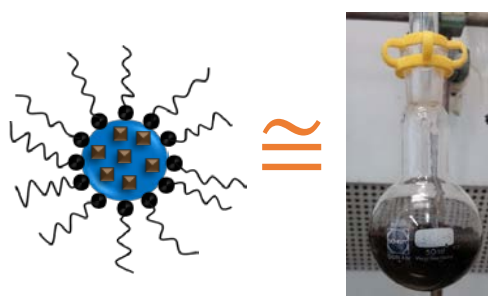
Figure 1.2. Representation of the water droplet of an inverse miniemulsion as nanoreactor compared to a normal laboratory round-bottom flask under reflux.

The confinement provided by miniemulsion droplets has many consequences on the crystallization: (i) it promotes homogeneous nucleation and, for certain systems, can provide conditions for the formation of crystalline phases that are not otherwise achievable under standard conditions, (ii) it controls the crystal growth because of the reduced amount of precursors present inside the droplets and because of the absence of exchange among them, and (iii) it governs the particle size by delimiting the maximum space in

which the crystallization can occur.[5] In this special environment, the synthesis of crystalline inorganic materials can be typically achieved at lower temperature than usually required,[8,9] even at room temperature,[10,11] and without post-synthesis thermal treatment.

In the following, the coprecipitation and crystallization of complex inorganic systems (namely ferrites, ammonium phosphomolybdates, and manganites) within the confined space of miniemulsion droplets will be discussed. The study has the fundamental goal of exploring, firstly, the effects of nanometric confinement on the particle formation and on the crystallization process and, secondly —as in the case of ferrites and manganites— the synergy between the confined space and the non-standard pressure conditions provided by the solvothermal route. Furthermore, the functional properties of the obtained crystalline products were assessed: ferrites and ammonium phosphomolybdates were tested as catalysts for epoxidation reactions because of their considerable dispersibility in organic media and their high specific surface area.

The present dissertation is divided in five chapters. Following the present motivation, Chapter 2 outlines the theoretical basis of crystallization and emulsions, with a focus on miniemulsions, providing a highlight on the crystallization of inorganic compounds in confinement (either physical or colloidal); hydrothermal/solvothermal routes and their application to inorganic synthesis are also explained in the same chapter. The main characterization methods employed to investigate the synthesized materials and their theoretical background are described in Chapter 3. In Chapter 4, the results of the syntheses and of the characterization of the complex inorganic systems are described in detail and discussed. The chapter is divided in three independent sections related to the three different classes of materials addressed. Finally, the experimental details are reported in Chapter 5.

2. Theoretical Background

This section gives a general overview on the theoretical principles behind the work described in this dissertation. A brief description of crystallization processes, confinement, and its exploitation for inorganic synthesis in miniemulsion and solvothermal routes will be provided.

2.1 Crystallization

A crystal is a solid constructed by the highly ordered, infinite, and periodic repetition of identical building blocks (e.g., atoms, molecules, ions) in the three dimensions of the space.[2] The study of crystalline materials has been one of the most investigated scientific topics because important physicochemical properties, such as electronic, magnetic, and catalytic ones, are related to the crystallinity.[2]

2.1.1 Supersaturated Solutions

The crystallization from solution is the formation of a crystal starting from dissolved species (e.g., atoms, molecules and ions). The thermodynamic driving force for crystallization is the supersaturation of a solution. For ionic systems, the saturation level (S) is defined as:

$$S = \frac{IP}{K_{sp}}$$

(2.1)

where IP is the ionic product, the product of the concentrations (or, more correctly, the activities) raised to the power of their stoichiometric coefficients, and K_{sp} is the equilibrium solubility product.[1] The Gibbs free energy for dissolution is given by:

$$\Delta G = RT \ln \frac{IP}{K_{sp}} = RT \ln S$$

(2.2)

$IP > K_{sp} \Rightarrow \Delta G > 0 \Rightarrow$ solution supersaturated

$IP = K_{sp} \Rightarrow \Delta G = 0 \Rightarrow$ solution saturated (equilibrium)

$$IP<K_{sp} \Rightarrow \Delta G<0 \Rightarrow \text{solution undersaturated}$$

Generally, the crystallization from a supersaturated solution includes three steps:

- <u>Nucleation</u>: formation of *nuclei*, starting centers for the spontaneous growth. Primary nucleation refers to systems not yet containing crystalline matter. It can be divided in homogeneous (spontaneous) and heterogeneous (induced by foreign particles). In contrast, the secondary nucleation occurs in the vicinity of crystals already present in solution.[12]
- <u>Growth</u>: deposition of material on the formed nuclei.
- <u>Ripening</u>: larger crystals (less soluble) grow at the expense of the smaller ones (more soluble).

2.1.2 Nucleation

A *nucleus* results from the interactions of ions or molecules, which combine until a stable cluster is reached. The most probable process is not a simultaneous collision of the required units but a sequence of bimolecular additions, until a critical size of the cluster is achieved. The nuclei formation can be thermodynamically described as the energy difference between a solid particle of the solute and the solute in solution. This difference is expressed as:

$$\Delta G = \Delta G_S + \Delta G_V = 4\pi r^2 \gamma + \frac{4}{3}\pi r^3 \Delta G_v \tag{2.3}$$

where ΔG_S is the surface free energy, the energy difference between the surface and the bulk of the particle, a positive quantity; γ is the interfacial tension between the supersaturated solution and the nucleus solid surface; r is the radius of the nucleus; and ΔG_V is the volume free energy, the energy difference between the bulk (supposed as a very large particle, $r\to\infty$) and the solute dissolved in solution, and it is calculated multiplying the volume of a nucleus with ΔG_v, free energy difference for the transition from solution to solid particle per unit volume. ΔG_v is negative in supersaturated solutions and its absolute value is equal to:

$$|\Delta G_v| = \frac{kT \ln S}{v} \tag{2.4}$$

2. Theoretical Background

Where S is defined in eq. (2.1), k is the Boltzmann constant, T is the temperature in Kelvin and v is the volume of a nucleus.

Eq. (2.3) can be described with a curve (Figure 2.1) that has a maximum corresponding to the ΔG_{crit}, the critical nucleation energy, at a certain critical radius r_c.
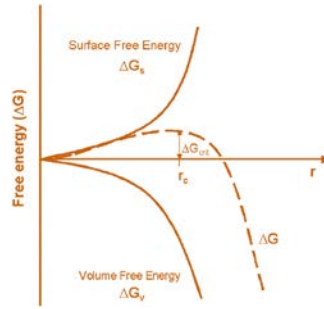
Figure 2.1. Free energy variation during the formation of a crystallization nucleus of radius r.

Differentiating and equating to zero eq. (2.3), the critical radius and the ΔG_{crit} can be calculated as:

$$r_c = -\frac{2\gamma}{\Delta G_v} \tag{2.5}$$

$$\Delta G_{crit} = \frac{16\pi\gamma^3}{3(\Delta G_v)^2} = \frac{4\pi}{3}r_c^2 \tag{2.6}$$

The critical size r_c is the minimum size for a stable nucleus: smaller particles would dissolve and bigger ones would continue to grow, to decrease in both cases the critical nucleation energy.

The nucleation rate J is the number of nuclei formed per unit of time and unit of volume and can be expressed by an Arrhenius-type equation:

$$J = Ae^{-\frac{\Delta G_{crit}}{kT}} \tag{2.7}$$

Substituting eq. (2.4) in eq. (2.6) and then inserting the value of ΔG_{crit} obtained (2.7), J can be calculated as:

$$J = A\exp\left[-\frac{16\pi\gamma^3 v^2}{3k^3T^3(\ln S)^2}\right] \tag{2.8}$$

Accordingly, three parameters are ruling the nucleation: the temperature, the saturation level (*S*), and the interfacial tension.

Generally, it is possible to observe experimentally that, cooling down quickly an aqueous solution of inorganic salts, the first formed crystals are a less thermodynamically stable form. At the end of 19th century, Ostwald provided a generalization of this phenomenon, known as the *Ostwald's rule of stages*:[13] "an unstable system does not necessarily transform directly into the most stable state, but into one that most closely resembles its own, a transient state whose formation implies the smallest loss of free energy".[12] Although this rule does not have any theoretical proof — even if many studies have been performed up to now —[14, 15] and plenty of exceptions are reported, the Ostwald theory points out the importance of kinetics in crystal nucleation and growth. If more than one polymorph is thermodynamically possible, the product is not the most thermodynamically stable but the one with the fastest formation rate.

2.1.3 Growth

After the formation of stable *nuclei*, the crystal growth starts: this process is quite complex to explain and mainly two categories of theories have been developed.[12]

The *surface energy theories* postulate that the shape assumed by a growing crystal is the one that minimize the surface energy. The crystal faces developed are the ones that allow the entire crystal to have the minimum total free energy and the growth rate of the faces is related to their respective surface energy, as theorized by Wulff.[16] This set of theories is quite simplistic and they are not much supported by quantitative proofs; therefore, they are nowadays not anymore accepted.

Another group of theories are the *diffusion theories*. The first contribution to the diffusion theory was made by Volmer[17], who adopted a thermodynamic approach. During the growth, when substance units arrive to the already formed crystal face, they are not immediately integrated into the lattice, but they loosely adsorb to the surface and are free to migrate over it (surface diffusion). A layer of adsorbate is formed and a dynamic equilibrium is established between the layer and the bulk solution: the units connect to the points in which there is the highest attractive force (active sites) and, step by step, the complete face will be covered. To start a new layer and to continue the crystal growth, a *surface nucleus* must be formed: this concept resembles the three-dimensional nucleation

theory, described in the previous section, but it occurs on a surface, thus on a two-dimensional level. The same thermodynamic explanation of the three-dimensional nucleation can be applied to the two-dimensional one. Thus, the free energy barrier and the critical radius for the surface nucleus formation can be calculated.

The free energy of formation for a surface nucleus is:

$$\Delta G = a\gamma + v\Delta G_V = 2\pi r h\gamma + \pi r^2 h\Delta G_v \qquad (2.9)$$

where a and v are the area and the volume of the nucleus, assuming it is a disc of radius r and height h. The critical radius of the surface nucleus can be obtained as for (2.5):

$$r_c = -\frac{\gamma}{\Delta G_v} \qquad (2.10)$$

The surface nucleus has half of the radius of the three-dimensional nucleus (2.5).

The free energy barrier can be calculated as:

$$\Delta G_{crit} = -\frac{\pi h\gamma^2}{\Delta G_v} = \frac{\pi h\gamma^2 v}{kT\ln S} \qquad (2.11)$$

Comparing equations (2.6) and (2.11), it is evident that a certain supersaturation is also required to form surface nuclei but it is lower than the one required to form the three-dimensional nuclei under the same conditions.

The growth layers are described by the theories of Kossel[18, 19] and Stranski:[20] the apparently flat surface of a crystal is, actually, made of layers (called *steps*) of monoatomic height, containing one or more *kinks* (Figure 2.2). Growth units are more easily incorporated into the crystal in correspondence of a kink, hence adding more and more units, the kink moves along the step and the face is covered. A new step is formed by surface nucleation and usually starts at the corner.
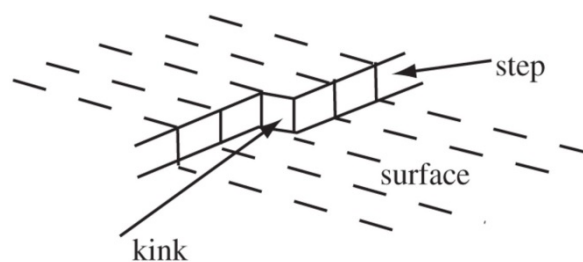
Figure 2.2. Representation of a kink on a single atomic layer step. Figure reproduced from the open source reference 21, http://dx.doi.org/10.1098/rsta.2014.0230, copyright 2015 from the Royal Society publishing.

The formation of a surface nucleus starting a new step should, in principle, require a high supersaturation. However, the growth occurs generally at lower supersaturation than supposed by the theory. Burton, Cabrera, and Frank[22] explained why the growth takes place even at low supersaturation by "recognizing that the crystals that grow are not perfect, and their imperfections (in particular dislocations terminating in the surface with a screw component) will provide the steps required for the growth, making two dimensional nucleation unnecessary".[23]

2.1.4 Ripening

The ripening is the tendency of smaller solid particles dispersed in their own saturated solution to dissolve. Immediately after the dissolution, the solute will deposit on the larger solid particles. The main cause of this phenomenon is the reduction of the surface free energy, achieved reducing the extension of the interfacial area. This process was firstly proposed by Ostwald[13, 24] in 1896 and then called "Ostwald ripening" by Liesegang.[25]

The driving force for the ripening is the difference of solubility between the small and large particles, as given by the Gibbs–Thompson relationship:[12]

$$\ln\left[\frac{c(r)}{c^*}\right] = \frac{2\gamma v}{\nu RTr} \tag{2.12}$$

where $c(r)$ is the solubility of small particles of size r, c^* is the equilibrium saturation for large particles ($r \rightarrow \infty$), γ the interfacial tension, ν are number of ions per formula unit and v is the molar volume of the solute. Considering $\frac{c(r)}{c^*} \approx 1$ because the ripening occurs at very low supersaturation, the Taylor series[1] can be applied:

$$c(r) - c^* \approx \frac{2\gamma v c^*}{\nu RTr} \tag{2.13}$$

If the growth kinetics of the large particles to the detriment of the small ones is a diffusion controlled first order kinetics, the radius change can be calculated by the expression

---

[1] The Taylor series of the natural logarithm when $x = a$ is expressed by:

$$\ln x = \ln a + \frac{x-a}{a} - \frac{(x-a)^2}{2a^2} + \frac{(x-a)^3}{3a^3} - \cdots$$

$$\frac{dr}{dt} = \frac{Dv[\overline{c} - c(r)]}{r} \tag{2.14}$$

where $\overline{c}$ is the average bulk solution concentration and D is the diffusion coefficient. Substituting eq. (2.13) in eq. (2.14) and setting the resultant equation to zero, the critical radius for the Ostwald ripening can be obtained from:

$$r^* = \frac{2\gamma v c^*}{vRT[\overline{c} - c(r)]} \tag{2.15}$$

All particles smaller than this radius will dissolve and all the larger will grow.

2.1.5 Precipitation and Coprecipitation

The IUPAC defines the precipitation as "the sedimentation of a solid material (i.e., precipitate) from a liquid solution in which the material is present in amounts greater than its solubility in the liquid".[3] According to Mullin, the precipitation can be intended as a "fast crystallization",[12] although there are many differences between the two processes.

- The precipitation is a fast process, instead the crystallization is slower. However, both processes are starting from supersaturated solutions and they comprise the same three steps: nucleation, growth, and ripening.

- The precipitation can result either in crystalline or in amorphous products. When crystal are formed, they are quite small due to the fast nucleation.[26]

- The precipitation is generally an irreversible process, the precipitates are virtually insoluble, whereas the products of the conventional crystallization can usually be redissolved at the original conditions of temperature, solvent and concentration (i.e., recrystallization).

- Furthermore, the precipitation process involves *aggregation* soon after nucleation, as well as *ageing*, which includes all the changes of the precipitate after its formation (ripening can be included in ageing). During ageing, the crystallinity of the material can be enhanced, for instance by thermal treatment.

Although precipitation can be induced in several further ways, the most exploited one is by chemical reaction. The product of the reaction has a low solubility (the solubility product, K_{sp}, is low) in the reaction medium and reaches supersaturation quite easily. For example, many hydroxides, carbonates, oxalates, and chalcogenides have very low K_{sp} in aqueous solutions.[27] The precipitation can involve exchange, redox, or hydrolysis

reactions, and can be induced by change of temperature, pressure, concentration, pH, or by the addition of an antisolvent. The nucleation may not occur immediately after the mixing of the two chemicals, but an *induction period* can pass.[12] This event took place, for example, in the case of the precipitation of ammonium phosphomolybdate from different phosphate precursors, described in Section 4.2 of this thesis.

Dealing with complex inorganic systems (e.g., ternary or quaternary oxides) multiple species precipitate simultaneously, and the process is thus called *coprecipitation*. As outlined for the precipitation, also the coprecipitation mechanism is quite complicate to explain,[28] but it has been exploited in recent years for the wet-chemistry preparation of multinary oxides.[27, 29] In particular, the coprecipitation of oxalates has been employed for the synthesis of ferrites: the metal precursors, in the presence of the oxalic acid, form oxalates upon the addition of a precipitating agent (e.g., a concentrated base). The precipitation can be followed by a thermal treatment and/or calcination at high temperature[30] or by low-temperature subcritical hydrothermal processing[31] to achieve the crystalline oxides. The coprecipitation of the oxalates has several advantages, such as the easy formation of precipitates and the homogeneous formation of the oxides upon the degradation of the oxalates. The coprecipitation of the oxalates was performed, in an early stage of the project, for the ferrite synthesis in miniemulsion–solvothermal conditions, as described in Section 4.1. However, this route was abandoned because oxalic acid residues were difficult to eliminate from the products; the coprecipitation of the hydroxides therefore was preferred.

The coprecipitation of the hydroxides occurs immediately after the addition of NaOH concentrated solution to the metal precursors. Amorphous hydroxides precipitate and then redissolved in excess of NaOH. Eventually, the hydroxides of the two metal precursors react together to form the ternary oxide.[32] This strategy was exploited for the synergic synthesis in miniemulsion–solvothermal conditions of ferrites[8] and manganites, as described in Sections 4.1 and 4.3.

2.1.6 Polymorphism and Phase Transition

A crystal may exist in more than one crystalline structure and each of them is called *polymorph*. The polymorphic transition is defined by the IUPAC as "a reversible transition of a solid crystalline phase at a certain temperature and pressure (transition point) to another phase of the same chemical composition with a different crystal structure".[3]

Different polymorphs of the same substance have the same chemical formula, but they can display different types of lattice and shape. This does not just involve a change of the crystal habit (i.e., external shape of an individual crystal, depending on the growth rate of the specific faces[12]), but a change of physical properties, such as density, hardness, melting point, solubility, thermal, electrical, and optical properties. Each polymorph is a separate phase of the considered substance according to the Gibbs phase rule, whereas different crystal habits of that substance are the same phase.[12] Polymorphs can be identified, among several other techniques, by X-ray diffraction, as described in Section 3.1.

Under specific temperature and pressure conditions, except at a transition point, only one polymorph is thermodynamically stable, but metastable phases can form, as stated by the Ostwald's rule of stages (Section 2.1.2). Sometimes the metastable form may display useful properties than the stable form and it can be isolated and dried to avoid phase transition.

Ferrites (generic formula MFe_2O_4) have a cubic crystal structure (space group $Fd\bar{3}m$) as explained in Section 4.1, and they can be "normal" and "inverse" spinels. In normal spinels the ion M having an oxidation state of +II occupies tetrahedral positions in the lattice formed by the oxygen atoms and the ferric ions occupy octahedral positions. In inverse spinels, ferric ions are divided between tetrahedral and octahedral sites and the M ions occupy octahedral sites. Ferrites can also occur as mixed spinels with a certain degree of inversion (see Section 4.1). In this dissertation, the spinel is the only crystalline phase achieved for all the syntheses performed for the ferrites, with different temperature, pressure, and routes.

The ammonium phosphomolybdate crystals have a cubic structure as well, but with a different space group ($Pn\bar{3}m$) and it has a three-dimensional framework, called Keggin structure. They have a characteristic rhombic dodecahedral habit (see Section 4.2).

2.2 Crystallization in Confinement

When referring to crystallization, the confinement is the act of delimiting a closed space where the precipitation and crystallization occur. In this section, the space confinement refers to closed spaces with dimension smaller than a micron.

The thermodynamic and kinetic parameters of crystallization in confinement change dramatically compared to bulk crystallization. For instance, a confined environment can

be created within pores of zeolites[33] or membranes[34], by microfluidic devices[35], or by emulsion droplets (micro- or miniemulsion droplets).[4, 5, 36, 37]The next overview about the different crystallization pathways under confinement does not intend to be exhaustive but to provide some highlights about the variety of the field.

2.2.1 Physical Confinement

Since the beginning of the 20th century, studies on *freezing and melting* of water and small organic molecules in confinement have been performed, exploring the physical transition in capillaries and in porous media (glasses, silicon, zeolites). When the confinement is nanometric the melting and freezing are depressed compared to the bulk.[38]

The *crystallization of small organic molecules* in the nanoscale confinement of membranes and porous glass has been described in a recent review by Jiang and Ward[34]. Nucleation and phase transformation at a scale corresponding to the critical nucleus size dramatically differ from the bulk and metastable polymorphs can be stabilized in such conditions. The properties of the polymorphs synthesized under nanoscale confinement are not appreciably different from the bulk ones, but the confinement, in this case in porous membranes, offers a tool for a systematic control of nucleation, growth, and orientation, by tuning the pore size.[33] For instance, by choosing a certain pore size, a polymorph can be promoted over another one with different critical nucleus size.[34] The stability of the polymorphs and the discover of new ones is a key point in the pharmaceutical research, because the employment of one of the polymorphs instead of the others can affect the rate of dissolution, the solubility and the stability of the final product.

Precipitation and *crystallization* of *inorganic materials* in confinement have not been investigated much compared to freezing–melting and crystallization of organic molecules in confinement. Fiona Meldrum and her group explored this field, creating the nanoconfinement through crossed-cylinder apparatus,[39-41] arrays of picolitre droplets[42], track etched membranes,[43] microfluidic devices,[35] and controlled pore glasses.[44]

The apparatus used to study the crystallization in confinement of calcium carbonate,[39] calcium sulfate,[40] and calcium phosphate[41] was composed of glass half-cylinders mounted in the way that the curved surfaces face each other with orthogonal cylinder axes. The two surfaces were brought gradually in contact increasing the force by a system of screw and

spring and the precipitation occurred in the delimited space between the two cylinders (Figure 2.3).
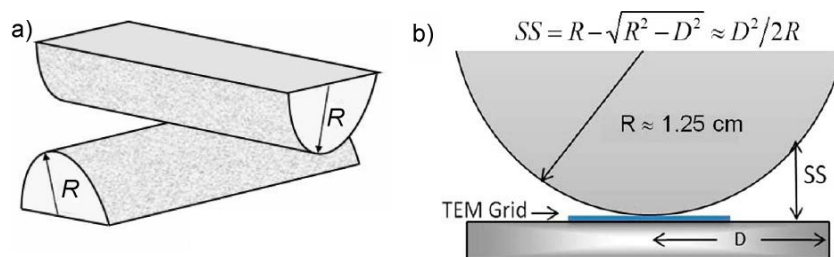

Figure 2.3. (a) Schematic diagram of the crossed-cylinder configuration with radius of curvature *R*. Modified and reproduced with permission from the reference 39, copyright John Wiley and Sons. (b) Schematic drawing of crossed-cylinder apparatus, where *R* is the radius of the half-cylinder, *SS* represents the surface separation between the half cylinders (or the TEM grid placed between the cylinders) and *D* is the distance from the contact point. Reproduced with permission from reference 41, copyright American Chemical Society.

In the case of calcium carbonate, the space constraint led to the stabilization of the amorphous form, because the physical confinement kept the micrometer particles remote from the interface with water and the crystallization of the $CaCO_3$ depends strongly on the presence of water. This effect is more kinetic than thermodynamic and probably it is also exploited by organisms in nature to control the crystallinity of the phases.[39] Differently, for the calcium sulfate in confinement, the stable form was the calcium sulfate hemihydrate instead of the thermodynamically stable calcium sulfate dihydrate (gypsum): this event was probably due to the reduced diffusion of particles that retards their aggregation and, therefore, the formation of the gypsum.[40] For the precipitation of calcium phosphate in confinement, the amorphous calcium phosphate and the octacalcium phosphate were stabilized with respect to the hydroxyapatite (the thermodynamically favored form) probably because of a slower transport of ions, due to a reduced rate of convection.[41] All these experiments demonstrated that the lifetimes of the amorphous precursor phases or of the metastable polymorphs can be extended under confinement.

The crystallization in the confined pores of a controlled pore glass took place more slowly than in the bulk and the transition among the transient polymorphs could be observed, as performed for the potassium ferrocyanide, where even metastable polymorphs were stabilized.[44]

Another physical way to afford confinement was the functionalization of a substrate with a self-assembly monolayer (SAM) of a hydrophobic compound and the subsequent formation of a pattern of hydrophilic and hydrophobic spots by photolithography. In humid conditions, the precursor supersaturated solution condensed as independent

picoliter droplets in the hydrophilic spots. The confinement of the droplets brought to smaller and early stage crystals because the growth was slowed down by the reduced amount of precursor present in the droplets. If the system was fed with new solution the growth continued until the final form. The droplet array was a valuable tool to study the nucleation and growth processes because they are slower compared to the same processes in the bulk.[42]

The crystallization of inorganic materials in the confinement of droplets, intended as "nanoreactors", has been studied in colloidal systems, such as microemulsion and miniemulsion.

2.2.2 Colloidal Confinement: Emulsions

A colloidal system is defined by IUPAC as a dispersion in a medium of "particle or polymolecular particles with at least in one direction a dimension roughly between 1 nm and 1 μm".[3] Colloidal assemblies, such as emulsions, microemulsions, and miniemulsions, can be employed to confine the synthesis of inorganic materials.

An *emulsion* (called also *macroemulsion*) is a thermodynamically unstable dispersion of a liquid (disperse phase) as droplets in another immiscible liquid (continuous phase). If the continuous phase is water and the disperse phase an organic apolar solvent, the emulsion is an oil-in-water (O/W), direct, emulsion; the opposite case is the water-in-oil (W/O), inverse, emulsion.[45] They are kinetically stabilized by a suitable surfactant. The droplet size is between 0.1 and 10 μm.

Microemulsions are thermodynamically stable dispersions of liquid droplets in another immiscible liquid, being formed spontaneously, differently from the macroemulsion. They are stabilized by a high concentration of surfactant (above the critical micelle concentration, CMC) and by the presence of a cosurfactant (i.e., chemical compound, generally an aliphatic alcohol, whose molecules go between one surfactant unit and the other to improve the surface coverage of the droplets). The droplet size can range between 10 and 100 nm.[46] Inverse microemulsions are called sometimes "reverse micelles":[36, 47] the main difference between microemulsions and reverse micelles is that inverse microemulsions are composed only by micelles containing a large amount of water in their core, while the reverse micelles can also not contain any solvent inside their confinement.[48]

2. Theoretical Background

Miniemulsions are kinetically stable emulsions with a droplet size between 50 and 500 nm. The formation of a miniemulsion, differently from macro- and microemulsion, requires high shear forces, usually provided by ultrasonication or high-pressure homogenization, and after the homogenization a "steady state" is reached.[5, 7]

2.2.3 Emulsion Stability

The colloidal stability of emulsions is a key point to understand the difference between microemulsions and miniemulsions and why miniemulsions act ideally as "nanoreactors", as described in the dissertation.

The destabilization of the emulsions is caused by two mechanisms.

- *Coalescence*: collision and merging of the droplets to reduce the extension of the area of the interfacial contact a and lower the high surface free energy ($\Delta G = \gamma \Delta a$) of the emulsion. To reduce the coalescence, the surface tension (γ) can be lowered by adding a surfactant to the system.
- *Molecular diffusion* and *Ostwald ripening*: diffusion of material from the smaller droplets to the bigger ones. This progressive disappearance of the smaller droplets can be stopped by adding an osmotic pressure agent.[49]

(a)

(b)
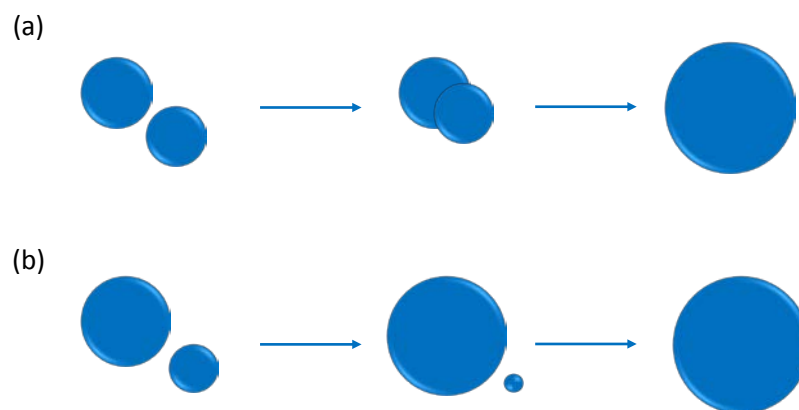
Figure 2.4. Schematic representation of (a) coalescence and (b) Ostwald ripening.

2.2.3.1 Surfactants

Surfactants (*surface active agents*) are molecules that lower the surface tension of the medium in which they are dissolved and/or the interfacial tension with other phases, since they positively adsorb at the interfaces.[3] Surfactant molecules are amphiphilic: they are formed by a hydrophilic part (a polar "head", ions or polar groups) and a hydrophobic part (a hydrophobic "tail, such as hydrocarbon chains).[50]

The classification of surfactants is based on the nature of their hydrophilic part.

- *Ionic surfactants*: they have an ionic hydrophilic group and they usually provide electrosteric stabilization. If the polar head is an anion, for instance a sulfate anion as in the very common sodium dodecyl sulfate (SDS), they are *anionic*. If the group is a cation, such as a trimethylammonium as in the equally common cetyltrimethylammonium bromide (CTAB), they are *cationic*.
- *Non-ionic surfactants*: their hydrophilic part can be a polyether (PEO, PPO), a polyethylene glycol, a polyester of triglyceride, a polyglucoside or a block copolymer and their stabilization is mostly steric.

Surfactants, solubilized in a liquid, tend to self-assemble to reduce the contact of the hydrocarbon chains (or of the hydrophilic heads) to the water (or to the organic solvent). At low concentration, the surfactant molecules are dispersed in the solvent and the surface tension is quickly reduced, as shown in Figure 2.5 for the case of pure water and ionic surfactant. Increasing the concentration, the surface tension continues to decrease until the critical micellar concentration (CMC) is reached. At the CMC, the surfactants self-assemble in *micelles*, structures containing about 50–100 molecules, depending on their molecular structure. If the surfactant is dispersed in water, the hydrophobic tails form a hydrophobic core inside the micelle and the hydrophilic heads remain outside in contact with the water (Figure 2.5); instead in the case of an organic solvent is the other way around (reverse micelles). Micelle formation is spontaneous and entropically favored.[46, 50, 51]
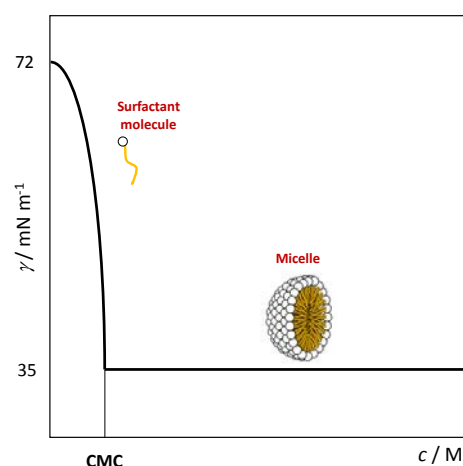

Figure 2.5. Schematic representation of the decrease of the water surface tension in function of the ionic surfactant concentration. Before the CMC, the surfactant is present as molecules, after the CMC, as micelles. The figure of the micelle is from Wikipedia, public domain.

To stabilize the emulsions against coalescence, the selection of the right surfactant is crucial. Surfactants can be either O/W or W/O emulsifiers depending on the ratio between their polar and apolar part. The stabilization of the emulsions is generalized by the *Bancroft's rule*: "the phase in which the surfactant is more soluble is the continuous phase".[45] Therefore, for O/W (direct) emulsions a surfactant with a prevalent polar part is required and for W/O (inverse) emulsions instead a one with a greater apolar contribution is needed.

The selection of the most suitable surfactant may be guided by an empirical parameter, the *hydrophilic–lypophilic balance* (HLB), a typical value for each surfactant, proposed by Griffin,[52] for non-ionic surfactants:

$$HLB = \frac{20 \cdot M_h}{M} \tag{2.16}$$

where M_h is the molar mass of the hydrophilic part and M the total molar mass of the surfactant. For non-ionic surfactants, the HLB is comprised between 0 and 20: from 3 to 8 the surfactants are W/O emulsifiers while between 8 and 18 are O/W emulsifiers. For ionic surfactants, eq. (2.16) is not valid and Davis proposed an incremental method:[53]

$$HLB = 7 + \sum m \cdot H - \sum n \cdot L \tag{2.17}$$

where H and L are empiric tabulated values relative to the hydrophilic and lypophilic parts, respectively, and m and n the number of those groups in the surfactant molecule. For instance, SDS (sodium dodecyl sulfate) has one $-SO_4^{2-}$ group with H of 38.7 and twelve $-CH_2$ groups with an L of 0.47 each. Therefore, the total value is 40, with a stronger polar contribution, as expected.

One of the differences between micro- and miniemulsion is the amount of surfactant required for the stabilization against the coalescence. In the case of microemulsions, the surfactant concentration is well above the CMC and a cosurfactant is generally added: the interfacial tension is close to zero. The droplets are in equilibrium and they can coalesce and exchange material. In contrast, for miniemulsions, the surfactant concentration is always lower than the CMC and, therefore, no micelles are present. The droplets are not fully covered by the surfactant molecules, and the interfacial tension is thus higher than zero.[7] The miniemulsion system is critically stabilized against coalescence.[54]

2.2.3.2 Ostwald Ripening and Osmotic Pressure Agent

The phenomenon of the Ostwald ripening has been already described in Section 2.1.4 as a step during the crystallization process. Referring to emulsion stability, Ostwald ripening is the molecular diffusion of material from the smaller to the bigger droplets, which, eventually, causes the disappearance of the smaller droplets.[6, 49] The phenomenon is a consequence of the *Laplace pressure* that is the pressure difference between the inside and the outside of a curved surface

$$\Delta P_{\mathrm{L}} = P_{\mathrm{inside}} - P_{\mathrm{outside}} = \frac{2\gamma}{r} \tag{2.18}$$

The Laplace pressure (eq. (2.18)) depends on the interfacial tension γ between the two phases (in the case of the emulsions, the two immiscible liquids) and on the radius of the curved surface (for emulsions, the droplet radius). The smaller the droplets are, the higher will be the pressure: the molecular diffusion occurs from the smaller droplets with high ΔP_L to the bigger droplets with lower ΔP_L. If all the droplets of an emulsion had the same radius, the Laplace pressure would be equal for each one and no molecular diffusion would take place.

In emulsions the Ostwald ripening can be counterbalanced by adding a third component, soluble in the disperse phase but not in the continuous.[55] The third component (called *osmotic pressure agent*) provides an osmotic pressure that counteracts the Laplace pressure, therefore the system can be considered metastable or fully stable.[56, 57]

To understand better the stabilization mechanism, we can consider the case of a direct emulsion, styrene/water and hexadecane as osmotic pressure agent. Styrene droplets are generally polydisperse and styrene diffuses from smaller droplets to the bigger ones through the water (continuous phase). Decreasing the droplet size, the Laplace pressure consequently increases. Hexadecane is much less soluble in water than styrene and does not diffuse, thus its concentration increases in the smaller droplets with the diffusion of styrene: the concentration difference will produce a pressure difference, called osmotic pressure (eq. (2.19)):

$$\pi_{osm} = P_1 - P_2 = RT(c_1 - c_2) \tag{2.19}$$

Where P_1 and P_2 are the pressure experienced by the small and the big droplets and c_1 and c_2 the hexadecane concentration in small and big droplets. The Laplace and the osmotic

pressure are balancing each other and the droplets reach a "steady state", their size changes much slower and their molecular diffusion is hindered.[54, 58] The overall pressure is, however, not zero because the Laplace pressure is higher than the osmotic: the droplets are metastable and experience a pressure. The presence of pressure can have consequences on crystallization as reported by us[8] and in Sections 4.1, 4.2, and 4.3.

Microemulsions, as already stated in the previous section, generally require a surfactant concentration well above the CMC. Consequently, the interfacial tension is almost zero. The Laplace pressure and the Ostwald ripening are negligible.

Miniemulsion droplets are ideal "nanoreactors" because they are kinetically stabilized against coalescence (see Section 2.2.3.1) and are fully stabilized against Ostwald ripening by adding the osmotic pressure agent. Non-compensatory exchange of material between the droplets does not happen. In the case of direct miniemulsions, a hydrophobe is added to the oil (commonly hexadecane), instead for the inverse miniemulsions a lyphobe is employed (a ionic compound, salts or sugars).[7] In the inverse miniemulsions described in the following, the inorganic precursors dispersed in the water droplets were also acting as osmotic pressure agents.

2.2.4 Colloidal Confinement: Microemulsion

The droplets of microemulsion can confine space in which chemical reactions can take place.[36, 59] Inorganic precursors are more soluble in water, so inverse microemulsions are generally selected for inorganic synthesis ,[60] even if there are examples of synthesis with O/W microemulsion, as performed by Sanchez-Dominguez et al.[61-63]

If the solution constituting each droplet is supersaturated, the crystallization takes place inside them. The supersaturation can also be reached by chemical reaction, mixing two microemulsions, one containing the inorganic precursors and the other containing the precipitating agent. Microemulsions are dynamic systems: collision and coalescence happen continuously, so that exchange of material between the droplets occurs. Cooper and her group deeply studied the control of the crystallization in the confinement of microemulsion[37, 48, 64] and they theorized a model describing the phenomenon. They stated that, due to the space confinement and the reduced amount of material (ascribed to the reduced space and to the slow intermicellar exchange), the crystallization occurs under thermodynamic control, instead of the usual kinetic control. The Ostwald's rule of stage is

not respected in this case and the most stable polymorph is immediately produced.[65] In microemulsion, homogeneous nucleation is more prevalent than the heterogenous one (opposite to the bulk), because the droplets are too small to contain a foreign material. The reduced amount of material slows down the process, as observed also for the physical confinement (Section 2.2.1). Different compounds, for which the achievement of the stable polymorph was difficult, could crystallize within this confinement: in all cases, the stable polymorph was obtained, but, metastable polymorphs also crystallized by increasing the supersaturation.[66] Therefore, only the initial high supersaturation played a role: the initial high supersaturation ensured that the energy for the formation of all the polymorphs was low, but, after the formation of the nuclei, the supersaturation decreased, the growth was impeded, and the polymorph formed at first was stable. By tuning supersaturation, different polymorphs can be obtained.[48]

Microemulsion has been employed for the synthesis of metal nanoparticles by reduction of the metal salts, as carried out by Boutonnet's [67] and Pileni's[36, 68] groups. Pileni's approach employs anionic surfactants with the metal to be reduced as counterions. Metal oxides are suitable to be prepared through microemulsion to ensure a better size control.[69] Sol–gel synthesis can be coupled with microemulsion, for instance to synthesize titanium dioxide,[70] although the products are usually amorphous. Ferrites were achieved in microemulsion through hydroxide precipitation both in W/O and O/W microemulsion by Sanchez-Dominguez et al.[63, 71, 72]

2.2.5 Colloidal Confinement: Miniemulsion

As stated above, the miniemulsion droplets offer a confined reaction environment:

- The droplets can be considered ideal nanoreactors and no exchange among the droplets occurs. Thus, the particle growth is controlled by the starting amount of material present in the confined space.
- The droplet confinement controls the particle size.
- The confinement and the surfactant stabilization can prevent the large-scale aggregation.
- The nucleation and the crystallization processes can be influenced by the confined environment, as already described for the physical confinement and the microemulsion.

2. Theoretical Background

Miniemulsions have been mainly employed for polymerization, encapsulation, and the synthesis of hybrid materials, but their application for inorganic crystallization is not so widespread, despite the big potentialities.[4, 5]

As reported for the microemulsion (see Section 2.2.3), *melting* and *freezing* were investigated in miniemulsion as well.[73] Montenegro et al. studied the crystallization of hexadecane in direct miniemulsion and of NaCl in the inverse miniemulsion. For both systems, the crystallization (freezing) temperature decreased compared to the bulk, due to the suppression of the heterogeneous nucleation. The required undercooling was higher, reducing the droplets size.

The crystallization of inorganic systems in miniemulsion has been studied since the beginning of the 21st century by Landfester and her group. Inorganic nanoparticles were produced by inverse miniemulsion: the disperse phase was comprised of molten salts, metals or concentrated salt solutions.[74] Cooling down the molten salts, recrystallization occurred or precipitation took place by adding a precipitating agent.

Inverse miniemulsion droplets can act as nanoreactors for *sol–gel synthesis* with water-soluble precursors. Titania has been prepared by sol–gel in inverse miniemulsion by using titanium glycolate as a precursor. Spherical porous and crystalline anatase nanoparticles were obtained at 100 °C with an average size of 200 nm, without calcination, differently from the bulk synthesis and from microemulsion, which require an annealing temperature at least of 300 °C for achieving the crystallinity.[75] Tuning the droplet size with the variation of the surfactant concentration, the crystallite size could be adjusted. Ceria nanoparticles were synthesized from cerium nitrate.[76]

Precipitation or *coprecipitation* can occur in the droplets of the miniemulsion after addition of a precipitating agent (directly or through mixing with a second miniemulsion) and a second ultrasonication step to trigger the fission and fusion of the droplets, for instance for the synthesis of ZnO,[10] ZnS,[77] and CaF_2[11] at room temperature. The inorganic precipitation can occur at the droplet interface producing hollow particles, as performed by our group for zirconium and hafnium hydroxides (amorphous at room temperature),[78] cerium and iron oxides (crystalline at room temperature)[79] and copper oxide (crystalline and pure phase at 80 °C).[9] The precipitation occurs at the interface because the precipitating agent (i.e., triethylamine) is soluble both in the continuous and in the disperse phase.

Inverse miniemulsion droplets have been exploited in this thesis as nanoreactors for the synthesis of ferrites, ammonium phosphomolybdates, and manganites. For all those systems, the confinement of the droplets provided spatial and material control on the particles growth and, furthermore, a Laplace pressure acting on the system can enhance the crystallinity. The residual surfactant functionalization improved the particle processability.

2.3 Hydrothermal and Solvothermal Synthesis

The term "hydrothermal" has a geological origin since it was used for the first time in the 19th century to describe the action of water at high temperature and pressure, leading to the formation of rocks and mineral in the Earth's crust.[80] Afterwards, the term broadened its meaning, referring not only to a natural mechanism, but also to a chemical processing

A solvothermal synthesis is defined as "a homogeneous or heterogeneous chemical reaction in a solvent above room temperature and a pressure greater than 1 atm". [80, 81] If water is employed as solvent, the process is called "hydrothermal".

Hydrothermal conditions can be achieved by using different kinds of experimental setups, in which temperature and pressure can be tuned.

In a sealed vessel, the solvent is heated and the pressure of the system increases. This *autogenous pressure* is produced by the solvent evaporation. For chemical reactions, stainless steel closed vessels containing a Teflon liner (i.e., *solvothermal bombs*) are employed to achieve autogenous pressure. The autogenous pressure is dependent on the nature of the solvent, the heating temperature, and the filling ratio of the vessel. The filling ratio of the vessel is the ratio between the total volume of the reactor and the volume occupied by the reaction mixture (e.g., solvents and precursors).

The pressure can also be increased independently from the heating, adding a gas from an external source. In this case, autoclave reactors are more sophisticated than simple closed vessels and are equipped with a gas inlet and a manometer. Typically, those devices are provided with a heating body regulated by a digital controller, to set a temperature and a heating ramp.

Figure 2.6. Reactors for solvothermal processing: (a) solvothermal bomb and (b) autoclave reactor with gas inlet and temperature–pressure monitoring.

Under pressure, the solvent and its vapor are simultaneously present even if the temperature is above the boiling point at ambient pressure. Under this non-standard condition, the physical properties of the solvents change: viscosity, density, ionic product, and dielectric constant are significantly different. For instance, the water at ambient pressure (1 bar = 0.1 MPa) has a boiling point at 100 °C and with the phase transition liquid–gas, the density, the viscosity, and the dielectric constant suddenly drop. Instead at 10 bar (1 MPa), the water remains liquid well above the boiling point (it is still liquid at 180 °C); therefore, the density, viscosity, and dielectric constant are comparable to lower temperatures and the water behaves like a less polar solvent.[60] Chemical compounds scarcely soluble under ambient conditions are dissolved under these conditions, enabling the subsequent crystallization from the solution and reactions normally not allowed.[82, 83]
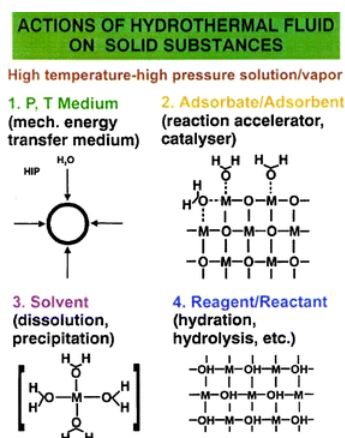

Figure 2.7. Action of hydrothermal fluids on solid substances. Reprinted with permission from ref. 84. Copyright Springer Science + Business Media, LLC.

The obtained solution is supersaturated and the nucleation–growth mechanism starts. The crystallization would be less probable under conventional conditions and single crystals or polycrystalline samples can be achieved.[84] Solvothermal/hydrothermal inorganic syntheses

occur at much lower temperature than required by the solid-state routes and afford crystalline materials without post-synthesis thermal treatment, differently from other low-temperature wet chemistry routes, such as sol–gel and coprecipitation.[27, 83]

All the reactions described in the dissertation were performed under *subcritical* solvothermal conditions, namely the temperature and the pressure are below the critical point of the solvent. The critical point for water is at 647 K (374 °C) and 22.06 MPa (220.6 bar) and for cyclohexane 554 K (281 °C) and 4.07 MPa (40.7 bar). *Supercritical* fluids (above the critical temperature and pressure) show both liquid and gas properties: they have the diffusivity of a gas and the solvating power and density of a liquid.[27]

Subcritical solvothermal conditions have been combined with the inverse miniemulsion route for the synthesis of the ferrites (see Sections 4.1 and 6.1). Experiments were performed under autogenous pressure, employing solvothermal bombs, and under argon pressure inserted in the autoclave from an external source. In the case of the autoclave equipped with the manometer, the pressure was constantly measured during the reactions; instead, for the bombs the autogenous pressure was unknown. To estimate the autogenous pressure, calculations based on the *Antoine equation*[85] were carried out.

The inverse miniemulsion under solvothermal conditions is a complicate system: two solvents are present and they have different boiling points. Furthermore, the reaction temperature is 80 °C, very close to the boiling point of cyclohexane (i.e., 80.75 °C).

To simplify the calculation the amount of water (about ¼ of the total miniemulsion) and the NaOH solution were neglected and, for approximation, the only components considered to contribute to the total pressure were the cyclohexane vapor pressure at 80 °C and the air pressure at 80 °C.

The cyclohexane vapor pressure at 80 °C was assessed by the Antoine law:

$$\log P = A - \left(\frac{B}{C + T}\right) \tag{2.20}$$

Where A, B and C are constant specific for each substance in a certain range of temperature. According to the NIST data bank,[86] for the cyclohexane in the range 323-523 K the constants are $A = 4.13983$; $B = 1316.554$; $C = -35.581$. Therefore, the vapor pressure is $P = 0.987$ bar.

2. Theoretical Background

The moles of air at room temperature (25 °C) and ambient pressure (1 atm) in the closed reactor (45 mL) were calculated with the universal gas law, assuming as free volume of the reactor, occupied by air, the total volume minus the volume of cyclohexane, water and NaOH solution:

$$n_{\text{AIR}} = \frac{P_{\text{atm}} V_{\text{free}}}{RT} \tag{2.21}$$

The moles of air do not change at 80 °C, instead the partial evaporation of the cyclohexane varies the free volume inside the reactor, and hence, the moles of cyclohexane gas at 80 °C should be determined with the universal gas law to obtain the cyclohexane gas volume and the free volume in the reactor at 80 °C:

$$n_{\text{CH gas}} = \frac{P_{\text{CH 80°C}} V}{RT} \tag{2.22}$$

$$V_{\text{CH gas}} = \frac{n_{\text{CH gas}} \cdot MW_{\text{CH}}}{\rho_{\text{CH 80 °C}}} \tag{2.23}$$

$$V_{\text{free 80 °C}} = V_{\text{reactor}} - V_{\text{CH}} + V_{\text{CH gas}} - V_{\text{water}} - V_{\text{NaOH}} \tag{2.24}$$

$$P_{\text{AIR 80 °C}} = \frac{n_{\text{AIR}} RT}{V_{\text{free 80°C}}} = 1.19 \text{ bar} \tag{2.25}$$

In eq. (2.22), V is the volume of the reactor minus the volume of water and NaOH. The total pressure inside the reactor containing the inverse miniemulsion at 80 °C is:

$$P_{\text{TOT}} = P_{\text{CH 80°C}} + P_{\text{AIR 80 °C}} = 2.18 \text{ bar} \tag{2.26}$$

The autogenous pressure is more than double than the atmospheric pressure. The nickel ferrite synthesis required 100 °C. Consequently, the autogenous pressure in that case was 3 bar. The autogenous pressure, in cooperation with the Laplace pressure acting in the water droplets of the inverse miniemulsion, had evident effects on the crystallization of the ferrites, as described in Section 4.1.

3. Characterization Methods

In the present chapter, the theoretical principles and the applications of the employed characterization methods will be described. Only the most relevant techniques will be introduced.

3.1 X-ray diffraction (XRD)

3.1.1 Theoretical Background

Wilhelm Röntgen discovered X-rays in 1895. During the first decade of the 20th century, the most eminent physicists of the history investigated their nature as electromagnetic waves or photons. In 1912, Max von Laue discovered that X-rays can be diffracted on crystals, confirming that they behave as electromagnetic waves. From von Laue's discovery, X-ray diffraction has been exploited to develop a physicochemical technique for studying the structural characteristics of materials, mainly crystalline.

The physical phenomenon is based on the diffraction of waves striking against objects: X-rays are electromagnetic waves scattered by the regular array of electrons (the "scatterers") in a crystal. The elastic scattering produces secondary waves that interfere one with the others: in most the directions are cancelling each other (destructive interference) but in few specific directions are adding each other (constructive interference). The specific directions of constructive interference are determined by the Bragg's Law[87] (eq. (3.1) and Figure 3.1):

$$n\lambda = 2d \sin\theta \qquad\qquad (3.1)$$
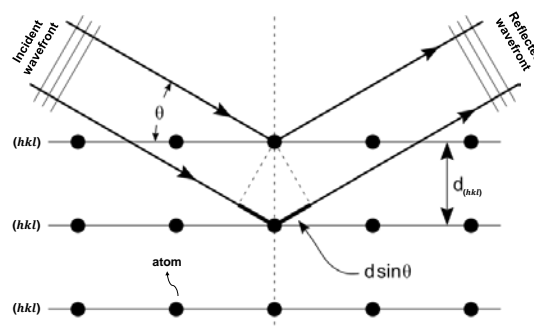
Figure 3.1. Crystalline lattice and Bragg's Law.

3. Characterization Methods

The monochromatic beam of wavelength (λ) is incident on a family of parallel crystalline planes, distant each other d, with an incident angle θ. The constructive interference occurs only when the path-length difference among waves scattered by subsequent different planes is equal to an integer multiple (n) of λ.[87, 88] X-rays are diffracted by crystals because their wavelength is comparable to the interatomic distances in a crystalline lattice, usually between 1–100 Å.

The set of crystalline planes is conventionally identified by three integers, the Miller indices (hkl) (Figure 3.1). Given a crystalline lattice, a unit cell is the smallest unit of the lattice that, repeated in the three dimensions of the space, builds the entire crystal: the sides of the unit cell are called crystallographic axis (commonly a, b, c, and α, β, γ the angles defined by their directions) and the vertices of a unit cell are occupied by atoms or molecules or ions. The Miller indices can be defined as the reciprocal intercepts of the planes with the crystallographic axis.[88] In the case of cubic crystals, $a = b = c$ and $\alpha = \beta = \gamma = 90°$, the spacing between the parallel planes defined by the (hkl) is:

$$d_{hkl} = \frac{a}{\sqrt{h^2 + k^2 + l^2}} \tag{3.2}$$

The eq. (3.2) (and the relative equations for other structures different from cubic) relates the d-spacing of the planes with the cell parameters and, from the Bragg's Law (3.1), d is also function of θ, the diffraction angle. θ identifies the specific directions of constructive interference, which appear as a spot on the diffraction pattern (Figure 3.2) and they are called reflections. These are the signals in the diffractogram, the plot in which the diffracted intensity I is function of θ. Therefore, in a diffractogram the positions of the reflections are defined by θ and at the same time by d: from the reflection positions the unit cell parameters can be determined. Therefore, a diffractogram contains the information about the three dimensional arrangement of atoms in crystals.

3.1.2 Instrumentation, Acquisition of the Data, and Applications

X-ray diffraction can be employed to study single crystals or polycrystalline powders; however, the physical phenomenon is different. A single crystal produces only one family of reflections in the diffraction pattern because it owns only one family of planes that fulfills the Bragg's law (e.g., all the planes ($h00$)). Instead, a polycrystalline powder contains thousands of crystallites (i.e., coherently scattering domains), casually oriented in the space, therefore, for every set of planes there will be a percentage of crystallites

properly oriented to diffract and the diffractogram will be composed of many reflections. The diffracted X-rays emerge as cones from the polycrystalline sample and when they are collected on a flat plate detector they produce diffraction rings (i.e., Debye rings) instead of discrete spots, as for the single crystal (Figure 3.2).


Single crystal diffracted beam   Polycrystalline powder diffraction cone
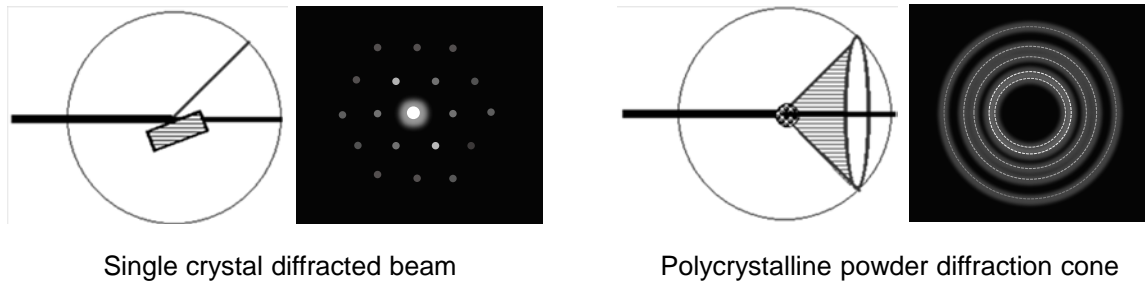
Figure 3.2. A single crystal diffracted beam with the relative discrete spots as diffraction pattern on the left side. On the right side the diffraction cone of a polycrystalline sample and the relative Debye rings. The diffraction patterns reported are schematic representations.

The XRD patterns reported in the following of the dissertation were recorded in a Philips PW 1820 diffractometer. This device (Figure 3.3) presents as X-ray source a copper tube with monochromatic K_α radiation (λ_{k_α} = 1.5418 Å). The diffractometer is operated in reflection mode with a Bragg–Brentano geometry: the X-ray source and the detector lie on a circle (i.e., goniometer) centered on the sample holder, that is rotated at one half the angular velocity of the detector. At this speed, the detector is always at 2θ and the sample at θ to the incident X-ray beam. Slits collimate the incident X rays. After passing through receiving slits, the diffracted X rays are monochromated and detected. The detector moves long the circle in steps ($\Delta\theta$), and measures the intensity for a certain time per step.
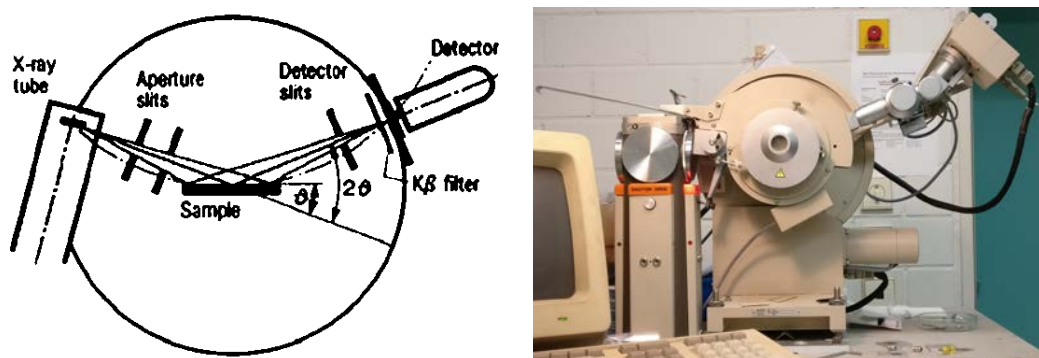

Figure 3.3. Bragg–Brentano geometry (left) and Philips PW18200 diffractometer (right).

The samples characterized in the thesis were all polycrystalline powders. They were carefully ground before the XRD to avoid the isoorientation of the crystallites and to have a statistical number of crystallites for each direction.

3. Characterization Methods

X-ray diffraction is a non-destructive method and it can provide many information:

- The *phase composition of the sample*: the diffraction pattern for each phase is unique as a fingerprint, the International Center for Diffraction Data (ICDD) manages and provides a data bank (Powder Diffraction File, PDF) containing hundreds of thousands catalogued structures, to allow the comparison of the experimental diffractograms with the reference patterns. A quantitative phase analysis for multiphase materials can be performed.

- *Crystallinity evaluation*: crystalline materials present only sharp and defined peaks in their diffractogram, instead semicrystalline materials (e.g., polymers) have broad signals, but a ratio crystalline/amorphous part can be calculated from the integrated intensities.

- *Unit cell parameters*: the peak positions are determined only by the size and the shape of the unit cell and each reflection is defined by the Miller indices of that lattice. Doping, temperature and pressure (e.g., phase transitions) can change the lattice parameters and can be monitored by the shift of the signal positions.

- *Crystal structure refinement and determination*: Rietveld refinement,[89] taking in account a crystal structure, instrumental and microstructural information, generate a theoretical diffraction pattern that can fit the experimental one, using the least square procedure to minimize the difference between the two. The fitting provides valuable information about the crystal lattice.

- *Crystallite size determination*: the dimension of coherent scattering domains is calculated from the peak widths, even if instrumental factors, defects in the lattice, strain (i.e., object deformation compared to its ideal dimension) influence them as well. The instrumental broadening can be determined measuring a reference crystalline sample (e.g., NIST LaB_6).

3.1.3 Crystallite Size Determination

In the previous section, the crystallite size determination was cited among the outcomes of an X-ray diffraction experiment. However, as already pointed out, the reflections widths are influenced not only by the crystallite size but also by instrumental factors and by the lattice strain. After subtracting or neglecting these factors, the size of the coherently scattering domains can be calculated with the Scherrer formula:[90]

$$L = \frac{K\lambda}{\beta \cos\theta} \tag{3.3}$$

where K is a constant commonly assumed as 0.94, λ is the radiation wavelength, θ is the diffraction angle of the reflection selected (usually the most intense of the diffractogram) and β the full width at the half maximum (FWHM) of the reflection in the scale of 2θ in radians. Equation (3.3) was developed by Scherrer in 1918 for cubic systems, assuming the sample monodisperse, the crystallite spherical and approximating the diffraction peak as a Gaussian: none of these conditions are usually respected, this is the reason why this method can be used only for comparison among a group of samples or for a rough idea about the size distribution, not for providing quantitative data.[88, 91]

3.2 Electron Microscopy

Electron microscopies are a kind of microscopy that uses accelerated electrons as source to create an image of a specimen. A microscope to be useful should resolve distances smaller than 0.1 mm (i.e., the minimum for a human eye). The resolving power of an optimal optical microscope cannot be higher than 200–100 nm. Therefore, to overcome this limit a source with smaller wavelength, such as an electron beam, is needed and the resolution can be in the order of the ångström. A general electron microscope is composed by an electron gun, the accelerated electron source, electromagnetic lenses, to direct and focus the beam, and a detector.

Electron microscopy can be classified in scanning electron microscopy (SEM) and transmission electron microscopy (TEM).

3.2.1 Scanning Electron Microscopy (SEM)

Scanning electron microscopy (SEM)[92] produces images of the sample surface by scanning it with a high-energy beam of electrons (typically 20–30 keV) in a raster scan pattern. As the beam interacts with the sample it creates various signals (secondary electrons, back-scattered electrons, characteristic X-rays, transmitted electrons), which are highly localized to the area directly under the beam and contain information about the sample surface topography, composition and other properties, such as electrical conductivity.

Both secondary and back-scattered electrons are revealed by a detector and the electric current associated to them is measured. The grey-scale surface image is formed using these

signals: the white areas correspond to high current (presence of material) and black spots to low current (less or no material). The obtained image is highly magnified (from about 10× to 1,000,000× for the best instruments) and it usually looks like a traditional microscopic image but with a much greater depth of field. The microscope spatial resolution depends on the size of the electron spot, which in turn depends on both the wavelength of the electrons and the electron-optical system which produces the scanning beam. The resolution is also limited by the size of the interaction volume, the extent to which the material interacts with the electron beam. Thus, the SEM resolution is not high enough to image individual atoms, while it is possible in the shorter wavelength with TEM.

On the other hand, the SEM has compensating advantages, such as the ability to image a comparatively large area of the specimen, the ease of sample preparation (which can be more complex in the case of TEM) and the availability of many analytical ways for measuring the composition and properties of the specimen (e.g., energy-dispersive X-ray spectroscopy, EDX).

Samples must be vacuum compatible (the analysis is realized in vacuum to avoid any interference with the electron beam), electrically conductive, at least at the surface, and electrically grounded to prevent the accumulation of electrostatic charge. Non-conductive specimens tend to charge when scanned by the electron beam and this causes scanning faults and other image artefacts.

For the projects described in the following, an ethanol or cyclohexane suspension of the samples was drop casted on silicon wafer to avoid conduction problems. The metal oxides presented in the thesis were electrical conductors, thus, in few cases, the SEM samples were prepared just sticking the powders on carbon tape instead of drop casting their suspensions on the wafers.

3.2.2 Transmission Electron Microscopy (TEM)

Transmission electron microscopy (TEM)[93] differs from SEM because the electronic beam arrives parallel to the sample and goes through it. The detector is placed under the sample and receives the transmitted electrons.

Three different acquisition modes are possible:

- *Bright field*: only the electrons that crossed the sample are detected; therefore, thicker sample regions or areas where are concentrated elements with high atomic number appear darker due to a higher absorption of electrons and parts with no sample will be brighter.

- *Dark field*: the direct beam is blocked and only diffracted rays are detected, therefore, the diffraction pattern will be the image (e.g., Figure 3.2). TEM in dark field mode can be compared to the XRD but with electrons instead of X-rays as source and can provide information about the crystal lattice, the spacing between the crystal planes and indexing of the reflections.

- *High resolution TEM* (HR-TEM): both the direct and the diffracted beams are detected and the resolution high enough to observe the reticular planes and atomic structures.

For the projects the acquisition mode bright field and high resolution TEM were employed.

3.3 Gas Chromatography

The gas chromatography (GC) is a chromatographic technique in which the mobile phase is an inert gas (in the present case helium flow) and the analytes are vaporized and solubilized in this mobile phase. The stationary phase could be a liquid or a solid present on the surface of the columns.

The molecules are eluted by the column at different times depending on their affinity with the stationary phase and they arrive to the mass spectrometer separately. The mass spectrometer is the GC detector: it breaks the molecules eluted in ionized fragment and classifies them in base of their mass–charge ratio. A typical mass spectrum is a plot of the intensity versus the mass–charge ratio of the chemical species.

At the end of the analysis, when all the chemical species are eluted and analyzed, a chromatogram (intensity vs. retention time) is given: the peaks correspond to the separate species present in the sample, selecting each of them in the GC–MS post run software is possible to see the corresponding mass spectrum. A comparison of that peak mass spectrum with the reference spectra reported in the data bank identifies the molecule relative to that chromatographic signal.

3.4 Physisorption of Nitrogen at Cryogenic Temperature: Specific Surface Area and Porosity Evaluation

IUPAC defines the adsorption as "the enrichment of molecules, atoms or ions in the vicinity of an interface. In the case of gas/solid systems, adsorption takes place in the vicinity of the solid surface".[94] Physisorption is a phenomenon that occurs when an adsorbable gas is brought in contact with the surface of a solid, only physical interactions (e.g., attractive and repulsive forces, Van der Waals, polarization, field dipole) are present and no chemical bonds are formed.[94]

A gas (usually nitrogen, but also argon and krypton can be adopted) is used at cryogenic temperature (i.e., 77 K for N_2) because low temperatures enhance the localization and the adsorption, and, furthermore, the weak interactions involved are more evident at low temperature. The physisorption of gas at cryogenic temperature is a non-destructive technique and usually it is reported as an isotherm plot, with the amount of gas adsorbed (usually a specific volume in $cm^3 g^{-1}$) against the relative pressure P/P_0 (where P_0 is the saturation pressure).

The specific surface area is one of the principal outputs of this characterization and it is determined with the Brunauer–Emmett–Teller method, known as BET method.[95] The specific surface area is calculated from the volume of gas needed to cover the surface of the material with a monolayer and the area occupied by an adsorbed molecule.[94] This value is crucial especially for heterogenous catalyst and it has been assessed for the ferrites and ammonium phosphomolybdate particles, as described in the following of the dissertation.

If the material analyzed is porous the extension of the surface area is higher increases because also the inner area of the pores is considered. The pores are usually classified according to their size.[96] Macropores, with size exceeding 50 nm, mesopores, with widths between 2 and 50 nm, and micropores, with size below 2 nm.

Information about the porosity are provided by the adsorption–desorption isotherms and, especially, by the hysteresis between the two curves. The IUPAC classifies the hysteresis loops in six categories (Figure 3.4).[94] H1 loop for uniform mesopores in narrow range; H2 type is typical of ink-bottle pores, the very steep desorption branch of H2(a) can be attributed to pore blocking, instead the H2(b) is associated to pore blocking but with much larger pore necks; H3 loop are typical of non-rigid aggregates of plate-like particles

or for a network of macropores not completely filled at the condensation; H4 hysteresis is typical of slit-shaped pores; H5 type is unusual and it is typical of structures containing both open and partially blocked mesopores. In the dissertation, the pore size distribution and the total pore volume were determined for the ferrites and the ammonium phosphomolybdate since those are fundamental features for catalysts and can point out differences between the synthetic routes adopted (e.g., bulk or miniemulsion routes).
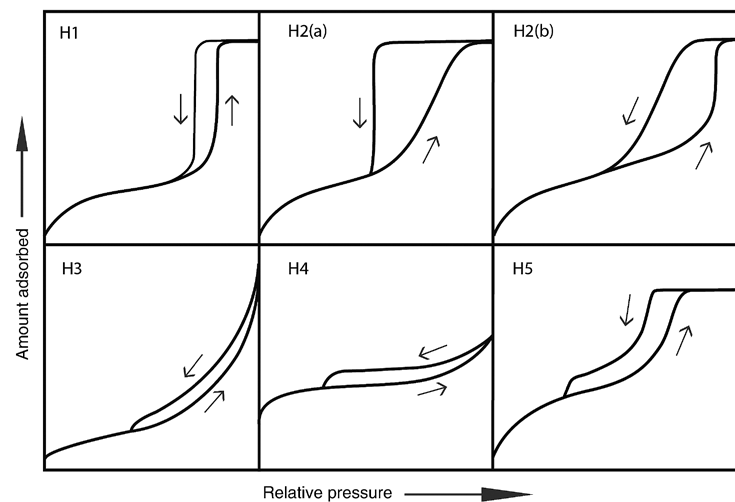

Figure 3.4. Classification of the hysteresis loops. Figure reproduced from Thommes, M.; Kaneko, K.; Neimark Alexander, V.; Olivier James, P.; Rodriguez-Reinoso, F.; Rouquerol, J.; Sing Kenneth, S. W., Physisorption of gases, with special reference to the evaluation of surface area and pore size distribution (IUPAC © Technical Report). In Pure and Applied Chemistry, ed. De Gruyter, 2015; Vol. 87, p. 1051.

3.5 Inductive Coupled Plasma–Mass Spectrometry (ICP-MS)

Inductively coupled plasma–mass spectrometry (ICP–MS) is an analytic technique for the detection of elements, especially metals, at very low concentration (i.e., order of the ppt).

The plasma is usually argon gas at very high temperature (i.e., 10,000 K) in an electromagnetic torch: the sample, usually liquid, is nebulized in the plasma and immediately ionized. The solid samples are generally either solubilized in an appropriate solvent or digested in strong acids (e.g., aqua regia).

The ions produced in the torch go to the mass spectrometer to be detected. The analyses can be quantitative and the concentrations determined through calibration with certified standards.

3.6 Interfacial Tension Measurements

The importance of the interfacial tension and of the resultant Laplace pressure for the inorganic crystallization in the confined space of the miniemulsion droplets has been already described in Sections 2.2.3.2 and 2.2.5.

The interfacial tension between the continuous and the disperse phase of inverse miniemulsions has been measured with two methods, pendant drop and spinning drop, at different temperatures.

In the case of the ferrites, the interfacial tension was determined at room temperature using the pendant drop method with an optical goniometer. The technique consists in suspending a drop from a needle in another bulk liquid, capturing a picture of that while is hanging and analyzing the drop shape with a software. In our case, the liquid with lower density (cyclohexane–PGPR 0.77 g cm^{-2}) was deposited in a polystyrene cuvette. A drop of the higher density liquid (water–salts 1.15 g cm^{-2}) was immersed in the cuvette, evaluating the interfacial tension through a drop shape analysis software. Averaged values from the data were recorded.

The interfacial tension value, in the case of the ferrites, was also cross checked with the spinning drop tensiometer. The principle is almost the same: a horizontal arranged capillary is filled with a bulk phase liquid (for our inverse miniemulsion system, the solutions of inorganic salts) and a drop of lower density liquid (the cyclohexane with PGPR) is placed inside. The capillary rotates and the drop is elongated by the centrifugal force. Knowing the rotation speed and the density of the two phases and measuring the droplet radius, the interfacial tension can be calculated.

The spinning drop can be employed to measure the interfacial tension also at high temperature, heating the capillary chamber with a thermostatic bath, as performed for the ammonium phosphomolybdate systems. The density of the solutions involved should be measured at the chosen temperature and with the same concentrations used for the analyses, because the density is a crucial value to obtain reliable calculations of the interfacial tension of the systems. In the case of the ammonium phosphomolybdates the interfacial tension was determined at the reaction temperature (i.e., 80 °C).

3.7 Magnetization Measurements

3.7.1 Theoretical Background

The magnetic moment is the elementary quantity of magnetism and at atomic level is associated to the spin of each electron. The magnetization M of a material is dependent on the alignment of the magnetic moments.[97] The magnetic flux density (also called overall magnetic field) B is related to the magnetic field intensity (also named magnetic field strength) H in the vacuum by the magnetic constant μ_0:

$$B = \mu_0 H \tag{3.4}$$

and in a medium they are related by the eq. (3.5):

$$B = \mu_0(H + M) \tag{3.5}$$

Sources of magnetic fields are electric currents and magnetized materials.

All the materials present in nature can be classified based on their magnetic behavior. In Figure 3.5 a schematic representation of the arrangement of the magnetic moments is reported for **diamagnetic** materials. Diamagnetic materials have all the electrons paired, therefore no magnetic behavior is present. Applying an external magnetic field H, a very weak magnetism is induced and all the magnetic moments orient opposite to H. Generally, this diamagnetic field is so weak that cannot be observed macroscopically. When the external field is removed, all the electrons pair again.
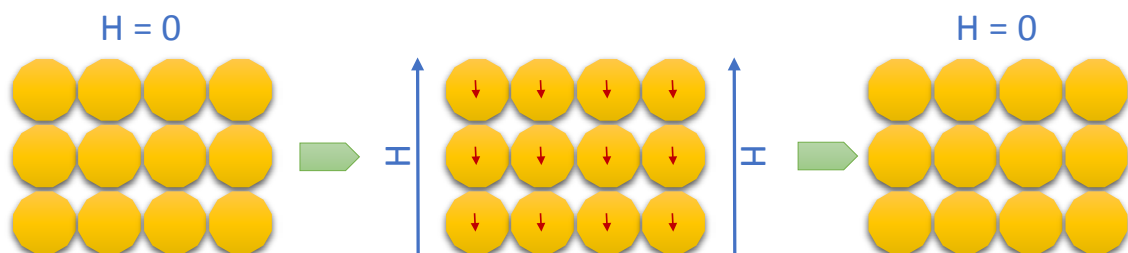
Figure 3.5. Arrangement of the magnetic moments in a diamagnetic material: when an external magnetic field H is applied, the spins are oppositely aligned to it.

A **paramagnetic** material is schematically represented in Figure 3.6. Differently from diamagnetic materials, unpaired electrons are present but, in absence of magnetic field, they are not aligned in the same direction due to entropy and thermal motion. As soon as

an external magnetic field is applied, the spins of the unpaired electrons align in the same direction of H, resulting in a net magnetization. When the external magnetic field is removed, the spins return to be randomly oriented.
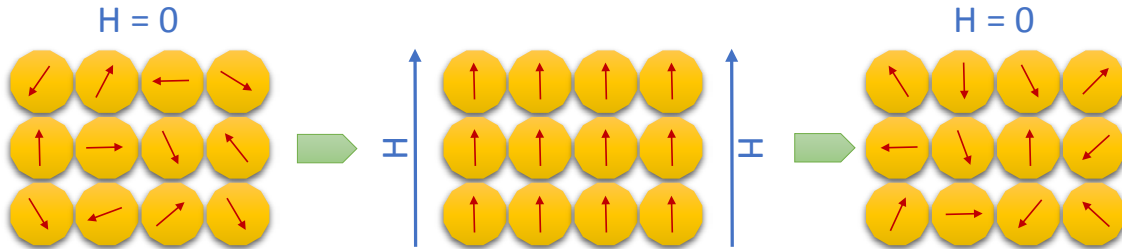

Figure 3.6. Arrangement of the magnetic moments in a paramagnetic material: when an external magnetic field *H* is applied, the spins are aligned to its directions.

The magnetization of paramagnetic materials is, indeed, inversely proportional to the temperature as reported in eq. (3.6):

$$M = \frac{C}{T} H \tag{3.6}$$

Where *C* is the Curie constant, specific for each material. Decreasing the temperature, the thermal motion is decreasing as well and the spins align more easily in the same direction.

The most evident manifestation of magnetism in solids is the spontaneous magnetization of **ferromagnetic** materials (Figure 3.7). The starting point is the same of a paramagnetic material, the unpaired electrons are randomly oriented and, as soon as an external magnetic field is applied, they align in the same direction of it. After the removal of the magnetic field, however, the spins retain their alignment and the solid remains magnetized.
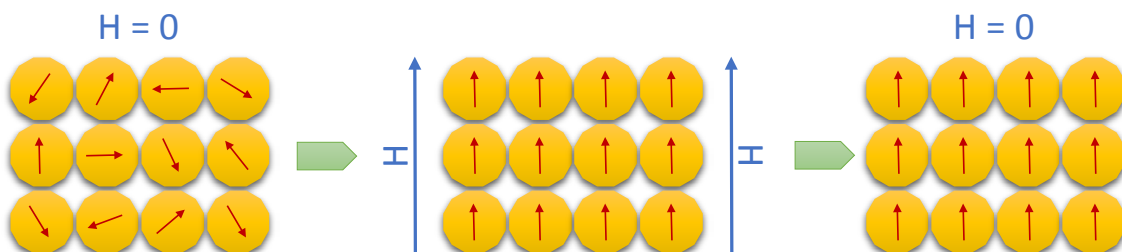
Figure 3.7. Arrangement of the magnetic moments in a ferromagnetic material: when an external magnetic field *H* is applied, the spins are aligned to its directions. The alignment is retained even after the removal of the external magnetic field.

Bulk ferromagnetic solids are divided in microscopic regions called *magnetic domains* (or Weiss domains) where all the spins are aligned in the same direction but, when the material is unmagnetized and $H = 0$, each domain has a different orientation and their overall magnetic field is little or null. When an external magnetic field is applied, all the domains align in the same direction of it and they will remain align in that way also when H will be removed, because, changing their orientation, the domains remain trapped in some crystal defects and they cannot return to their original direction. Iron, nickel and cobalt are ferromagnetic.

The magnetic domains are responsible of further kinds of magnetism, as shown in Figure 3.8.
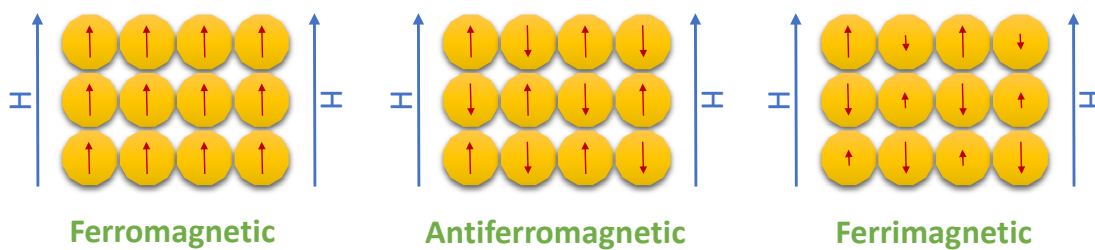
Figure 3.8. Classification of the different kind of ordered magnetism.

In the case of **antiferromagnetism**, after the application of an external magnetic field, each domain is regularly oriented in opposite directions to the neighbors, therefore, the overall magnetization is almost zero.

Ferrimagnetic solids are usually composed of two populations of atoms with unequal and antiparallel magnetic moments. The spinel ferrites (see Section 4.1) are a typical example of ferrimagnetic solids. Taking for instance the magnetite (spinel ferrite Fe_3O_4), eight Fe^{3+} ions occupy the tetrahedral sites and other eight Fe^{3+} the tetrahedral sites, but they have antiparallel spins, therefore, they cancel each other. The observed magnetization comes only from the Fe^{2+} ions in the octahedral sites.[2]

As showed in the eq. (3.6), the magnetization is inversely proportional to the temperature and when the temperature is higher than the Curie temperature (T_c, i.e., the temperature at which a material loses its permanent magnetic properties) the materials become paramagnetic and the spins are randomly distributed in absence of magnetic field.

3. Characterization Methods

Nanoparticles of ferro or ferrimagnetic materials are **superparamagnetic** if they have the same size of a magnetic domain (single-domain particle). When $H = 0$ the nanoparticles change direction very fast for the Brownian motion and thermal energy, thus no net magnetic field results. Applying an external magnetic field, all the nanoparticles orient in its direction and a strong magnetization is produced. Removing the field, the nanoparticles return to be randomly oriented. The superparamagnetism reminds paramagnetism because of the absence of magnetization when the external magnetic field is removed and ferromagnetism for the high magnetization reached under the influence of a low magnetic field. Superparamagnetic nanoparticles have short relaxation time and they quickly orient to an alternating external magnetic field. The spinel ferrites nanoparticles described in the following of the dissertation (see Section 4.1.6) are superparamagnetic at room temperature, except for $CoFe_2O_4$, and the miniemulsions of the ferrites were **ferrofluidic** (i.e., colloidal liquids made of ferro or ferrimagnetic nanoparticles).

3.7.2 Instrumentation and Results

The room temperature magnetic behavior of the ferrite nanoparticles was characterized by measuring the magnetic hysteresis and the saturation magnetization in a superconductive quantum interference device (SQUID) magnetometer.

The SQUID is a very sensitive detector of magnetic flux and consists of tiny loops of superconductors employing Josephson junctions.[98] Josephson junctions are devices made of two superconductors coupled together by a link (e.g., an insulator or a non-super-conducting metal) in a way that a supercurrent is formed, a current that flows indefinitely long without any voltage applied. The SQUID responds to changes in the magnetic flux within the superconducting loop with a change in voltage, in the case of a direct current (dc) device, or with a change in the amplitude of the oscillating voltage, in the case of radio frequency (RF) device.

Gelatin capsules were filled with the weighed samples and mounted in a low magnetic moment sample holder of the SQUID. The diamagnetic contribution of the gelatin capsule was measured and subtracted.

The output of the SQUID is a magnetization curve, a plot of the magnetization (M) as function of the external magnetic field (H). The curves of ferrimagnetic ($CoFe_2O_4$

synthesized in miniemulsion) and superparamagnetic materials ($NiFe_2O_4$ synthesized in miniemulsion) are reported in Figure 3.9. Generally, the magnetization reaches a state where it cannot be further risen by an increase of H, this is the saturation magnetization M_s, and corresponds to the alignment of all the magnetic domains with H. The remanence M_r is the magnetization remaining at $H = 0$ and it is present only for ferro and ferrimagnetic materials, not for the superparamagnetic ones, since they quickly demagnetize when $H = 0$ (they don't present a hysteresis loop). The coercivity H_c is the magnetic field required to return to $M = 0$, therefore express how difficult is to demagnetize a material. Materials with high coercivity (large hysteresis) are *hard* magnetic materials and usually exploited for permanent magnets, instead materials with low coercivity (little hysteresis) are *soft* magnetic materials, easy to magnetize and demagnetize. The bulk ferrites are usually soft magnetic, except of the cobalt ferrite that is hard.
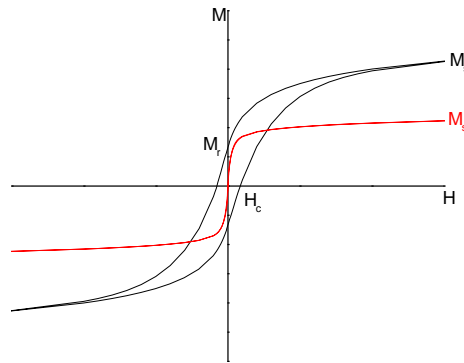
Figure 3.9. Magnetization curves of a ferromagnetic material ($CoFe_2O_4$, black curve) and of a paramagnetic material ($NiFe_2O_4$, red curve). The curves are the result of the experimental measurements on the ferrites synthesized in miniemulsion.

3.8 X-Ray Absorption Spectroscopy (XAS)

A monochromatic X-ray of energy E passes through a homogeneous sample and it is attenuated, analogously to the Lambert-Beer law[3]

$$I(E) = I_0(E)e^{-\mu(E)\cdot d} \tag{3.7}$$

where *I(E)* and *I$_0$(E)* are the incident and transmitted X-ray intensities, $\mu(E)$ is the linear absorption coefficient and d the thickness of the sample. The absorption coefficient decreases with increasing the energy of the incident beam till a threshold frequency is reached and the absorption coefficient dramatically rises. This steep increase of *μ(E)* is

called absorption edge and corresponds to the ejection of a core electron from an atom. The X-ray absorption spectroscopy (XAS) is the measurement of the absorption coefficient as function of the X-ray energy.[99] The absorption coefficient of an isolated atom rises only in correspondence of the absorption edges (corresponding to the shells from which the electrons are removed). In contrast, for atoms in molecules or in condensed phase the absorption coefficient above the absorption edge shows a fine structure, called EXAFS, extended X-ray absorption fine structure.[100] The XAS spectrum usually is divided in three regions (Figure 3.10).
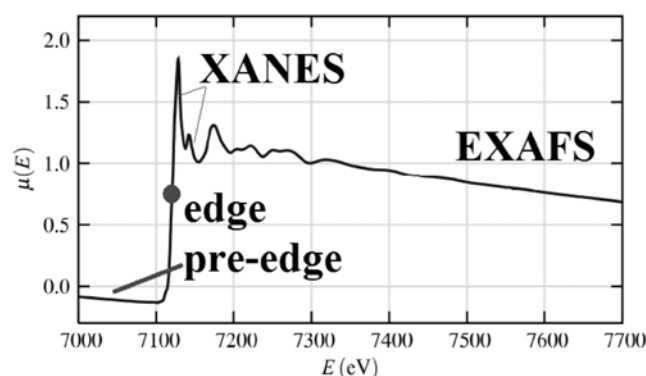
Figure 3.10. X-ray absorption spectrum composed of a pre-edge area, the X-ray absorption near edge structure (XANES) and the extended X-ray absorption fine structure (EXAFS).

The zone just before the absorption edge is the "pre-edge": sometimes in this region there are some peaks and in the best cases their interpretation can provide information about the symmetry and the electronic structure of the elements. The absorption edge is indicated in Figure 3.10 by the dot corresponding to the inflection point. The X-ray absorption near edge structure (XANES) gives information about the nature of the absorbent, its oxidation state, its coordination symmetry and its orbitals. The extended X-ray absorption fine structure (EXAFS) provides information about the coordination and the chemical surrounding of the absorbent atom and the interatomic distances. XAS is, indeed, powerful for very sensitive short-range structural and chemical investigations of the materials and it is specific for each element present, that can be analyzed independently.

The measurement needs a synchrotron radiation, source with high energy, brilliance and collimation, and the proper energy is selected with a crystal monochromator before hitting the sample. Two ionization chambers in front and behind the specimen measure the incident and the transmitted intensity (transmission mode). Additionally, the absorption

spectrum of a reference is measured to calibrate the energy scale and to monitor any irregularity.[99] Also a fluorescence mode is available where, instead of the transmitted intensity, the fluorescence, proportional to the absorption coefficient, is detected.

In the dissertation, the XAS has been carried out on the ferrite samples to investigate their cation distributions and, consequently, their inversion degree.

4. Results and Discussion

4.1 Synergy of Miniemulsion and Solvothermal Conditions for the Crystallization of Transition Metal Ferrites[2]

In this section, the preparation and the characterization of crystalline transition metal ferrites by a novel synergetic combination of miniemulsion synthesis and solvothermal route is presented. The simultaneous employment of the two routes combines unconventional conditions in terms of space confinement, temperature, and pressure. Six crystalline ferrites were achievable at much lower temperature (i.e., 80 °C) than usually required and without any post-synthesis thermal treatment. X-ray diffraction (XRD) revealed that analogous ferrites synthesized by miniemulsion at ambient pressure or in bulk, either at ambient pressure or under solvothermal conditions, were not comparatively highly crystalline products. The ferrites synthesized by the synergy displayed superparamagnetism and were active oxidation catalysts.

4.1.1 Introduction

Ferrites were selected as model material to study the effects of the synergy between miniemulsion synthesis and solvothermal conditions. They are ternary metal oxides recently encountering a great development and interest not only for their thermal, mechanical, and chemical stability,[101, 102] and for their magnetic properties,[97, 103, 104] but also for their outstanding electric and structural properties,[105] making them appealing for a wide array of applications. In particular, ferrites are being exploited for catalysis[106, 107] and photocatalysis[108] of several reactions, such as C–C and C–X coupling reactions,[106] alkylation reactions,[109] and oxidation reactions of alcohol to aldehydes,[110] of CO,[111] of styrene,[112, 113] and of toluene.[114, 115] The ferrite-catalyzed production of hydrogen through the photocatalytic water splitting is as well a promising application of these materials.[116, 117]

Furthermore, ferrites are magnetic materials, being hence easily recoverable from the reaction medium, which is important for achieving sustainable and green methodologies for chemical reactions.[118]

The principal routes for preparation of ferrites have been, up to now, solid-state synthesis and high temperature approaches,[82, 119-121] but more sustainable and low-temperature methods of synthesis are required.[60, 83] Generally, the multinary oxides obtained by wet-chemistry preparation are single-phase, more homogeneous, and characterized by smaller crystallites than those prepared by conventional solid-state reactions.[60] Among wet-chemistry routes,[60] the most commonly employed techniques for synthesis of ferrites are sol–gel,[122] non-aqueous sol–gel,[123-125] hydrothermal and solvothermal routes,[80, 126] coprecipitation,[27, 29] and microemulsion.[61, 127] Miniemulsion technique, as discussed in the Theoretical Background, is an innovative way to employ a wet-chemical strategy to achieve crystalline inorganic materials at low or even room temperature.

Non-classical crystallization pathways can be investigated with solvothermal conditions,[80, 128] already described in the Theoretical Background of this dissertation. At high pressure and temperature, relevant physical parameters of the solvent (ionic product, density, viscosity, dielectric constant) change; thus, the solubilization and the crystallization of compounds that normally would not occur, can be pursued.[60, 82]

In this section, our working hypothesis will be demonstrated: the synergy of the unconventional conditions provided by the simultaneous use of the miniemulsion and of the solvothermal route could lead to an improved crystallinity of the products when compared to materials prepared from conventional miniemulsions (i.e., at ambient pressure) or by simple solvothermal synthesis. Further investigations concerning the role of the synthetic approach and, in the case of the synergy, also of the reaction time, were carried out for zinc ferrite. Zinc ferrite was chosen as a model because, among the spinel ferrites discussed in this section, it is the only one displaying a complete direct structure in the bulk phase.

4.1.2 Synthetic Approaches for Transition Metal Ferrites

A generic spinel ferrite is typically prepared through the precipitation of the iron and the divalent metal hydroxides immediately after the addition of a NaOH solution to an aqueous solutions of salts, as reported in literature.[32] In such a case, the mixture of

hydroxides is heated at a certain temperature (e.g., 390 °C) to produce the ternary metal oxides. The combination of miniemulsion synthesis and subcritical solvothermal conditions allowed to synthesize crystalline spinels at much lower temperature (i.e., 80 °C) than generally reported in literature, exploiting the precipitation of the hydroxides in the confined space of the miniemulsion droplets under non-standard conditions.

Inverse miniemulsion was employed for our synthesis: this system was critically stabilized against coalescence by commercial polyglycerol polyricinoleate (PGPR), dispersed in the continuous phase (cyclohexane). This surfactant was selected because it is lipophilic with a low hydrophilic–lipophilic balance (HLB) (around 1.5).[129] On the other hand, the inorganic precursors were solubilized in the disperse phase (Milli-Q water). The miniemulsion was formed by high shear forces (ultrasounds) and the precipitation inside the water droplets started as soon as NaOH solution was added and ultrasound applied (Figure 4.1).

The adopted procedure is the result of a careful optimization: at the beginning of the project, different experiments were carried out by changing independently (i) concentration of precursors, (ii) precipitating agents, and (iii) ways of addition of the precipitating agent.

Firstly, the concentration (c) of the precursors was set at low values: iron chloride solution was 0.1 M and the other metal chloride solution was 0.05 M, taking as reference the concentrations usually reported in literature for the bulk solution synthesis of these materials.[30, 31] The syntheses performed with such concentrations were unsuccessful: the particles were not formed or their size was too small. In the miniemulsion, as already explained, the reactions occur inside the water droplets and the growth of the particles is controlled by the amount of precursor present inside in the confinement and if, as in this case, the overall concentrations of the reagents is extremely low, their quantity inside the droplets is almost negligible and the particles cannot growth properly. If a generic water droplet of an inverse miniemulsion is considered a sphere with a diameter of 100 nm, its volume (V) is $5 \cdot 10^{-19}$ dm^3 (eq. (4.1)), thus knowing the precursor concentrations is possible to calculate the average moles of each element and consequently of the ferrite, in each droplet (eq. (4.2)). Taking as a model the $CoFe_2O_4$ (MW=234.62 g mol^{-1}), the calculations are reported in the following.

$$V_{\text{droplet}} = \frac{4}{3}\pi r^3 = 5 \cdot 10^{-19}\text{dm}^3 \tag{4.1}$$

$$\text{mol}_{\text{Co}} = c_{\text{Co}} \times V_{\text{droplet}} = 3 \cdot 10^{-20}\text{mol} = \text{mol}_{\text{CoFe}_2\text{O}_4} \tag{4.2}$$

$$V_{\text{CoFe}_2\text{O}_4\text{particle}} = \frac{m_{\text{CoFe}_2\text{O}_4}}{\rho_{\text{CoFe}_2\text{O}_4}} = \frac{\text{mol}_{\text{CoFe}_2\text{O}_4} \times \text{MW}_{\text{CoFe}_2\text{O}_4}}{\rho_{\text{CoFe}_2\text{O}_4}} = 10^{-21}\text{dm}^3 \tag{4.3}$$

$$d_{\text{CoFe}_2\text{O}_4\text{particle}} = 7 \text{ nm} \tag{4.4}$$

From the ferrite moles per droplet and the ferrite density $(\rho_{\text{CoFe}_2\text{O}_4} = 5.3\,\text{g cm}^{-3})$ is possible to calculate the volume of an average particle (eq. (4.3)) and from that the diameter $(d_{\text{CoFe}_2\text{O}_4\text{particle}})$ of a generic ferrite particle grown in the droplet, around 7 nm (eq. (4.4)). The syntheses in confinement require higher concentrations to achieve particles: after these considerations, the concentration adopted for the precursors was increased ten times and the calculated particle diameter was about 14 nm.

Secondly, the precipitating agent, instead of being added directly as water solution, was provided through a second miniemulsion, prepared with cyclohexane–PGPR as continuous phase and sodium hydroxide water solution as disperse phase. The two resulting miniemulsions, the one containing the precursors and the other containing the precipitating agent, were mixed together. This strategy was abandoned, because the NaOH could not reach efficiently the precursors, hence the yield was low and, furthermore, the resulting final miniemulsion was not stable.

Finally, triethylamine was employed as precipitating agent, because this organic base is dispersible both in the organic and in the water phase and, in principle, should be more suitable for the biphasic miniemulsion. However, for the synthesis of ferrites the NaOH was more successful as precipitating agent, probably because the hydroxides ions are more readily available to react with the precursors.

After the addition of the precipitating agent and the second sonication step, the system was placed in a Teflon-lined autoclave reactor under subcritical solvothermal conditions, generated upon heating of the closed vessel (Figure 4.1). The autogenous pressure is $2 \cdot 10^5$ Pa, 2 bar, at 80 °C and $3 \cdot 10^5$ Pa, 3 bar, at 100 °C as calculated with Antoine's equation.[85]
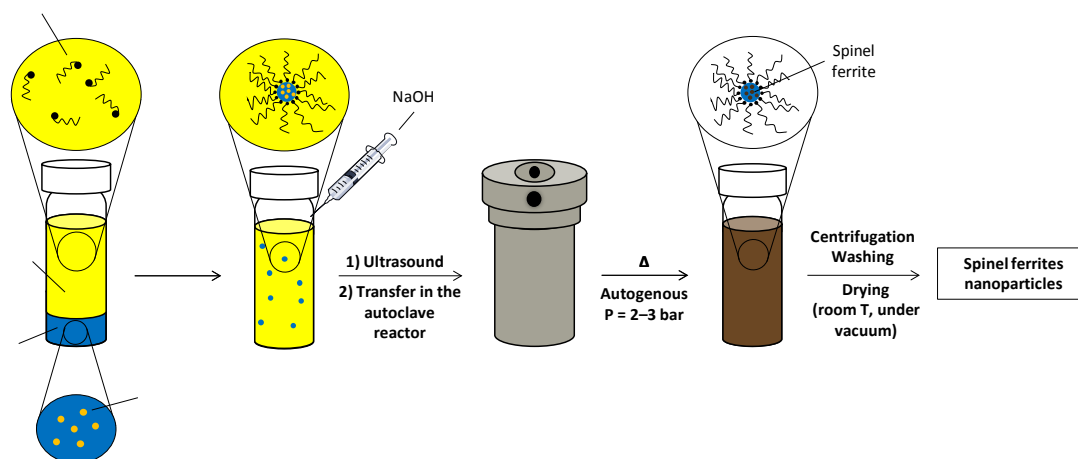
Figure 4.1. Combination of inverse miniemulsion process and solvothermal conditions for the synthesis of spinel ferrites.

In the case of zinc ferrite a comparison among different approaches was carried out (the labeling of the samples used in the following is indicated in brackets): (i) miniemulsion under solvothermal conditions (ME–HP), (ii) miniemulsion at ambient pressure (ME), and (iii) bulk procedure, which involves the mixing of the inorganic precursors and the precipitating agent and directly the precipitation of the products, either at ambient pressure (bulk) or combined with solvothermal conditions (bulk–HP).

Another suitable wet-chemistry route for the synthesis of ferrites, alternative to the coprecipitation of the hydroxides, is the coprecipitation of oxalates: the metal precursors, in the presence of oxalic acid, form the oxalates after the addition of the precipitating agent (generally a concentrated base). This synthesis can be followed by either thermal treatment at high temperature or by low-temperature subcritical hydrothermal processing to afford the final crystalline oxides. [30, 31] In an initial stage of the work, pursuing the optimization of the reaction, the combination of the coprecipitation of the oxalates with the miniemulsion technique was employed to achieve the formation of spinel ferrites. The inorganic precursors and the oxalic acid were dissolved in the aqueous disperse phase and the precipitating agent (NaOH) was added to the miniemulsion. However, this procedure did not lead to single-phase crystalline materials and, despite several washings of the products, the oxalic acid was still present. This finding can be traced back to the environment of the confined space of a miniemulsion droplet, which is completely different from the environment of a standard bulk synthesis.[75] The precipitation of the hydroxides was found to be a more successful and reliable route.

4.1.3 Structural Characterization of Transition Metal Ferrites Obtained by the Combination of Miniemulsion and Solvothermal Conditions

X-ray diffraction (XRD) provides information not only about phase purity and crystallite size of the crystalline materials but, more importantly, also about their structural evolution towards the crystalline phase as a function of sample composition, pressure, reaction time, and temperature. To explore the effects of those parameters, the crystallization of the zinc ferrite was therefore followed by analyzing ex-situ samples after different reaction times (Table 4.6). Information on the structural evolution in the long range was integrated and complemented by the one on the local range delivered by XAS measurements (see below).

The diffractograms of all ferrites produced from miniemulsion under solvothermal conditions are reported in Figure 4.5. The diffractograms of iron, cobalt, and copper ferrites match with the reference patterns of the corresponding MFe_2O_4 present in the ICDD PDF-2 database. Although the diffractograms of manganese, nickel, and zinc ferrites are matching with the corresponding references patterns of $MnFe_2O_4$ (ICDD card no. 01-074-2403, Figure 4.2), $NiFe_2O_4$ (ICDD card no. 00-054-0964, Figure 4.3) and $ZnFe_2O_4$ (ICDD card no. 00-022-1012, Figure 4.4) the stoichiometry obtained from inductively coupled plasma mass spectrometry (ICP–MS) is not compatible with the expected atomic ratio M:Fe=1:2 (Table 4.1).

Table 4.1. Results of the ICP–MS analysis performed on ferrites synthesized under miniemulsion–solvothermal conditions. The autogenous pressure present in the autoclavable vessel (i.e., solvothermal bomb) during the experiments was 200 kPa for the reactions at 80 °C and 300 kPa for the reaction at 100 °C.

Metal (M) present in the ferrite	Reaction temperature / °C	[M] / [Fe] Molar
Mn	80	0.99 ± 0.03
Co	80	0.510 ± 0.005
Ni	100	1.00 ± 0.03
Cu	80	0.50 ± 0.01
Zn	80	0.305 ± 0.003
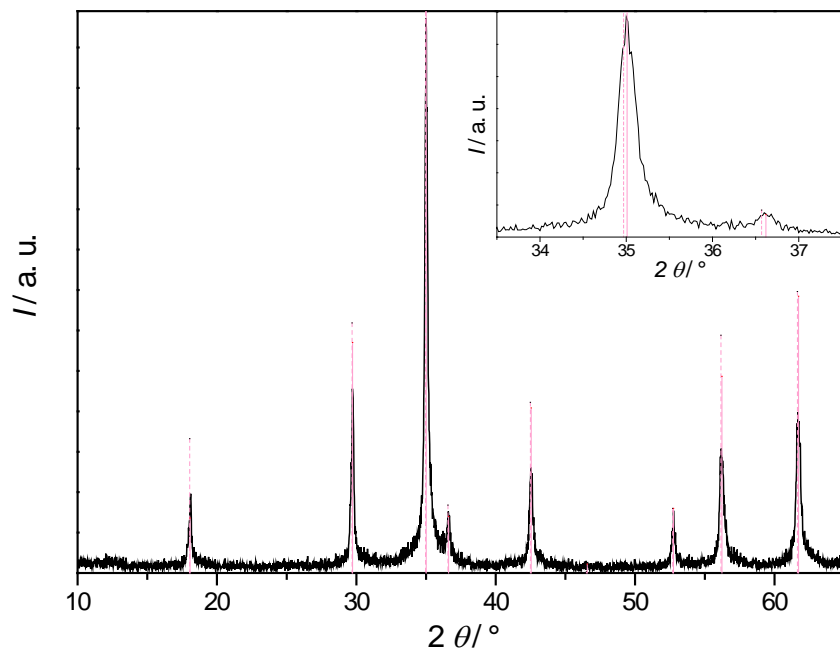
Figure 4.2. X-ray diffractogram of $Fe_3Mn_3O_8$ synthesized in miniemulsion–solvothermal conditions. The reference patterns are reported as vertical lines: $Fe_3Mn_3O_8$ (ICDD card no. 01-075-0034, continuous line) and $MnFe_2O_4$ (ICDD card no. 01-074-2403, dashed line). In the inset plot, a magnification of the diffractogram between 33.5° and 37.5° is reported: the reference patterns of the two crystalline structures are almost overlapping.
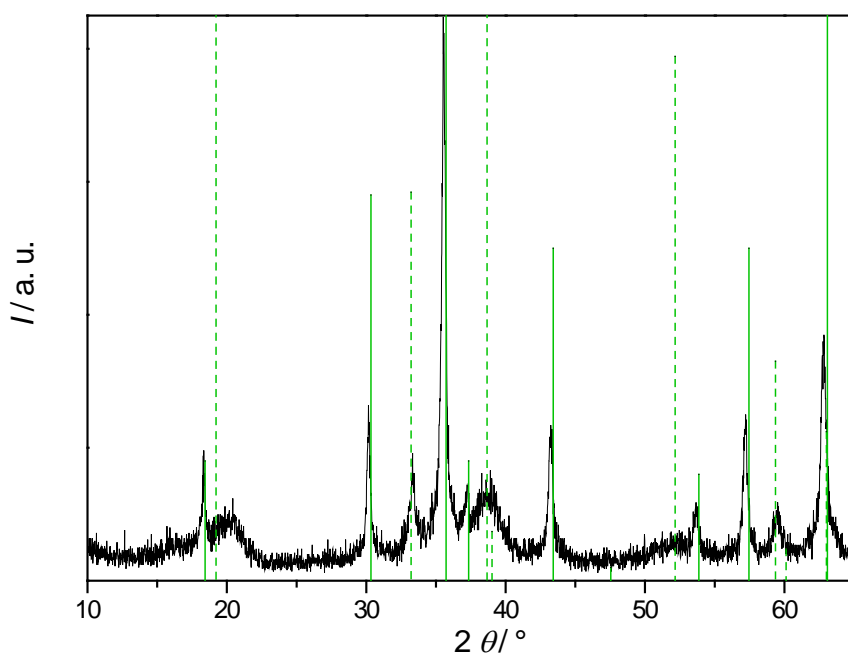
Figure 4.3. X-ray diffractogram of $NiFe_2O_4$ synthesized in miniemulsion–solvothermal conditions. The reference patterns are reported as vertical lines: $NiFe_2O_4$ trevorite syn (ICDD card no. 00-054-0964, continuous line) and $Ni(OH)_2$ (ICDD card no. 01-073-1520, dashed line). The diffractogram presents reflections typical of both phases, therefore the sample produced is a mixture of both materials.
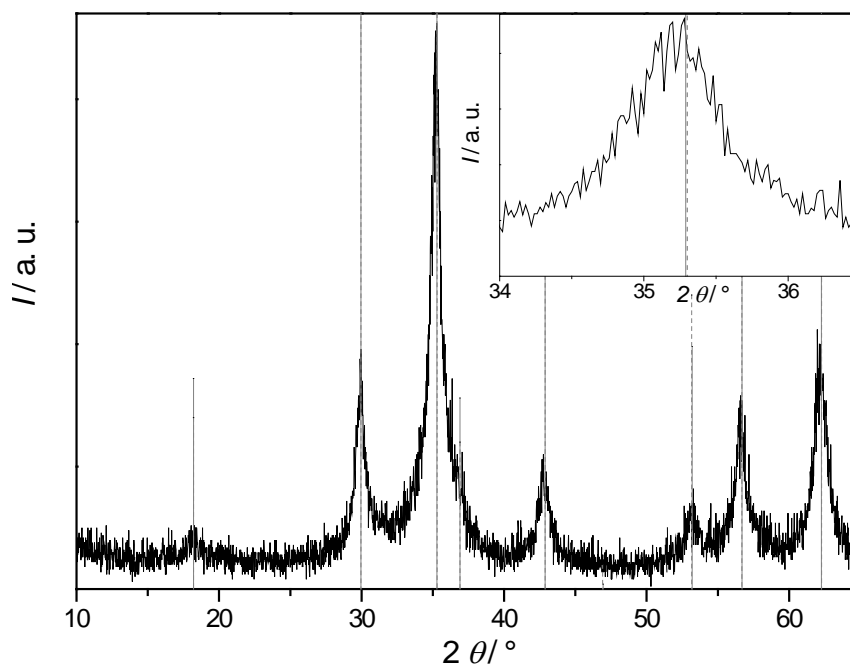
Figure 4.4. X-ray diffractogram of iron-rich zinc ferrite synthesized in miniemulsion–solvothermal conditions. The reference patterns are reported as vertical lines: $(Zn_{0.664}Fe_{0.336})(Fe_{1.934}Zn_{0.066})O_4$ (ICDD card no. 01-086-0508, continuous line) and $ZnFe_2O_4$ (ICDD card no. 00-022-1012, dashed line). In the inset plot a magnification of the diffractogram between 34° and 36.5° is shown: the reference patterns of the two crystalline structures are overlapping.

The synthesis of manganese and nickel ferrites required, to obtain a crystalline material, a molar ratio between the precursors of metal:Fe 1:1, differently from the other ferrites synthesized with a metal:Fe molar ratio of 1:2; therefore, the molar ratio 1:1 adopted for the synthesis is probably the reason of the values measured by the ICP–MS. In addition to the pattern of $MnFe_2O_4$, the diffraction pattern of the manganese compound is matching as well with the reference pattern of $Fe_3Mn_3O_8$ (ICDD card no. 01-075-0034), as reported in Figure 4.2. $Fe_3Mn_3O_8$ is another kind of spinel ferrite, less common, faced-centered cubic and with the same point group ($Fd\bar{3}m$) as the jacobsite $MnFe_2O_4$, but with a slightly contracted lattice. The explanation of the molar ratio Zn/Fe 0.3 obtained by ICP–MS cannot be ascribed to the adopted different atomic ratio between the precursors, since the amounts of zinc and iron chlorides used were in the common atomic ratio 1:2, but probably to the formation of a more favored crystalline phase, similar to the iron-rich ferrite $(Zn_{0.664}Fe_{0.336})(Fe_{1.934}Zn_{0.066})O_4$ corresponding to the ICDD card no. 01-086-0508 (franklinite ferroan, see Figure 4.4). The crystal structure of this phase is also in this case spinel and face-centered cubic (space group $Fd\bar{3}m$) like the franklinite $ZnFe_2O_4$. In the case of the nickel ferrite, the molar ratio Ni:Fe 1:1 corresponds actually to the molar ratio adopted for the synthesis between $FeCl_3 \cdot 6H_2O$ and $NiCl_2 \cdot 6H_2O$, as aforementioned. However, the diffractogram of this sample presents the typical reflections of $NiFe_2O_4$, but

also reflections ascribed to $Ni(OH)_2$, as reported in Figure 4.3. The syntheses were performed in an alkaline aqueous solution of the metal salts at a measured value of pH of 13.8. According to the pH–concentrations diagram of aqueous solution of nickel ions, a description of the behavior (i.e., concentrations and chemical species) of the ions as a function of the pH, nickel hydroxide, and further oxo-hydroxo species, characterized by very low K_{sp}, already precipitate at pH 7. In our reaction conditions at pH 13.8, Ni should be present as insoluble hydroxide. Since the formation of the ferrites, under the chosen experimental conditions, occurs upon coprecipitation and dehydration of the corresponding hydroxides, it can be inferred that part of the hydroxide has not been decomposed to give the targeted material.
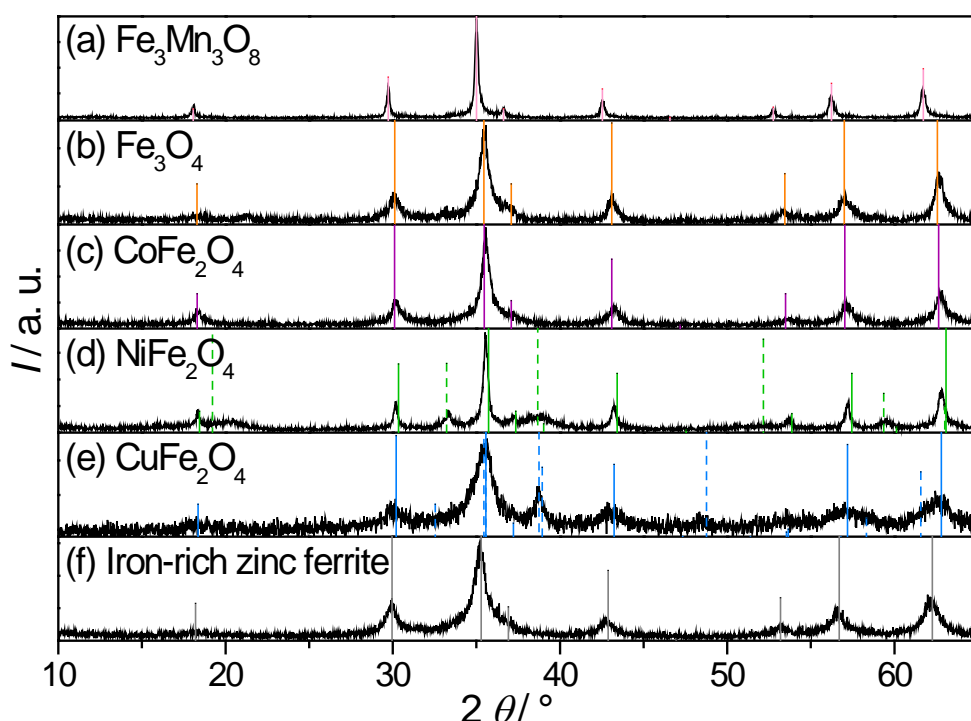
Figure 4.5. X-ray diffractograms of the ferrites produced using the solvothermal–miniemulsion route at 80-100 °C: (a) $Fe_3Mn_3O_8$ with its reference pattern ICDD card no. 01-075-0034 reported as vertical lines (b) Fe_3O_4 with ICDD card no. 00-019-0629 (c) $CoFe_2O_4$ with ICDD card no. 00-022-1086 (d) $NiFe_2O_4$ with its reference pattern (continuous line) ICDD card no. 00-054-0964 and the reference pattern of $Ni(OH)_2$ (dashed line) ICDD card no. 01-073-1520 (e) $CuFe_2O_4$ with its reference pattern (continuous line) ICDD card no. 01-077-0010 and the reference pattern of CuO (dashed line) ICDD card no. 00-048-1548 (f) iron-rich zinc ferrite with ICDD card no. 01-086-0508, related to $(Zn_{0.664}Fe_{0.336})(Fe_{1.934}Zn_{0.066})O_4$.

The diffractogram of $CuFe_2O_4$ displays, as well, the presence of the reflections ascribable to CuO, but the stoichiometry assessed by ICP–MS is as expected 1:2, consistent with nominal molar ratio between copper and iron chlorides of 1:2 used in the synthesis.

To better define the structure of the six ferrites produced in miniemulsion–solvothermal conditions in terms of sites occupation and quantify the relative amount of the crystalline phases, Rietveld refinement was performed on the collected diffractograms. These procedures evidenced, for most ferrites, the presence of two different populations with different sizes. The crystallite sizes and relative weights are reported in Table 4.2.

Table 4.2. Phase composition with relative weight and crystallite size (L) for the all the six ferrites produced in miniemulsion–solvothermal conditions, calculated by Rietveld refinement.

Sample	Phase(s)	L / nm	Weight %
$MnFe_2O_4$	$MnFe_2O_4$	5	40
		46	60
Fe_3O_4	Fe_3O_4	5	45
		16	55
$CoFe_2O_4$	$CoFe_2O_4$	5	55
$NiFe_2O_4$	$Ni_1Fe_2O_4$	27	59
	$Ni(OH)_2$	-	41
$CuFe_2O_4$	$CuFe_2O_4$	5	81
	CuO	16	19
$ZnFe_2O_4$	Iron-rich $ZnFe_2O_4$	4	57
		13	43

In conclusion, although with slight variations in the metal/Fe ratios, all obtained ferrites are classified as spinels, with a face-centered cubic crystal system and $Fd\overline{3}m$ space group: the achievement of such crystalline spinel ternary oxides from the combination of miniemulsion and solvothermal conditions is, to the best of our knowledge, an unprecedented result. The synergetic route allowed to obtain (except in the case of Ni and Cu, where, though much less intense reflections ascribed to $Ni(OH)_2$, and CuO, respectively, were also detected) phase pure crystalline materials and at lower temperature, 80 °C with respect to temperatures above 150 °C employed in other routes.[130] The low temperature synthesis and the absence of post-synthesis thermal treatment are appealing from the perspective of sustainability and to avoid coalescence and coarsening of the nanoparticles, resulting in uncontrolled growth. As described above the formation of crystalline spinels for all samples is the result of a long process of optimization, which involved an accurate selection of the synthetic procedure, reagent molar ratios, and

reaction temperature: Mn and Ni ferrites were not obtained as expected from the molar ratio M:Fe 1:2, but rather with a 1:1 M:Fe molar ratio. Furthermore, a clearly crystalline $NiFe_2O_4$ was obtained only working at 100 °C (at 80 °C the product was not crystalline). Interestingly, as visually assessed, the miniemulsions were stable for few hours and no phase separation occurred. Despite of the boiling point of the cyclohexane (80.75 °C), they remained stable even after heating at 80–100 °C for 24 h.

4.1.4 Comparison among the Different Synthetic Routes: Effects on the Crystallinity

To investigate the effect of the different routes (miniemulsion and bulk, either at ambient pressure or under solvothermal conditions) on the crystallinity of the samples, a comparison of the XRD patterns of the iron-rich zinc ferrites is reported in Figure 4.6. Only the sample prepared by the synergetic approach (miniemulsion under solvothermal conditions) is highly crystalline, whereas the application of miniemulsion at ambient pressure and bulk procedure in both conditions yield a poorly crystalline material.
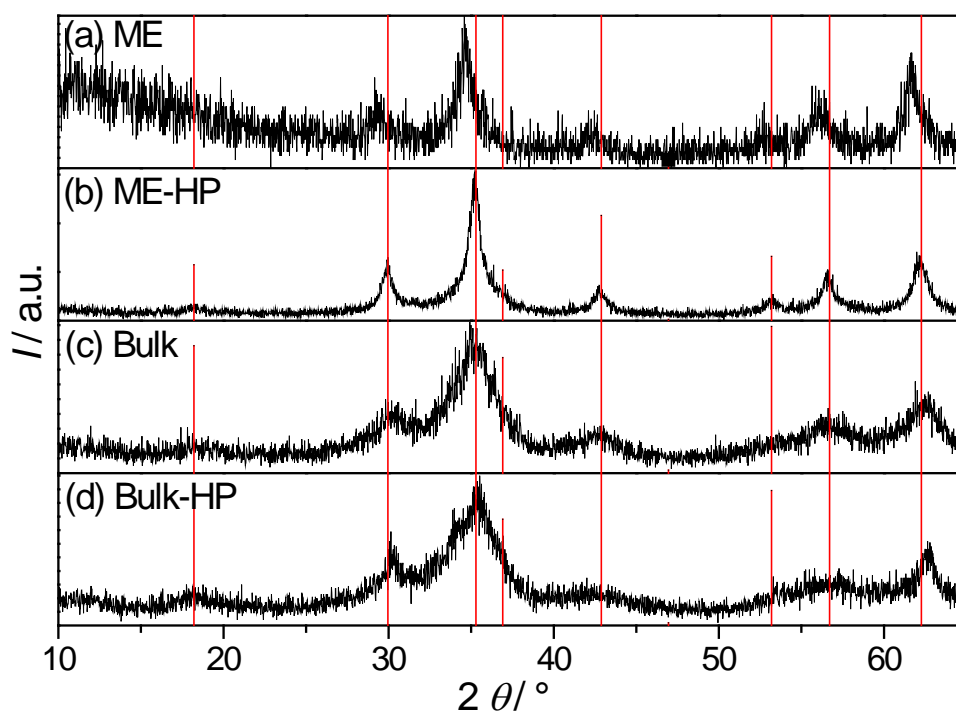
Figure 4.6. Iron-rich zinc ferrite produced with different routes compared with the reference pattern ICDD card no. 01-086-0508: (a) miniemulsion at ambient pressure (ME), (b) miniemulsion under pressure (solvothermal route) (ME–HP), (c) bulk at ambient pressure (bulk), (d) bulk under pressure (solvothermal route) (bulk–HP).

The ICP–MS analysis was performed not only on the six ferrites produced in miniemulsion solvothermal conditions, but also on the iron-rich ferrites produced in bulk–solvothermal

conditions (Table 4.3) to evaluate a possible difference in the stoichiometry and to compare with the information provided by the XRD and the XAS.

Table 4.3. ICP-MS analyses on the iron-rich zinc ferrites synthesized in miniemulsion–solvothermal conditions and bulk–solvothermal conditions.

Synthetic route	[M] / [Fe] Molar
ME–HP	0.305 ± 0.003
Bulk–HP	0.085 ± 0.001

The bulk sample presents a very low amount of zinc compared to the miniemulsion sample, which can be considered a further advantage of the synergetic approach, because it allows a better control of the stoichiometry.

Rietveld refinement conducted on the pattern of the sample prepared by the synergetic approach (Table 4.2) evidences also in this case the presence of two size populations (4 nm: 57%; 13 nm: 43%). However, because of the low signal-to-noise ratio, a precise determination of the cation-site occupancy was not possible.

The enhanced crystallinity of the sample synthesized by the synergy of miniemulsion and solvothermal route may be explained also invoking the Laplace pressure acting on droplets.[5, 6] As discussed in Section 2.2.5, the Laplace pressure is high in the small droplets of the miniemulsion and may induce the crystallization of inorganic systems at lower temperature than usually required (or even at room temperature), without any thermal treatment afterwards.[9, 79] The additional external pressure due to the solvothermal route is likely to enhance this effect. The interfacial tension between the two phases (water with the salts and cyclohexane with PGPR) was experimentally determined with the pendant drop method with an optical goniometer. In Figure 4.7, a plot with the data of surface and interfacial tensions are reported: the values were measured at room temperature and the possible effect of temperature is neglected. The average surface tensions of the pure water and of the solution of salts in water are reported in the equations (4.5) and (4.6); the interfacial tension between water and cyclohexane is shown in eq. (4.7).

$$\gamma_{\text{water–air}} = (70.7 \pm 0.5)\text{mN m}^{-1} \tag{4.5}$$

$$\gamma_{\text{water+salts–air}} = (72.8 \pm 0.6)\text{mN m}^{-1} \tag{4.6}$$

$$\gamma_{\text{water+salts–cyclohexane+PGPR}} = (2.9 \pm 0.7)\text{mN m}^{-1} \tag{4.7}$$

This surprisingly low valued was confirmed by independent measurements of the interfacial tension with the spinning drop method. The Laplace pressure exerted by droplets is given by the Young–Laplace equation:[131]

$$\Delta P_{\text{Laplace}} = P_{\text{inside}} - P_{\text{outside}} = \frac{2\gamma_{\text{water/cylclohexane}}}{r_{\text{droplet}}} \tag{4.8}$$

For ideal spherical droplets of 100 nm of diameter, the resulting value of $\Delta P_{\text{Laplace}}$ is about $1.2 \cdot 10^5$ Pa (1.2 bar). Accordingly, the pressure inside the droplets would be of about 3.4 bar (4.2 bar in the case of nickel, prepared at 100 °C), more than three times higher than atmospheric pressure, which evidences the advantages derived by the synergy miniemulsion–solvothermal conditions. The positive effect of pressure had been already pointed out in the case of simple hydrothermal synthesis of ferrites,[31] by comparing results obtained by using hydrothermal synthesis and by using reflux synthesis conditions at ambient pressure, both at the same temperature. In that case, the beneficial effect of applied pressure in terms of enhanced purity and yield was pointed out.
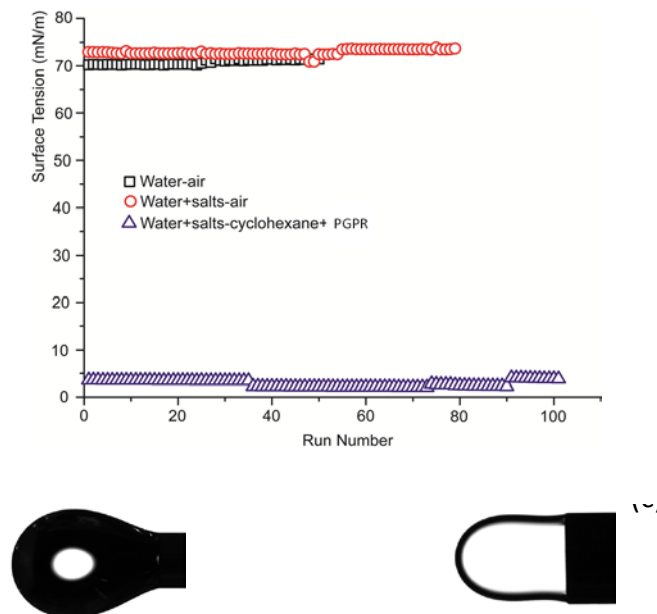
Figure 4.7. Surface and interfacial tension measurement: (a) surface tensions of the different systems as a function of the runs of measurements (b) droplet of water+salts solution in air (c) droplet of water+salts solution in cyclohexane+PGPR solution (images as recorded by the device).

A typical cell volume for a ferrite would be of the order of 590 Å^3, which multiplied by Avogadro's number would lead to a molar volume of $3.55 \cdot 10^{-4}\ \text{m}^3\ \text{mol}^{-1}$. Multiplying the pressure inside the droplets ($3.4 \cdot 10^5$ Pa) by the molar volume, a value of 120.7 J mol^{-1} (ca. 29 cal mol^{-1}) is obtained. We are not aware of reliable data on nucleation and growth activation energies for the studied ferrites, but values of the order of tenths up to hundreds of kilocalories per mol for the nucleation, and of a few kilocalories per mol up to tenths of kilocalories per mol for the growth would be expected. The estimated energy of ca. 29 cal mol^{-1} exerted by the curved interface of the droplet is less relevant for the nucleation process (which occurs anyway also in the bulk solution), but would not be negligible for the growth processes.

As anticipated, the effect of the different routes on the structural evolution and on the growth of the ferrites nanosized particles was also determined on a short-range scale by performing X-ray absorption spectroscopy (XAS) experiments at Elettra synchrotron facility. XAS has been shown a very powerful tool to investigate nanosized ferrites, in particular to determine the cation distribution and thus the inversion degree of these structures.[132] Analyses were performed at both Zn and Fe K-edges to enhance the local chemical sensitivity through a combined picture of both species and corresponding chemical environments. All the Zn K-edge X-ray absorption near-edge structure (XANES) spectra (Figure 4.8) present a white line composed of three peaks, at 9665 (A), 9668 (B) and 9672 eV (C), with a shoulder (D) at about 9679 eV. Features B and D were shown to be indicative of the degree of inversion, with peak B increasing for higher inversion, while shoulder D decreases.[132] In addition, the position of these features slightly decreases in ferrites with higher inversion degrees. The experimental outputs evidence how the cationic distribution is relatively highly inverted for samples prepared by the synergetic approach or the miniemulsion at ambient pressure, while it decreases for the bulk preparation. The sample prepared by simple solvothermal method is likely a fully direct ferrite.

The position of the edge in the Fe K-edge XANES spectra (Figure 4.9) is typical for an oxidation state +3. The pre-edge peak provides valuable information. First, the position of the pre-edge peak is often a preferred way to determine the oxidation state with respect to the edge position, since it is less affected by multiple-scattering phenomena.[133-135] In addition, this peak is symptomatic of the symmetry around the absorber. It arises from a $1s \rightarrow 3d$ transition, which is forbidden by dipole selection rules and hence weak, but the

intensity of which increases for non-centrosymmetric environments, like tetrahedral ones.[136]
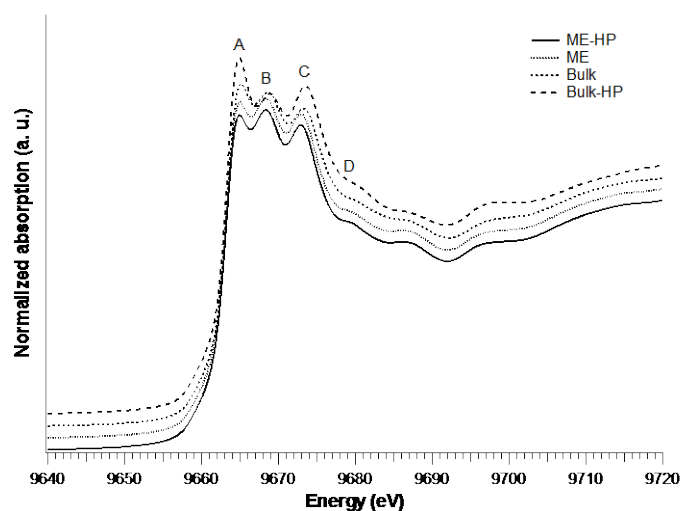
Figure 4.8. Zn K-edge XANES spectra of samples prepared with different synthetic approaches.
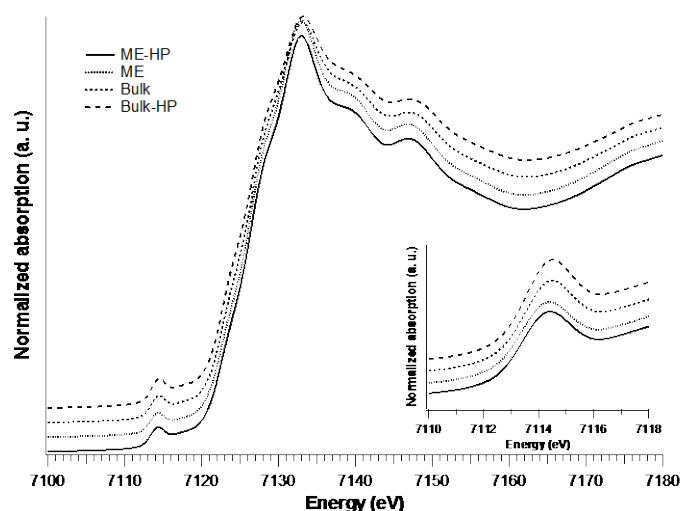
Figure 4.9. Fe K-edge XANES spectra of iron-rich zinc ferrites prepared with different synthetic approaches.

The pre-edge position and relative intensities were analyzed after background removal with an arctangent function[133, 134] and deconvolution with pseudo-Voigt components. Divalent iron ions usually show a pre-edge peak centered around 7112.5–7113 eV, while for trivalent iron ions this is located around 7114–7114.5 eV.[133] The centroid positions determined for the experimental samples confirm an oxidation of +3 for all samples, being centered at 7114.2–7114.3 eV (Table 4.4). A small contribution of Fe^{2+}, limited to less than 4%, is also present, compatible with the ferrite being rich in iron, and thus requiring the presence of divalent iron to keep electroneutrality.

In addition, the pre-edge peak area decreases in going from tetrahedral to octahedral site symmetry.[132-134] The experimental data at Fe K-edge disagree with what had been evidenced by measurements at Zn K-edge, showing an opposite trend. The samples prepared by miniemulsion at ambient pressure or coupled with the solvothermal step show similar pre-edge areas (Table 4.4). Interestingly, the bulk sample show the greatest area, contrary to the indications given by the Zn K-edge. This result is likely to indicate the presence of Fe_3O_4 moieties, not discernible in the XRD diffractograms due to similar patterns.

Table 4.4. Pre-edge characteristics for the Zn ferrites prepared with different synthetic approaches.

Sample	Component / eV	Area / a.u.	Centroid / eV	Total area / a.u.
ME–HP	7112.4	0.005 (3.2 %)	7114.2	0.142
	7114.3	0.138 (96.8 %)		
ME	7112.4	0.005 (3.6 %)	7114.2	0.141
	7114.3	0.136 (96.4 %)		
Bulk	7112.5	0.007 (4.1 %)	7114.3	0.174
	7114.4	0.167 (95.9 %)		
Bulk–HP	7112.5	0.006 (3.8 %)	7114.3	0.159
	7114.4	0.153 (96.2 %)		

To obtain a more detailed description of the zinc ferrites, the fitting of the EXAFS curves, not only of the pre-edge, was also performed. The ferrites were modelled by using two different clusters of atoms, one having the absorber in tetrahedral sites (A sites), and the other having the absorber in octahedral B sites. The distribution among A and B sites was determined by a variable parameter x_A, indicating the fraction of absorber atoms in T_d sites. During the fit, the absorber-backscatterer distance R, the Debye–Waller factors σ^2 and the energy correction E_0 were left free to vary. The coordination numbers N and the amplitude reduction factors S_0 (determined to be 0.75 for Zn and 0.8 for Fe by fitting of

4. Results and Discussion

appropriate standards) were kept fixed. Best fitting parameters for EXAFS curves are reported in Table 4.5.

Table 4.5. Structural parameters determined by fitting of the EXAFS curves registered at Zn and Fe K-edges for iron-rich zinc ferrite samples prepared employing different synthetic approaches.

	Zn K-edge			
	A site (71 %)	N (atoms)	R (Å)	Debye–Waller factors σ^2 (10^{-3} Å^2)
	O	4	1.96	2.5
	Fe	12	3.47	7.3
	O	12	3.50	7.3
	Zn	4	3.62	4.4
ME–HP	B site (29 %)			
	O	6	2.05	2.5
	Zn	6	2.98	7.0
	Fe	6	3.54	7.3
	O	2	3.55	7.3
	O	6	3.75	4.4
	A site (64 %)	N (atoms)	R (Å)	Debye–Waller factors σ^2 (10^{-3} Å^2)
	O	4	1.96	3.4
	Fe	12	3.47	7.4
	O	12	3.50	7.4
	Zn	4	3.62	4.5
ME	B site (36 %)			
	O	6	2.04	3.4
	Zn	6	2.98	7.4
	Fe	6	3.52	7.4
	O	2	3.53	4.5
	O	6	3.73	7.4
	A site (89 %)	N (atoms)	R (Å)	Debye–Waller factors σ^2 (10^{-3} Å^2)
	O	4	1.97	3.2
	Fe	12	3.49	7.1
	O	12	3.52	7.1
	Zn	4	3.64	4.3
Bulk–HP	B site (11 %)			
	O	6	2.05	3.2
	Zn	6	3.03	6.7
	Fe	6	3.55	7.1
	O	2	3.56	7.1
	O	6	3.76	4.3
	A site (81 %)	N (atoms)	R (Å)	Debye–Waller factors σ^2 (10^{-3} Å^2)
	O	4	1.97	2.4
	Fe	12	3.49	9.4
	O	12	3.52	9.4
	Zn	4	3.64	6.6
Bulk	B site (19 %)			
	O	6	2.04	4.0
	Zn	6	3.01	9.2
	Fe	6	3.53	9.4
	O	2	3.54	9.4
	O	6	3.74	6.6

Fe K-edge			
A site (65 %)	*N* (atoms)	*R* (Å)	Debye–Waller factors σ^2 (10^{-3} Å^2)
O	4	1.89	2.8
Zn	12	3.41	14.4
O	12	3.44	14.4
Fe	4	3.57	11.3
B site (35 %)			
O	6	2.02	2.8
Fe	6	2.97	8.5
Zn	6	3.49	14.4
O	2	3.49	14.4
O	6	3.69	11.3
A site (73 %)	*N* (atoms)	*R* (Å)	Debye–Waller factors σ^2 (10^{-3} Å^2)
O	4	1.92	5.6
Zn	12	3.44	15.6
O	12	3.47	15.6
Fe	4	3.59	14.9
B site (27 %)			
O	6	2.04	5.6
Fe	6	3.00	5.3
Zn	6	3.52	15.6
O	2	3.52	15.6
O	6	3.72	14.9
A site (68 %)	*N* (atoms)	*R* (Å)	Debye–Waller factors σ^2 (10^{-3} Å^2)
O	4	1.89	6.5
Zn	12	3.34	21.4
O	12	3.37	21.4
Fe	4	3.49	8.8
B site (32 %)			
O	6	2.03	6.5
Fe	6	2.98	7.5
Zn	6	3.49	21.4
O	2	3.50	21.4
O	6	3.70	8.8
A site (81 %)	*N* (atoms)	*R* (Å)	Debye–Waller factors σ^2 (10^{-3} Å^2)
O	4	1.92	7.5
Zn	12	3.44	16.0
O	12	3.47	16.0
Fe	4	3.60	16.4
B site (19 %)			
O	6	2.04	7.5
Fe	6	3.00	4.6
Zn	6	3.52	16.0
O	2	3.52	16.0
O	6	3.72	16.4

Row labels (leftmost column, spanning each block): ME–HP, ME, Bulk–HP, Bulk.

The Fourier transforms (FTs) of the EXAFS functions recorded at the two different edges are reported in Figure 4.10. The second shell, that is the region between 2 and 4 Å, is particularly meaningful, since it is mainly composed by the cation–cation contributions and can thus provide a qualitative indication of the inversion degree. The distance between

two cations in octahedral sites is about 3.0 Å, whereas for two cations in tetrahedral sites this distance is about 3.65 Å; two cations occupying neighboring octahedral and tetrahedral sites are about 3.5 Å apart (from crystal structure: $M_{O_h} - M_{O_h} = 3.00$ Å, $M_{O_h} - M_{T_d} = 3.51$ Å, $M_{T_d} - M_{T_d} = 3.66$ Å).
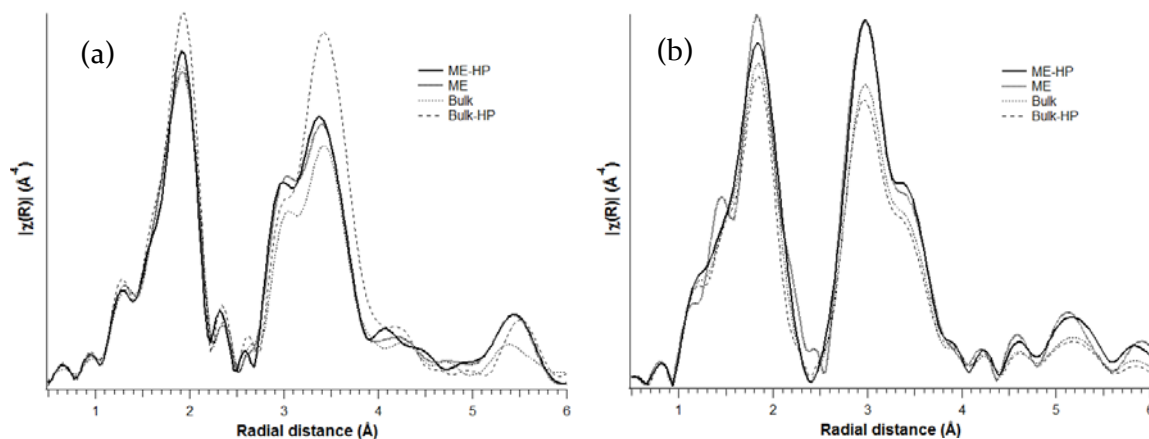
Figure 4.10. FTs of spectra recorded at a) Zn and b) Fe K-edges.

As seen in Figure 4.10a, the second shells in the Zn K-edge FTs are clearly formed by two components. Following the previous reasoning, the presence of a noticeable component at about 3 Å indicates a partially inverted spinel. In agreement with the XANES findings, this component is much less intense in the sample prepared by the simple solvothermal method, indicating that for this sample the inversion degree is lower. This, as outlined, is a very relevant result.

In the Fe K-edge FTs, the inversion degree is mainly evident in the contribution at 3.5 Å, corresponding to the interactions involving tetrahedral sites. For this edge, samples prepared by simple miniemulsion or by the combined approach present a higher occupation of Fe cations in T_d sites, symptomatic of higher inversion.

The Zn-O and Fe-O distances expected from the direct zinc ferrite structure (Zn in T_d A sites, Fe in O_h B ones) are 1.98 and 2.03 Å respectively. For Zn in A sites and Fe in B sites, the metal-to-oxygen bond distances determined by in-depth analysis of the EXAFS curves are, for all samples, in agreement with these values (average values: 1.96 and 2.04 Å respectively). For Zn occupying B sites, an average bond distance of 2.04 Å was determined, slightly shorter than the expected value for divalent zinc in octahedral symmetry (2.10 Å). Finally, the insertion of trivalent Fe ions in the A sites leads to a shortening of M–O distances to about 1.88 Å, in accordance with Fe^{3+} in T_d sites (1.86 Å,

Fe^{2+} in T_d: 2.00 Å). The distances determined for metal–metal interactions were $M_{O_h} - M_{O_h}$=3.00 Å, $M_{O_h} - M_{T_d}$=3.50 Å, $M_{T_d} - M_{T_d}$=3.63 Å.

4.1.5 Synergy of Miniemulsion–Solvothermal Conditions with Different Heating Times: Evolution of the Crystallinity

The synthesis of the samples in miniemulsion under solvothermal conditions at different treatment times (time 0, 3 h, 6 h, 12 h and 24 h) was carried out to understand the effect of the heating time on the structural evolution. In Figure 4.11 the diffractograms collected at different reaction times of the iron-rich zinc ferrite are reported whereas, for sake of comparison, the diffractograms of the other ferrites are shown in the subsequent Figures. As expected, the crystallinity of the samples increases with time, the reflections becoming sharper and more intense. The sample collected at time 0 was centrifuged and washed immediately after the second miniemulsification without placing it at 80 °C and, as demonstrated by its diffractogram, it is poorly crystalline. As reported in Figure 4.11, Zn ferrite synthesized after only 3 h of reaction shows instead a crystalline pattern: this result is interesting in the pursuing of greener synthetic routes, because a crystalline product was achieved after a reaction of just 3 h at 80 °C, without further thermal treatment, only exploiting the non-standard conditions made available by the combination of miniemulsion and the solvothermal routes. Increasing the time of the reaction, other conditions being equal, the reflections become sharper, hence crystallinity increases.
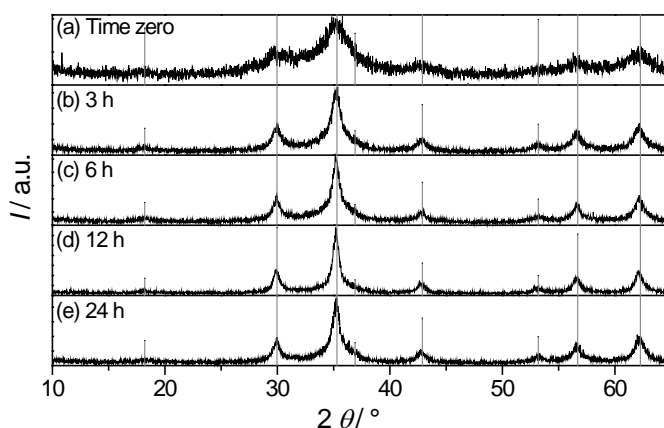
Figure 4.11. Crystallization of iron-rich zinc ferrite synthesized in miniemulsion–solvothermal condition at different reaction times: (a) time zero (b) after 3 h (c) after 6 h (d) after 12 h and (e) after 24 h. The vertical lines are the reference pattern of $(Zn_{0.664}Fe_{0.336})(Fe_{1.934}Zn_{0.066})O_4$ ICDD card no. 01-086-0508.
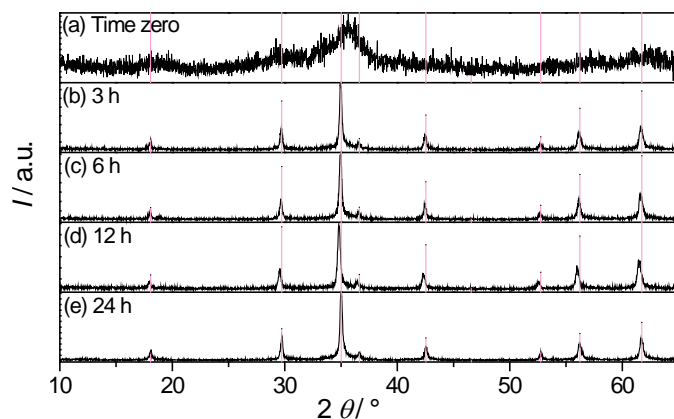
Figure 4.12. Crystallization of $Fe_3Mn_3O_8$ synthesized in miniemulsion–solvothermal conditions at different reaction times: (a) time zero (b) after 3 h (c) after 6 h (d) after 12 h and (e) after 24 h. The vertical lines are the reference pattern of $Fe_3Mn_3O_8$ ICDD card no. 01-075-0034.
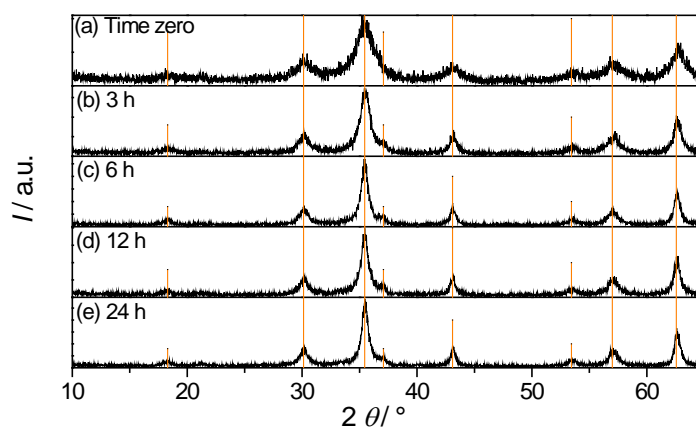
Figure 4.13. Crystallization of Fe_3O_4 synthesized in miniemulsion–solvothermal conditions at different reaction times: (a) time zero (b) after 3 h (c) after 6 h (d) after 12 h and (e) after 24 h. The vertical lines are the reference pattern of Fe_3O_4 ICDD card no. 00-019-0629.
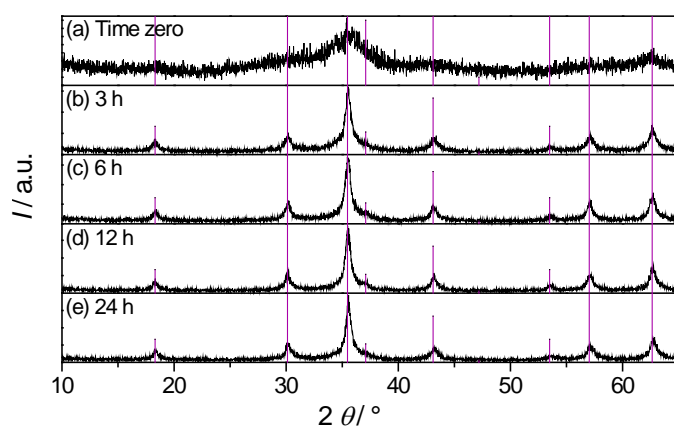
Figure 4.14. Crystallization of $CoFe_2O_4$ synthesized in miniemulsion–solvothermal conditions at different reaction times: (a) time zero (b) after 3 h (c) after 6 h (d) after 12 h and (e) after 24 h. The vertical lines are the reference pattern of $CoFe_2O_4$ ICDD card no. 00-022-1086.
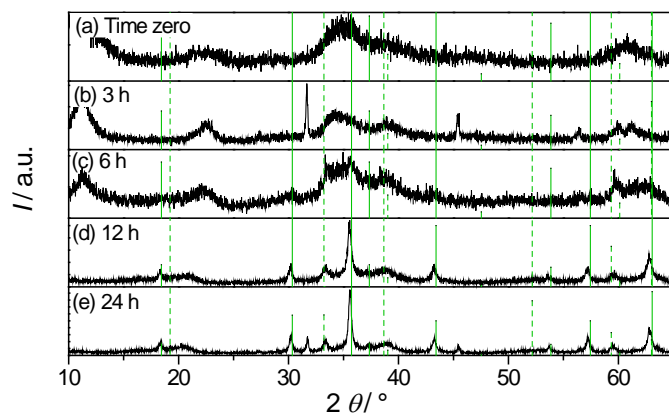
Figure 4.15. Crystallization of $NiFe_2O_4$ synthesized in miniemulsion–solvothermal conditions at different reaction times: (a) time zero (b) after 3 h (c) after 6 h (d) after 12 h and (e) after 24 h. The reference patterns are of $NiFe_2O_4$ (ICDD card no. 00-054-0964, continuous lines) and of $Ni(OH)_2$ (ICDD card no. 01-073-1520, dashed line).
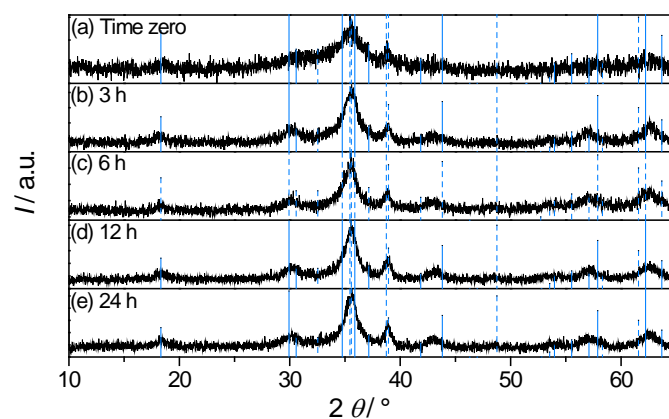
Figure 4.16. Crystallization of $CuFe_2O_4$ synthesized in miniemulsion–solvothermal conditions at different reaction times: (a) time zero (b) after 3 h (c) after 6 h (d) after 12 h and (e) after 24 h. The reference patterns are of $CuFe_2O_4$ (ICDD card no. 01-077-0010, continuous line) and of CuO (ICDD card no. 00-048-1548, dashed line).

The results for all the six ferrites are summarized in Table 4.6, for each series of material, the values of crystallite size determined by the Scherrer formula[90] are constant through all the experiments within the limits of the experimental error, and the size of the crystallites depends strongly on the composition of the ferrite. Mn spinel has the biggest crystallites, followed by $CoFe_2O_4$; Zn ferrite and Fe_3O_4 show a similar size and $CuFe_2O_4$ has the smallest crystallites. $NiFe_2O_4$ starts to show distinguishable reflections after 12 h, so that the Scherrer formula cannot be applied before. The constancy of the values of the crystallite size through all the experiment at different times points out that, even with very short processing time, except nickel ferrite, crystalline and stable materials are produced.

Table 4.6. Crystallite size (*L*), calculated with the Scherrer formula, for all the six ferrites produced in miniemulsion–solvothermal conditions.

Reaction time / h	*L* Mn ferrite / nm	*L* Fe ferrite / nm	*L* Co ferrite / nm	*L* Ni ferrite / nm	*L* Cu ferrite / nm	*L* Zn ferrite / nm
3	37	9	13	—	6	8
6	37	12	14	—	6	10
12	34	11	15	24	7	13
24	36	13	14	29	7	10

The time zero is not reported because all these samples were poorly crystalline and the Scherrer formula could not be applied.

The time-resolved evolution of zinc ferrite nanostructures was also followed by means of Zn and Fe K-edges XAS. The Zn K-edge XANES (Figure 4.17) evidences once more the relevance of the combined miniemulsion and solvothermal approach. The sample at $t = 0$ h, thus not subjected to any solvothermal treatment, indeed shows less defined features with respect to the other samples, indicating that the local structure around the Zn absorber sites is different, in agreement with a poorly crystalline sample. This might also be related to a size effect. With increasing treatment time, on the other hand, no significant difference could be detected, in agreement with the similar crystallite size.
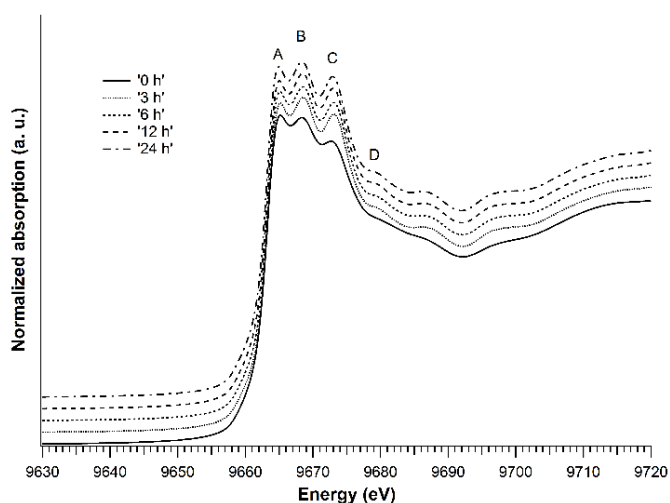
Figure 4.17. Zn K-edge XANES spectra of samples prepared with different reaction times.

In a similar way, the Fe K-edge spectra registered after different reaction times are very similar, except for the starting sample (Figure 4.18). In this case, the pre-edge peak is

slightly more intense than the following samples, indicating a less centrosymmetric local structure.
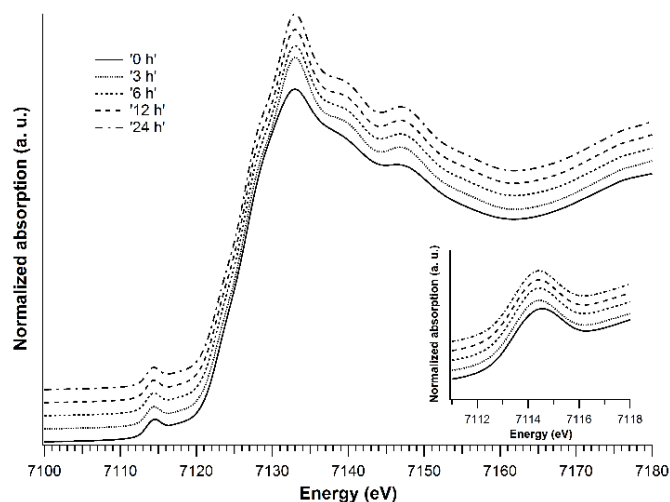
Figure 4.18. Fe K-edge XANES spectra of iron-rich zinc ferrite samples prepared with different solvothermal treatment time.

This is confirmed by the fitting of the EXAFS function, since the Debye–Waller factors determined at both edges for the starting samples are higher than samples synthesized with longer times, due to a more disordered structure, in agreement with a smaller crystallite size (Table 4.7). The pre-edge has been fitted as well and the results are reported in Table 4.8.

Table 4.7. Structural parameters determined by fitting of the EXAFS curves registered at Zn and Fe K-edges for iron-rich zinc ferrite samples prepared with different hydrothermal treatment time.

	Zn K-edge			
	A site (54 %)	N (atoms)	R (Å)	Debye–Waller factors σ^2 (10^{-3} Å^2)
	O	4	1.93	3.0
	Fe	12	3.42	15.6
	O	12	3.44	15.6
	Zn	4	3.57	9.1
0 h	B site (46 %)			
	O	6	2.01	3.0
	Zn	6	2.96	14.1
	Fe	6	3.47	15.6
	O	2	3.48	15.6
	O	6	3.68	9.1
	A site (70 %)	N (atoms)	R (Å)	Debye–Waller factors σ^2 (10^{-3} Å^2)
	O	4	1.96	3.0
3 h	Fe	12	3.47	7.3
	O	12	3.49	7.3
	Zn	4	3.62	5.8

		N (atoms)	R (Å)	Debye–Waller factors σ^2 (10^{-3} Å^2)
	B site (30 %)			
	O	6	2.08	3.1
	Zn	6	2.99	7.1
	Fe	6	3.58	7.3
	O	2	3.59	7.3
	O	6	3.84	5.8
6 h	A site (71 %)	N (atoms)	R (Å)	Debye–Waller factors σ^2 (10^{-3} Å^2)
	O	4	1.96	3.6
	Fe	12	3.47	7.4
	O	12	3.50	7.4
	Zn	4	3.62	6.0
	B site (29 %)			
	O	6	2.08	3.6
	Zn	6	2.99	6.7
	Fe	6	3.59	7.4
	O	2	3.59	7.4
	O	6	3.80	6.0
12 h	A site (71 %)	N (atoms)	R (Å)	Debye–Waller factors σ^2 (10^{-3} Å^2)
	O	4	1.96	3.0
	Fe	12	3.47	6.6
	O	12	3.50	6.6
	Zn	4	3.62	5.1
	B site (29 %)			
	O	6	2.08	3.0
	Zn	6	2.98	6.2
	Fe	6	3.59	6.6
	O	2	3.59	6.6
	O	6	3.80	5.1
24 h	A site (71 %)	N (atoms)	R (Å)	Debye–Waller factors σ^2 (10^{-3} Å^2)
	O	4	1.96	2.5
	Fe	12	3.47	7.3
	O	12	3.50	7.3
	Zn	4	3.62	4.4
	B site (29 %)			
	O	6	2.05	2.5
	Zn	6	2.98	7.0
	Fe	6	3.54	7.3
	O	2	3.55	7.3
	O	6	3.75	4.4
	Fe K-edge			
0 h	A site (74 %)	N (atoms)	R (Å)	Debye–Waller factors σ^2 (10^{-3} Å^2)
	O	4	1.93	7.0
	Zn	12	3.45	22.1
	O	12	3.48	22.1
	Fe	4	3.60	16.5
	B site (26 %)			
	O	6	2.05	7.0
	Fe	6	3.01	8.5
	Zn	6	3.52	22.1
	O	2	3.53	22.1
	O	6	3.73	16.5
3 h	A site (75 %)	N (atoms)	R (Å)	Debye–Waller factors σ^2 (10^{-3} Å^2)
	O	4	1.92	4.5

		N (atoms)	R (Å)	Debye–Waller factors σ^2 (10^{-3} Å²)
	Zn	12	3.44	13.7
	O	12	3.47	13.7
	Fe	4	3.60	17.1
	B site (25 %)			
	O	6	2.05	6.7
	Fe	6	3.01	3.9
	Zn	6	3.52	14.8
	O	2	3.53	14.8
	O	6	3.73	17.6
6 h	A site (79 %)	N (atoms)	R (Å)	Debye–Waller factors σ^2 (10^{-3} Å²)
	O	4	1.92	6.7
	Zn	12	3.45	16.3
	O	12	3.47	16.3
	Fe	4	3.60	21.4
	B site (21 %)			
	O	6	2.04	6.7
	Fe	6	2.99	4.3
	Zn	6	3.51	16.3
	O	2	3.52	16.3
	O	6	3.72	21.4
12 h	A site (75 %)	N (atoms)	R (Å)	Debye–Waller factors σ^2 (10^{-3} Å²)
	O	4	1.93	6.6
	Zn	12	3.45	15.6
	O	12	3.48	15.6
	Fe	4	3.60	18.9
	B site (25 %)			
	O	6	2.04	6.6
	Fe	6	2.99	4.3
	Zn	6	3.51	15.6
	O	2	3.52	15.6
	O	6	3.72	14.0
24 h	A site (65 %)	N (atoms)	R (Å)	Debye–Waller factors σ^2 (10^{-3} Å²)
	O	4	1.89	2.8
	Zn	12	3.41	14.4
	O	12	3.44	14.4
	Fe	4	3.57	11.3
	B site (35 %)			
	O	6	2.02	2.8
	Fe	6	2.97	8.5
	Zn	6	3.49	14.4
	O	2	3.49	14.4
	O	6	3.69	11.3

Table 4.8. Pre-edge characteristics of iron-rich Zn ferrite samples prepared with different reaction times.

Reaction time / h	Centroid position / eV	Normalized area / a.u.
0	7114.4	0.158
3	7114.4	0.154
6	7114.3	0.154
12	7114.3	0.155
24	7114.3	0.152

4.1.6 Morphological, Analytical and Magnetic Characterization of the Transition Metal Ferrites

X-ray diffraction (XRD) results on crystallinity were complemented with morphological investigations by transmission electron microscopy (TEM) (Figure 4.19). The images reported were obtained either by embedding the nanoparticles in an ionic-liquid matrix or by embedding in a trehalose matrix with negative staining of uranyl acetate, as reported in Section 6.4.3. Despite the natural tendency to aggregate upon solvent evaporation, single primary particles are distinguishable. Noticeably, the miniemulsion route has the advantage of yielding samples that are less aggregated than the ones produced in bulk, since the particles are synthesized independently inside the droplets, acting as nanoreactors, and not in a single-event precipitation. Particle sizes were estimated by statistical treatment of TEM images. Two size populations were observed and a mean value was calculated from them (Table 4.9). The average sizes of the two populations are matching the sizes calculated by the Scherrer formula (Table 4.9) and by Rietveld refinement (Table 4.2).
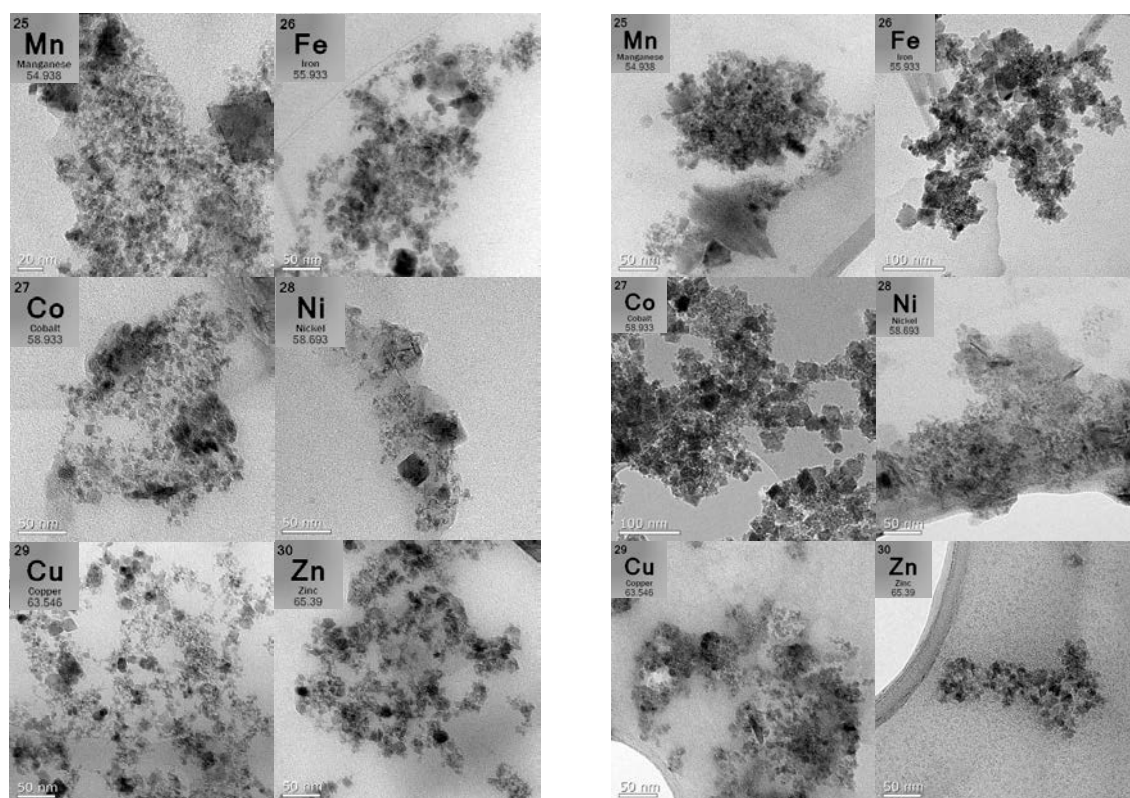
Figure 4.19. TEM images of the ferrites samples: the images are reported in the order of the periodic table. Left side, embedding in an ionic liquid matrix, right side, embedding a trehalose matrix with uranyl acetate staining.

Since the prepared materials are potentially applicable as heterogeneous catalysts, the specific surface area and the porosity, factors affecting the interaction with the substrates, are important features to be investigated. The physisorption of nitrogen at cryogenic temperature and the following calculation with the BET method allow assessing that the produced ferrites are mesoporous materials: their pores have sizes between 2 and 50 nm (Table 4.9 and Figure 4.21). The hysteresis loop (Figure 4.20) is typical of slit-shaped pores, resembling the hysteresis loop H4 reported in the official definition of IUPAC.[94]

Table 4.9. Crystallite size calculated with the Scherrer formula (L), average particle size measured by TEM of the two size populations, specific surface area and average pore diameter of the ferrites synthesized in miniemulsion–solvothermal conditions for 24 h.

Metal present in the ferrite	Reaction temperature / °C	Pressure / kPa	L / nm	Average sizes / nm		Average size / nm	Specific Surface Area / $m^2 g^{-1}$	Average pore diameter / nm
Mn	80	200	36	5±1	11±2	8±2	80	9
Only Fe	80	200	13	6±1	21±9	14±6	93	12
Co	80	200	14	7.1±0.9	11±2	9±2	149	3
Ni	100	300	29	6±1	21±7	13±5	101	5
Cu	80	200	7	6±1	14±2	10±2	173	2
Zn	80	200	10	6±1	12±3	9±3	203	3
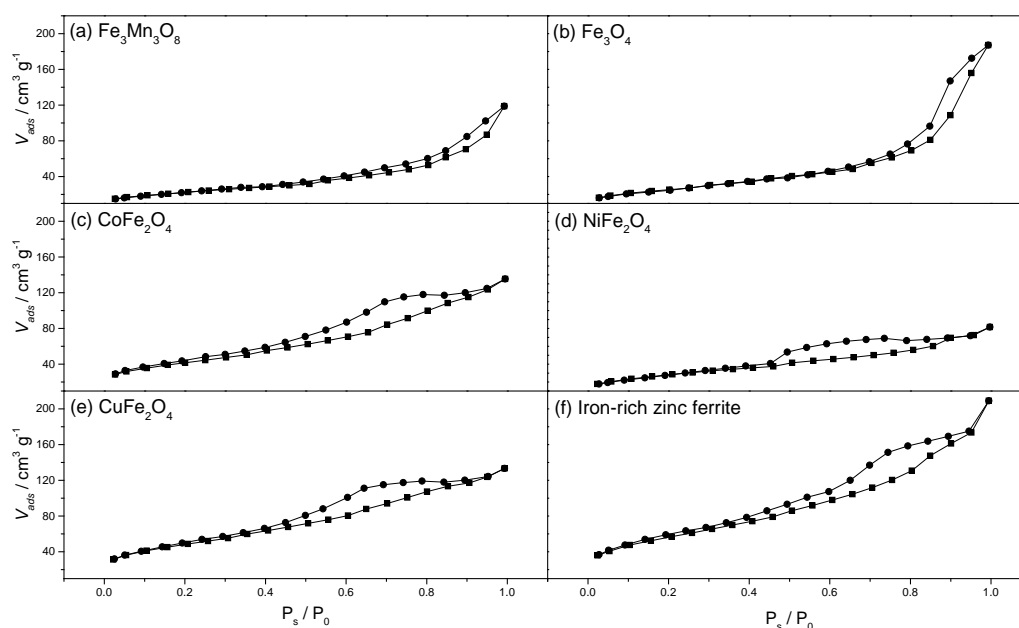
Figure 4.20. Adsorption–desorption BET isotherms for the ferrites synthesized in miniemulsion–solvothermal conditions. (a) $Fe_3Mn_3O_8$ (b) Fe_3O_4 (c) $CoFe_2O_4$ (d) $NiFe_2O_4$ (e) $CuFe_2O_4$ (f) iron-rich zinc ferrite. The hysteresis loops are similar to the H4 loop officially defined by IUPAC, typical of slit-shaped pores.
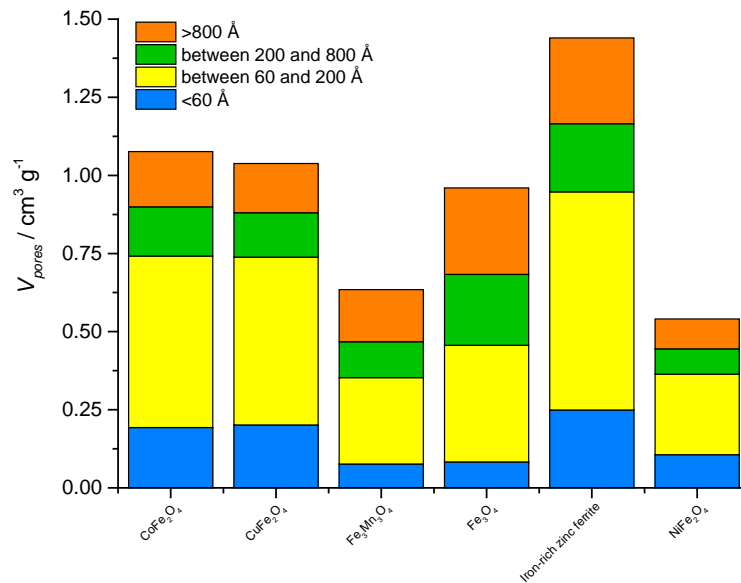
Figure 4.21. Pore size distribution for the different types of ferrites synthesized in miniemulsion–solvothermal.

The theoretical surface area calculated from the sizes obtained by statistical treatment of TEM micrographs was compared with the specific surface experimentally obtained from nitrogen physisorption experiments. Considering the ideal case of spherical and non-porous particles, the specific surface area can be calculated with the following equation:[137]

$$S_{BET} = \frac{6}{\rho\,D} \tag{4.9}$$

ρ is the density of the material (for non-porous solids, the geometric density is considered) and D is the particle diameter. Taking as diameter of a single particle the size measured with the TEM and the density reported in the literature for the materials, the results are reported in the Table 4.10.

The theoretical values, calculated for the ideal case of spherical and non-porous particles from the average size, are—except for the case of the manganese ferrite—generally smaller than the experimentally measured ones, which is an indication of the porosity of the materials that leads to a higher specific surface area.

Table 4.10. Comparison between the specific surface areas calculated from the average particles size measured at the TEM and the ones measured with the BET.

Sample	ρ / g cm^{-3}	D_{TEM} / nm	$S_{calculated}$ / m^2 g^{-1}	$S_{measured}$ / m^2 g^{-1}
Mn ferrite	5.0	8	151	80
Fe ferrite	5.2	14	83	93
Co ferrite	5.3	9	126	149
Ni ferrite	5.3	13	87	101
Cu ferrite	5.4	10	111	173
Zn ferrite	5.3	9	126	203

The experimental specific surface areas for the iron-rich zinc ferrites produced with the different routes were compared as well. In this case, the sample synthesized by the miniemulsion–solvothermal route has the highest specific surface area, followed by the one produced in miniemulsion at ambient pressure and the two samples prepared in bulk solution (Figure 4.22). The hysteresis loops of the bulk samples seem different from the ones of the miniemulsion samples and they resemble more the H2 hysteresis loop officially defined by IUPAC,[94] typical of "ink-bottle" pores (Figure 4.22). Both miniemulsion and bulk materials can be considered as mesoporous.
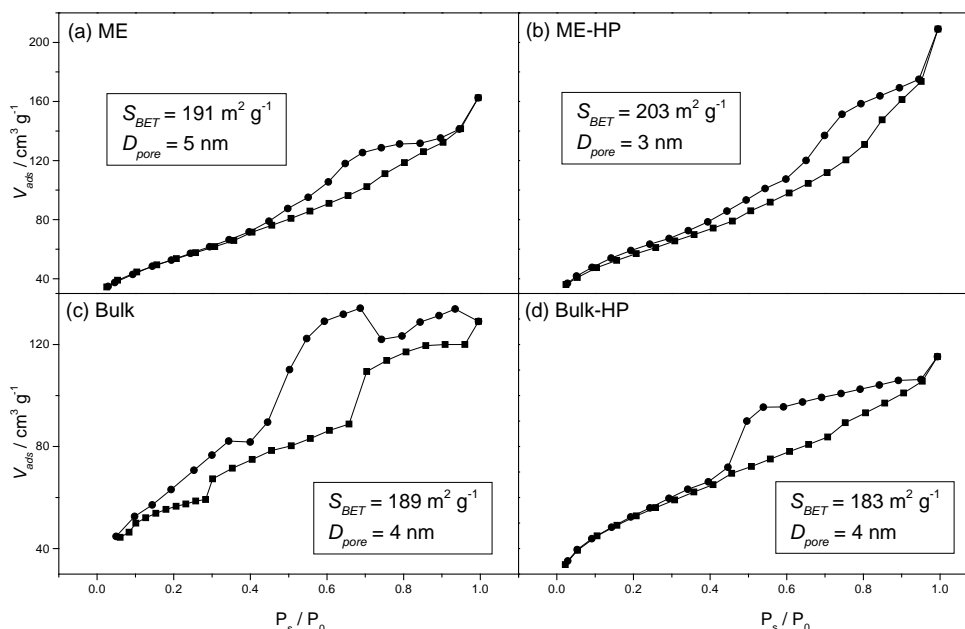
Figure 4.22. Adsorption–desorption BET isotherms for the iron-rich zinc ferrites synthesized in (a) miniemulsion–ambient pressure, (b) miniemulsion–solvothermal conditions, (c) bulk–ambient pressure and (d) bulk–solvothermal conditions. The hysteresis loops of the miniemulsion samples are similar to the H4 loop officially defined by IUPAC, typical of slit-shaped pores, instead for the bulk samples the loops resemble the H2 loop, typical of "ink-bottle" pores.
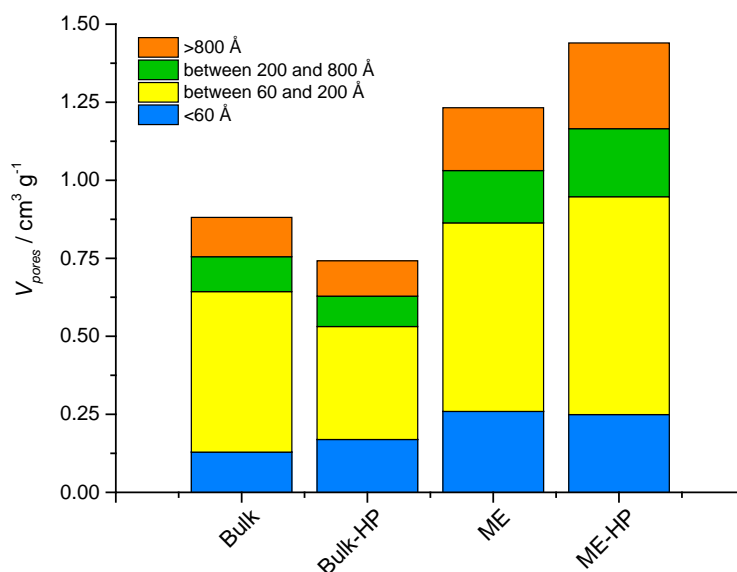
Figure 4.23. Pore size distribution for the four different synthetic routes applied for iron-rich zinc ferrites.

These nanomaterials are well known to have magnetic properties. The room temperature (RT) magnetic behavior of the nanoparticles was characterized by measurements of the magnetic hysteresis in a SQUID magnetometer, as described in the Characterization Methods. Saturation magnetization values for each sample are reported in the corresponding plots (Figure 4.24).

All samples show a superparamagnetic behavior except the $CoFe_2O_4$, which exhibits a ferromagnetic hysteresis loop at RT. The data displayed have been generated by subtraction of the small diamagnetic contribution of an empty capsule that was measured separately. For the Fe_3O_4 nanoparticles, a maximum value of 64 emu g^{-1} is observed at 4 T (i.e., 40000 Oe) that can be compared to a theoretical saturation magnetization for magnetite of 96.5 emu g^{-1} (assuming 4 Bohr magnetons per formula unit (μB/f.u.) in the inverse spinel structure). As nanoparticles possess a high surface to volume ratio and the number of interacting neighbors at a surface is reduced, a reduction of the saturation moment must be expected and is frequently observed.[138]
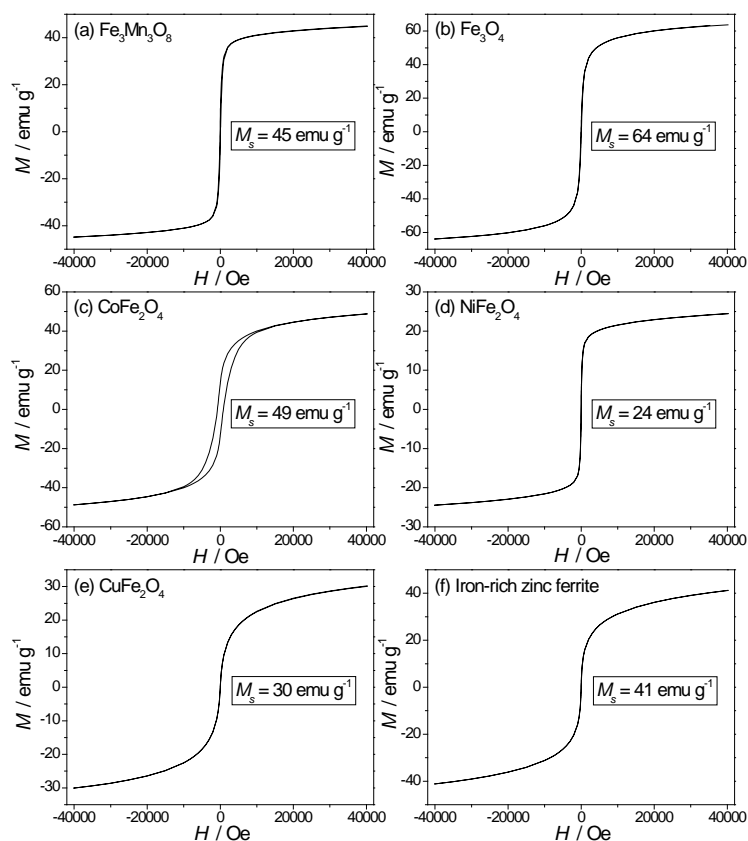
Figure 4.24. Magnetization of the ferrites synthesized in miniemulsion–solvothermal conditions: (a) $Fe_3Mn_3O_8$ (b) Fe_3O_4 (c) $CoFe_2O_4$ (d) $NiFe_2O_4$ (e) $CuFe_2O_4$ (f) iron-rich Zn ferrite. The saturation magnetization values are reported as inset in the corresponding plots.

The measured behavior can be reproduced within the measurement error using a superposition of Brillouin functions calculated for superparamagnetic particles. Indeed, a combination of superparamagnetic particle response of two sizes of nanoclusters plus a paramagnetic response term already yields very good agreement. While one can easily simulate the expected magnetic behavior from a known size distribution, the inverse problem is mathematically ill conditioned. The two different angular momenta J are ascribed to two different superparamagnetic particle sizes in Table 4.11. However, this is not an indication for a bimodal distribution of particle sizes, but rather an estimation of the width of the real distribution. For the superparamagnetic Fe_3O_4 clusters, total angular momenta of $J_1 = 1250\,\hbar$ and $J_2 = 10480\,\hbar$ were found by least square fitting of Brillouin functions with a g-factor $g = 2$ and relative weight 1:2.6. Assuming 4 μB/f.u. of magnetite, the clusters contain 312.5 f.u. and 2620 f.u. which corresponds to ideal particle diameters of 3.6 nm and 7.2 nm. Placing all the remaining Fe ions in a magnetically dead (or paramagnetic) shell around the active cores enhances the diameters to 4.6 nm and 8.2 nm, respectively. The superparamagnetic clusters sizes calculated from the magnetic data are

smaller than the crystallite sizes from X-rays outputs. However, in an X-ray experiment, larger particles of a distribution will dominate as the scattered intensity scales with the scattering amplitude of a particle squared, while the magnetization increases linearly with the particle volume. In addition, a perfect magnetic spin alignment is not guaranteed in the nanoparticles such that the magnetic data rather give lower bounds on the particle sizes. For the other MFe_2O_4 compounds the fitting parameters are given in Table 4.11.

Table 4.11. Fitted clusters sizes and their scale factors as magnetic moment per mass plus the fitted diamagnetic contribution as mass susceptibility (which is paramagnetic and very small compared to the superparamagnetic ones for all samples).

M	J_1 $(\hbar)$	Scale$_1$ $(A\,m^2\,kg^{-1})$ $(=emu\,g^{-1})$	J_2 $(\hbar)$	Scale$_2$ $(A\,m^2\,kg^{-1})$ $(=emu\,g^{-1})$	χ $(4\pi \cdot 10^{-7}\frac{m^3}{kg})$
Mn	8647	35.29	82660	5.24	1.2758
Co	(1143)	29.88	(4483)	15.11	1.4074
Fe	1250	16.20	10480	41.84	1.8469
Ni	8606	11.81	61100	8.79	1.1649
Cu	1031	15.70	11050	8.97	1.8184
Zn	1332	19.46	22290	13.17	2.7845

For the other MFe_2O_4 compounds, an essential magnetic defect is the degree of inversion. For example, for $CuFe_2O_4$ with $Cu(3d^9)$ and $Fe(3d^5)$ in a high spin state, one calculates 9 µB/f.u. (5+5–1) for the normal spinel structure, while the inverse spinel structure has only 1 µB/f.u. (5+1–5).[139] This sets the bandwidth from 24 emu g^{-1} up to 217 emu g^{-1}. We observe 30 emu g^{-1} at $B = 4$ T which points more to an inverse spinel structure and is in agreement with the measurements on ball milled nanoparticles of this compound.[140] For the Zn based sample the observed saturation value of 41 emu g^{-1} at 4 T is in agreement with reported results on $ZnFe_2O_4$ nanoparticles of similar size by Guo et al.[141] A visual inspection of Figure 4.24 shows a most square like hysteresis curve for the Mn (Ni) compounds. The fitted values indicate superparamagnetic moments considerably larger than for the magnetite particles (Table 4.11) as determined from the magnetization curve. Indeed, the evaluation of the X-ray diffraction data (see Table 4.2) yielded the largest particle size for the Mn compound, followed closely by $NiFe_2O_4$, with both values being a factor 2–3 larger than that of the Fe_3O_4 nanoparticles.

A pronounced hysteresis with a coercive field of 80 mT is only observed for $CoFe_2O_4$. For bulk samples a saturation magnetization of 74 emu g^{-1} is observed[142] while high temperature treated nanoparticles of 25 nm size resulted in a saturation magnetization of 61.7 emu g^{-1} and a coercive field of about 50 mT.[143] Our low temperature processed nanoparticles of smaller size show a maximum magnetization at 4 T external field of 49 emu g^{-1}. In summary, the magnetic properties of the nanoparticles prepared by the low temperature solvothermal method are comparable to that of conventionally processed nanoparticles, which renders them suitable for a multitude of applications.

4.1.7 Catalytic Tests

The ferrite nanoparticles produced in miniemulsion are solvent-born and, even after several washings, a part of the surfactant used (PGPR) is still adsorbed on their surface; the particles are thus dispersible in organic solvents. For this important property, a reaction in an organic medium, the oxidation of styrene, was selected to demonstrate the catalytic performances of the synthesized ferrites. This reaction has a strategic application as well: olefin epoxidation is one of the most important processes in the chemical industry and styrene oxide, one of the products (Figure 4.25), is an intermediate for fine chemicals and pharmaceuticals.[144] New efficient and recyclable heterogeneous catalysts for this reaction are therefore sought for.
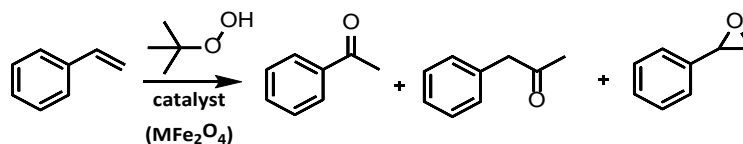
Figure 4.25. Oxidation of styrene with t-butyl hydroperoxide.

Additionally, the ferrites are magnetic particles, therefore are easily separable from the reaction medium and recoverable to catalyze further other reactions. The oxidation reactions were carried out using 1,2-dichloroethane as a solvent because it increases the styrene conversion when compared to the other halogenated solvents.[145] The oxidant employed was t-butyl hydroperoxide in decane, chosen for its dispersibility in the organic solvent. In Table 4.12 the results of the oxidation with different catalysts are reported. With 100% conversion, manganese, cobalt, and copper ferrites display the highest styrene conversion after 24 h. The catalysts are selective mostly for styrene oxide and benzaldehyde (with comparable percentages) and only a small amount of phenylacetaldehyde is produced. The other three ferrites do not show any relevant catalytic activity, since the

styrene conversion is only slightly higher than the one of the blank reaction, performed without any catalyst. A possible reason proposed to explain the different catalytic activity among the tested ferrites is the different amount of oxygen vacancies in the spinel materials that facilitate the adsorption of the peroxide to form the molecular oxygen for the oxidation.[112] A further explanation could be that the Fe^{3+} cation from the octahedral sites of the ferrite reacts with the peroxide molecule to form metal-oxyradical (Fe^{4+}-O) and hydroxyl radicals as an initiation step; these species, which are formed on the surface of the catalyst, will then oxidize the alkene substrates.[146, 147] In certain cases also the other metal of the ferrites can form metal-oxyradical species with a transitional oxidation of the metal.[148]

Table 4.12. Styrene oxidation catalyzed by ferrites produced by the combination of miniemulsion and solvothermal route: conversion and selectivity after 24 h of reaction.

Metal present in the ferrite	Styrene conversion %	Benzaldehyde selectivity %	Phenylacet-aldehyde selectivity %	Styrene oxide selectivity %
Mn	100	48	16	36
Fe	16	27	17	56
Co	100	39	15	46
Ni	15	28	18	54
Cu	100	56	16	28
Zn	8	0	40	60
Blank no catalyst	6	23	9	68

The same oxidation of styrene was performed several times with the same amounts of chemicals and with the same conditions using the same catalysts (Co, Cu and Mn ferrites) from the same batch to test the reproducibility of the results. Those evaluations confirmed, in the range of the experimental error, the results reported in Table 4.12.

The cobalt, copper, and manganese ferrites that showed relevant catalytic activities after a first cycle of reaction were separated from the reaction medium and collected with the help of a neodymium magnet. The recovered catalysts were then washed several times, dried, and employed for other cycles of reaction. Interestingly, the catalyst showed in all the cases (except a little loss of activity and, especially in the case of copper ferrite, a

slightly slower kinetics) an excellent overall conversion, reaching in the case of copper and manganese ferrites 100% of conversion even after the 4th cycle.
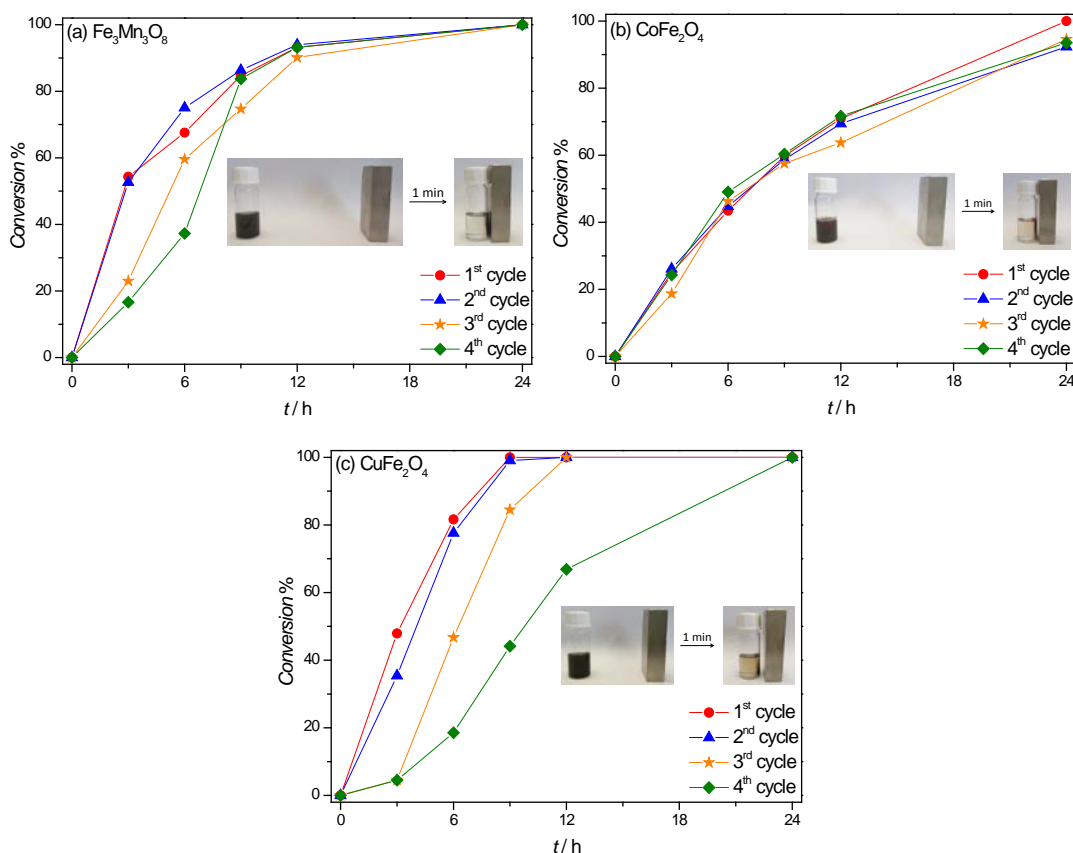
Figure 4.26. Recyclability of the catalysts, ferrites produced by miniemulsion–solvothermal route. Conversion after different reactions with the same catalyst are reported (the solid line is guiding the eye): (a) $Fe_3Mn_3O_8$ (b) $CoFe_2O_4$ (c) $CuFe_2O_4$. The insets show the separation of the catalysts with a magnet.

4.1.8 Synthesis of Transition Metal Ferrites at Different Pressures

The solvothermal conditions for miniemulsion or bulk syntheses of the ferrites have been generally provided by Teflon-lined autoclave reactors (alternatively called "solvothermal bombs"), as described in Section 4.1.2 (Figure 4.1). This kind of reactors, as mentioned in Sections 2.3 and 6.1.2, is simply stainless steel closed vessels with Teflon liners inside. Starting the reaction, the vessel is closed tightly with its own screw cap and it is placed inside an oven at a certain temperature. The evaporation of the solvents at that temperature develops the autogenous pressure inside the reactor. The autogenous pressure, which is also dependent on the filling of the vessel, can be calculated with the Antoine equation.[85] For this inverse miniemulsion system, in a 45 mL autoclave, filled at the 50.1 % of its volume, at 80 °C, the pressure is 2 bar ($2 \cdot 10^5$ Pa) and at 100 °C 3 bar ($3 \cdot 10^5$ Pa), as reported in Section 4.1.2.

4. Results and Discussion

Changing the pressure in the system at a constant temperature is interesting to explore the crystallization of the materials. At higher pressure, it is worthy to find out whether there is a crystallinity improvement at the same temperature (or even at room temperature) and if other phases are achieved or the products are purer. For these purposes, another reactor was employed, namely a stainless-steel high-pressure reactor with a gas inlet to introduce gas (in our case argon) from an external source and increase, in this way, the pressure inside the reactor. The reactor is equipped with a heating body, regulated by a digital controller (to set a precise temperature and heating ramp) and a manometer, directly connected to the reactor, to measure the pressure inside.

The synergetic synthesis of ferrites described in Section 4.1.2 was performed in this high-pressure reactor under argon pressure and at a selected temperature.

Firstly, the synthesis of $CoFe_2O_4$ was performed keeping the same composition of the inverse miniemulsion and the same temperature (80 °C) of the procedure carried out under autogenous pressure, but adding argon inside the closed reactor to reach a pressure of 70 bar ($7 \cdot 10^6$ Pa), as described in Section 6.1.2. By increasing the temperature of the system, also the pressure raised: the pressure measured after 1 h at 80 °C was 78 bar. After 24 h at 80 °C and 78 bar, the miniemulsion was visually stable, no separation of phase occurred even if sedimentation started faster than usual, after few minutes instead of few hours. The higher amount of precipitate is probably caused by the p–T conditions, which increased the yield of the reaction. The stability of the miniemulsion, even in such harsh conditions, is a remarkable result and evidences the possible applicability of the synergy, even for systems requiring higher temperature and pressure to promote the crystallinity. The X-ray diffractogram of $CoFe_2O_4$ obtained at high-pressure is comparable with the one produced under autogenous pressure (Figure 4.27). Both patterns are well defined and match with the reference. The crystallite dimensions, calculated with the Scherrer formula on the reflection (311), are 14 nm in both cases, demonstrating once more that the crystallite dimension does not change significantly by increasing the time of the reaction or, in this case, the pressure, as soon as the crystallinity is achieved. The crystalline spinel phase, once reached, is stable and does not change increasing the pressure, at least at this order of magnitude.
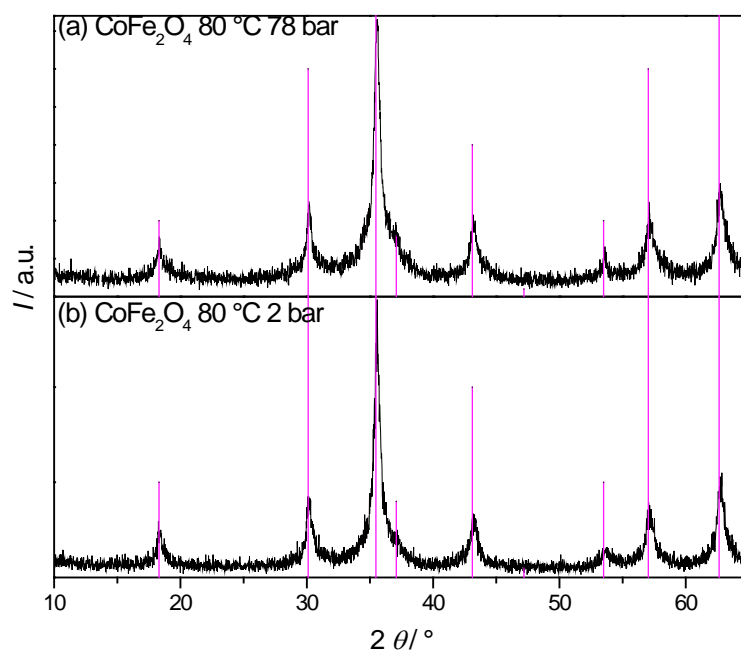
Figure 4.27. X-ray diffractograms of the cobalt ferrite produced by the synergy of miniemulsion–solvothermal route at the same temperature (80 °C) but at different pressures. (a) $CoFe_2O_4$ under 78 bar (70 bar of argon), (b) $CoFe_2O_4$ under the autogenous pressure of 2 bar. The vertical lines are the reference pattern (ICDD card no. 00-022-1086).

$NiFe_2O_4$ and $CuFe_2O_4$ were not obtained as a pure phase under autogenous pressure, but reflections of $Ni(OH)_2$ and CuO were present in their XRD patterns (Figure 4.5). Nickel and copper ferrites were synthesized under argon pressure to investigate the effect of a higher pressure on them.

The miniemulsion containing the nickel ferrite precursors was placed in the autoclave at 100 °C (same temperature of the usual procedure) and under 78 bar of argon pressure. After reaching 100 °C, the pressure raised to 94 bar. After 24 h, the miniemulsion was visually stable and no separation of phase occurred, but sedimentation started less than 2 min after the removal of the miniemulsion from the reactor. The XRD of the nickel ferrite is matching with the one of the sample produced at 3 bar in the solvothermal bomb (Figure 4.28). As already stated for the cobalt ferrite, the spinel phase, once achieved, is stable and does not change with pressure. Also, the crystallite dimension does not change: under autogenous pressure of 3 bar, the dimension of the crystallites calculated with the Scherrer formula is 29 nm, and at 94 bar is 27 nm. $Ni(OH)_2$ is present in the high-pressure sample as well, demonstrating what was asserted in Section 4.1.3: the presence of the hydroxides is not caused by the temperature–pressure conditions but by the pH and the K_{sp} of the hydroxide. Nickel hydroxide and related oxo-hydroxo species precipitate already

at pH 7 and, at the reaction pH (close to 14), they are present as insoluble precipitates and are not decomposed to give ferrites.
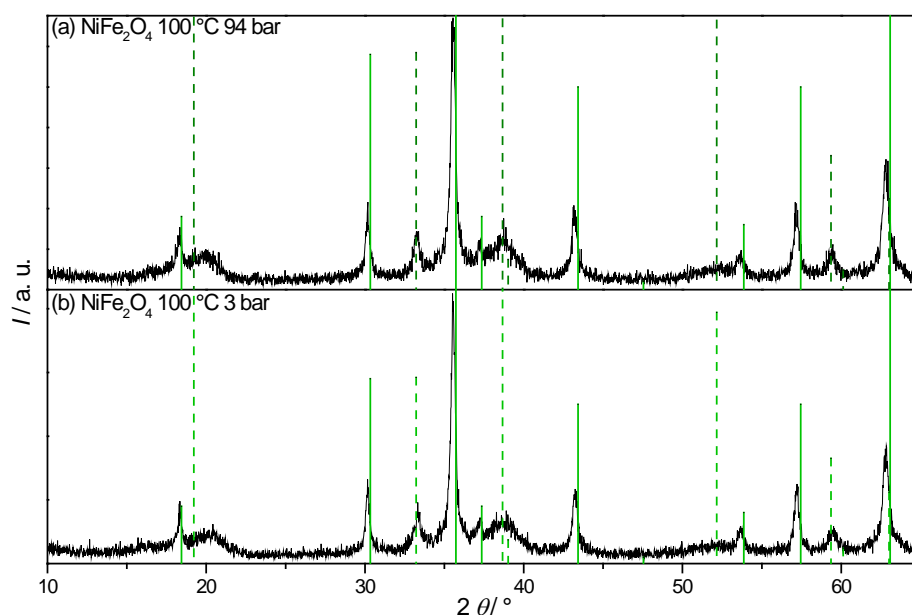
Figure 4.28. X-ray diffractograms of nickel ferrite produced in miniemulsion-solvothermal route, keeping the same temperature (100 °C) and varying the pressure. (a) NiFe$_2$O$_4$ at 94 bar (78 bar of argon) and (b) NiFe$_2$O$_4$ at 3 bar of autogenous pressure. The vertical lines are the reference patterns: the solid lines are the pattern of NiFe$_2$O$_4$ with the ICDD card no. 00-054-0964 and the dashed lines for Ni(OH)$_2$ with ICDD card no. 01-073-1520.

CuFe$_2$O$_4$ was prepared as well under 80 bar of argon pressure at the same temperature usually employed (i.e., 80 °C). As in the other cases, the pressure increased till 92 bar reaching 80 °C. After 24 h, the reaction was stopped and the miniemulsion was initially stable, without phase separation, but also this time the sedimentation occurred quite fast. The diffraction patterns of the copper ferrites are reported in Figure 4.29. The diffractograms are similar, both match with the spinel reference pattern and additionally present the reflections of CuO. As explained for the nickel ferrite, the presence of copper oxide does not seem to be influenced by the pressure, but rather to be caused by the pH conditions. Probably, only higher pressures (in the order of thousands of bars) would cause changes to the phases of the materials. The crystallite dimension remained unchanged as well, 7 nm for the high-pressure copper ferrite, exactly as the autogenous pressure sample.
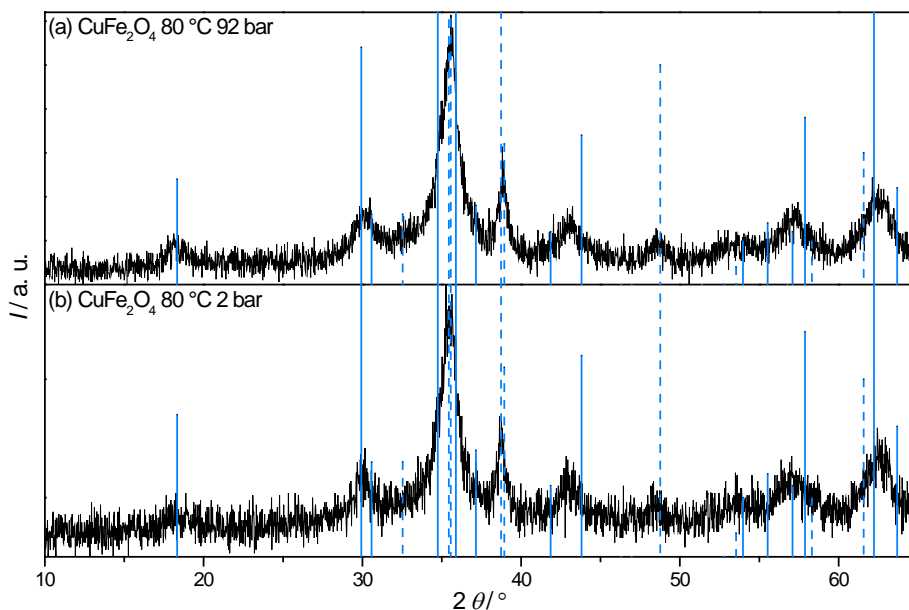
Figure 4.29. X-ray diffractograms of the copper ferrites synthesized in miniemulsion–solvothermal conditions at 80 °C applying different pressures. (a) $CuFe_2O_4$ at 92 bar (80 bar of argon) and (b) $CuFe_2O_4$ at the autogenous pressure of 2 bar. The vertical lines are the reference patterns: the continuous lines are the pattern of $CuFe_2O_4$ (ICDD card no. 01-077-0010) and the dashed lines are for CuO (ICDD card no. 00-048-1548).

All the synthesis carried out heating the system under argon pressure evidenced that the spinel phase is stable and the crystallite dimensions do not change by varying the pressure applied during the synthesis. However, the achievement of the crystalline phase requires energy, as described in Section 4.1.4: iron-rich zinc ferrite presents a defined diffraction pattern only by the combination of miniemulsion and solvothermal conditions (Figure 4.6).

A further proof of the importance of the synergy between miniemulsion and solvothermal route is the synthesis of ferrites in miniemulsion at room temperature and ambient pressure. $CoFe_2O_4$ was prepared with the usual procedure and left aging for 24 h at room temperature. The X-ray diffractogram of this sample shows a pattern with broad reflections (Figure 4.30). The sample does not have a defined composition: it is a mixture of cobalt ferrite, iron and cobalt oxides. The product is crystalline at ambient temperature and pressure probably because the Laplace pressure, acting on the system, is likely to be the driving force of the crystallization, but not enough for the phase selection.
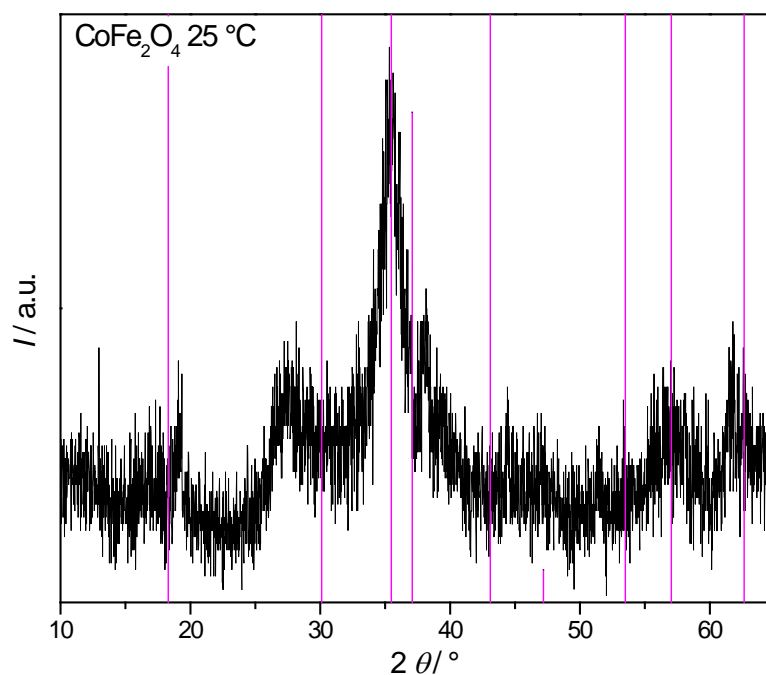
Figure 4.30. X-ray diffractogram of the cobalt ferrite synthesized in miniemulsion at room temperature (i.e., 25 °C) and ambient pressure. The vertical lines are the reference pattern for $CoFe_2O_4$, ICDD card no. 00-02-1086.

Iron-rich zinc ferrite, chosen as model to be comparable with the experiments carried out with the different routes in Section 4.1.4, was prepared in miniemulsion at room temperature under 80 bar of argon pressure in the autoclave. After 24 h at 80 bar, without heating, the miniemulsion was perfectly stable, phase separation or sedimentation did not occur, pointing out that is the temperature or, most probably, the combination of temperature and higher pressure the cause of sedimentation and the destabilization process. The sample recovered was characterized and the corresponding XRD pattern is reported in Figure 4.31. The pattern is well-defined and the reflections perfectly match with the reference pattern for the iron-rich zinc ferrite, even if they are broader than the ones of the sample prepared at 80 °C under autogenous pressure (Figure 4.5 and Figure 4.6). The crystallite size, calculated with the Scherrer formula, is 4 nm, smaller when compared to the dimension for the sample synthesized by miniemulsion at 80 °C under autogenous pressure, which was 10 nm. Nonetheless, the achievement of the crystallinity and phase purity at room temperature only by employing the miniemulsion route and by increasing the system pressure is a remarkable result. Furthermore, the colloidal stability of the miniemulsion under high pressure points out the versatility of this route for materials that require harsher conditions for the crystallinity, providing synthetic confinement and better processability of the products.
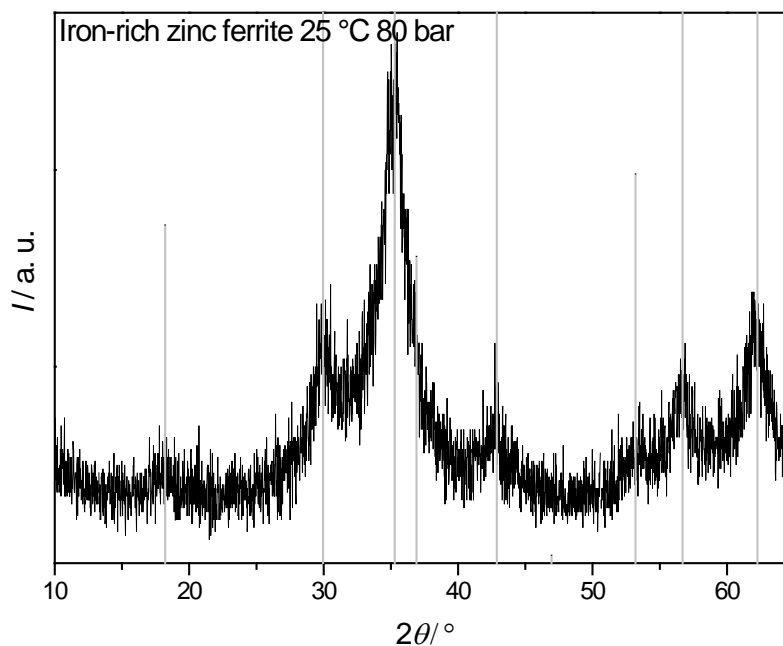
Figure 4.31. X-ray diffractogram of the iron-rich zinc ferrite synthesized in miniemulsion at 25 °C under 80 bar of argon. The vertical line are the reference pattern for $(Zn_{0.664}Fe_{0.336})(Fe_{1.934}Zn_{0.066})O_4$ (ICDD card no. 01-086-0508).

The morphological characterization of the ferrite particles prepared at high pressure was performed by TEM (Figure 4.32). The TEM samples of $NiFe_2O_4$ and iron-rich zinc ferrite were obtained by embedding the nanoparticles in a trehalose matrix with negative staying of uranyl acetate, whereas the sample of $CuFe_2O_4$ was achieved by embedding the material in a matrix of ionic liquid, as reported in Section 4.1.6. Even under high pressure and despite the natural tendency of the products to aggregate upon solvent evaporation, the confinement of the miniemulsion droplets yields well-distinguishable nanoparticles. The size distribution is comparable with the one obtained for samples produced under autogenous pressure. Two size populations are present and the averages of the two size populations are for nickel ferrite is 7 ± 2 nm, for copper ferrite is 11 ± 3 nm and for zinc ferrite 7 ± 3 nm.

In summary, the miniemulsion synthesis of ferrites under high pressure demonstrated the colloidal stability of this system even in hard conditions and its possible applicability to materials, which require higher energy for the crystallization, providing all the advantages of the synthesis in confinement. Especially, the employment of miniemulsion at room temperature and under pressure can be promising as an energy-saving route to produce crystalline materials.
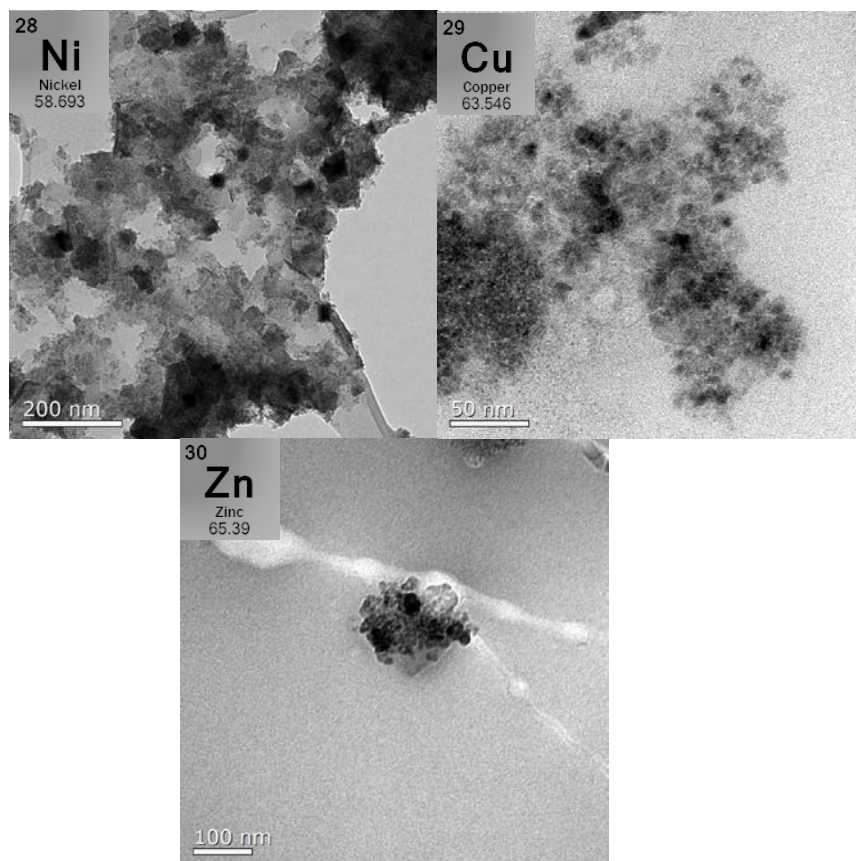
Figure 4.32. TEM images of the ferrites produced in miniemulsion under high argon pressure.

4.1.9 Conclusions

In this section, as a "proof of concept", the synergy between miniemulsion and solvothermal routes for the preparation of crystalline transition metal ferrites was successfully achieved. The confinement of "nanoreactors" provided by miniemulsion droplets and the non-standard temperature and pressure conditions provided by the solvothermal route were proven to be very effective to achieve crystalline metal ferrites at lower temperature (i.e., 80 °C) than usually required and without any post-synthesis thermal treatment. X-ray diffraction (XRD) demonstrated the crystallinity of the six spinel ferrites synthesized. Zinc ferrites obtained with miniemulsion at ambient pressure and with bulk synthesis, either at ambient pressure or under solvothermal conditions, did not result in comparatively highly crystalline samples, outlining the relevance of the combined synthetic approach. X-ray absorption spectroscopy (XAS) evidenced that zinc ferrites produced in miniemulsion are inverse spinels, whereas the samples produced in bulk, especially in the solvothermal bomb are direct spinels. The switch from direct to partially inverse spinel, being the composition equal, it is a relevant result. The reason for this finding could be clarified in future with in situ and time-resolved studies on the

crystallization of these systems. The evolution of the crystallization of the ferrites was followed as well performing ex situ XRD on samples produced with different reaction times. The crystallization of the targeted compound was noticeably achieved already after 3 h of reaction when the combination of miniemulsion and solvothermal route was applied, showing the high potential of this approach in pursuing more sustainable synthetic routes in very short synthesis time. The synergy between miniemulsion and solvothermal conditions was evaluated even varying the pressure applied to the system, keeping constant the temperature. The miniemulsion remained colloidally stable even at 100 °C and almost 100 bar of pressure, outlining its possible application in more severe conditions for materials that require higher energy for crystallization. Crystalline and pure phase iron-rich zinc ferrite was obtained in miniemulsion at room temperature, instead of 80 °C, under 80 bar of argon, opening new scenarios for energy-saving syntheses of materials not requiring heating. Elemental measurements by ICP–MS assessed that the stoichiometries of the ferrites produced by the synergy were not the expected one, MFe_2O_4, in the case of the manganese, nickel and zinc ferrite. In particular, $Fe_3Mn_3O_8$, $(Zn_{0.664}Fe_{0.336})(Fe_{1.934}Zn_{0.066})O_4$ and a mixture between $NiFe_2O_4$ and $Ni(OH)_2$ were selected as compatible compounds, which are in any case all spinel ferrites, clearly except the hydroxide. Measurements of nitrogen physisorption at cryogenic temperature and the corresponding calculations with the BET method displayed that the materials are mesoporous with a quite high surface area, making them suitable for catalytic applications. The ferrites synthesized showed promising functional properties such as superparamagnetism, pointed out by the SQUID (superconductive quantum interference device), and catalytic properties for oxidation of styrene in organic medium, determined following the reactions with the GC–MS (gas chromatography coupled with mass spectrometry). Three of the six ferrites synthesized (manganese, cobalt and copper ferrites), well dispersible in organic media, were proven to be catalytically active and reached 100% of conversion of styrene after 24 h. The ferrites can be furthermore, due to the mentioned magnetic properties, easily recovered from the reaction medium with a magnet and reused for several cycles without losing activity, pointing out a promising recyclability of the material.

4.2 Colloidally Confined Crystallization of Ammonium Phosphomolybdates from Organic and Inorganic Phosphate Sources

In the present section, the water droplets of inverse miniemulsion provided a confined space for the crystallization of another inorganic system after the ferrites, namely the ammonium phosphomolybdates, synthesized from different phosphate precursors. A comparison between miniemulsion and bulk solution synthesis was carried out also in this section to evaluate the effect of the confinement on the particles produced. Both miniemulsion and bulk materials were employed for the epoxidation of *cis*-cyclooctene to tests their catalytic activity and their performances were compared.

4.2.1 Introduction

Ammonium phosphomolybdate, $(NH_4)_3PO_4(MoO_3)_{12}$, was reported for the first time by Berzelius in 1826,[149] and it has been widely exploited in analytical chemistry for the determination of phosphorus.[150] The determination of phosphorus in human fluids, waste water, and soil has been indeed one of the most prominent applications of analytical chemistry since the end of the 19th century. The "molybdenum blue" reaction involves the formation of the polyoxoanion $[PO_4(MoO_3)_{12}]^{3-}$ from sources of molybdenum and phosphate, present in acidic solutions, and the subsequent reduction of Mo^{VI} to Mo^{V} by a reducing agent. The solution is deeply blue and the amount of phosphate present can be determined spectroscopically. The method has been improved over the years but its mechanism has remained quite obscure until nowadays, as explained by Nagul et al. in a recent review.[151]

The structure of ammonium phosphomolybdate remained for many years not well understood until Keggin, in 1934, determined by X-ray diffraction the structure of the phosphotungstate anion,[152] analogous to the one of the phosphomolybdate. Ammonium phosphomolybdate (APM) was one of the first examples of a polyoxometalate (POM), a polyatomic ion formed by transition metal oxo-anions connected by bridging oxygen atoms to create a closed three-dimensional framework composed of vertex-, edge-, or face-connected polyhedra. Its structure, the so-called Keggin structure, is one of the most typical for these compounds. In this framework, the phosphorus atom is at the center of a tetrahedron surrounded by four oxygen atoms. The tetrahedron is caged by 12 MoO_3

octahedra linked together by bridging oxygen atoms. The MoO_3 units are almost equidistant. This regular three-dimensional structure is stable towards hydration and dehydration and to heating up to 400–500 °C. The ammonium ions and the water molecules are probably accommodated between the anion units of the framework. There is a relatively large space between the units, so that larger ions could fit in those positions. Ammonium ions can have an isomorphic exchange with monovalent cations in the crystal lattice, hence the APM can be used as an ion exchanger.[153, 154] The ion-exchange ability of APM is highly important nowadays, especially for the removal of cesium ions after incomplete disposal of radioactive waste deriving from nuclear industry, nuclear weapons test, or nuclear reactor accidents.[155]

Heteropolyacids have been explored in recent years because of their catalytic properties, their easy and affordable preparation, their possibility to be tailored to obtain certain functionalities, their thermal stability, and their non-toxicity.[156, 157] Keggin structures can be multielectron oxidants, can acquire as many as 6 electrons without changing the structure, and are strong Brønsted acids (almost superacids).[158] These characteristics can be exploited in the refinery industry and for fine chemicals production,[156] for instance for the conversion of methanol to hydrocarbons, the desulfurization of diesel,[159] the hydration of olefins, and the oxidation of isobutane to methacrylic acid.[160] Heteropolyacids are soluble in polar solvents and can be applied in homogeneous catalysis, especially when acidity is an important feature.[158] The hydration of propene was the first commercial process based on these catalysts.[161] Ammonium phosphomolybdate is a solid heteropolyacid insoluble in water and concentrated acids (solubility in water at $20 °C = 0.2 \pm 0.1 \, g \, L^{-1}$) but soluble in concentrated bases. The polyoxoanion $[PO_4(MoO_3)_{12}]^{3-}$ is balanced by three ammonium cations and crystallization water molecules are present. Ammonium phosphomolybdate is thermally stable and microporous; therefore it can be employed also for heterogeneous catalysis.[162] It has been as well applied as a photocatalyst for the hydroxylation of benzophenone[163] and for the photodegradation of dyes.[164]

The precipitation of APM, starting from the molybdenum and the phosphate precursors in acid media leads easily to the formation of the rhombic dodecahedral particles: this is a clear example of self-assembly of the Keggin structures through hydrogen bonding.[165-167]

In the present section, we synthesize APM starting from different sources of phosphates, both organic and inorganic, keeping constant the source of molybdenum. By employing

different phosphates, it is possible to test the effects of the counterions (in case of inorganic sources) and the degradation kinetics of the organophosphates on the final structure of the materials, analyzing thereby the influence of the availability of free phosphates ions in solution. Actually, the different availability of the phosphates has been, since the beginning of the 20th century, object of various investigations because it is a key point for the analytical determination of the phosphorus in solution and human fluids (blood and urine). Fiske and SubbaRow[150] proposed a colorimetric method to determine the amount of phosphorus in the human fluids using the ammonium heptamolybdate in acid conditions (concentrated sulfuric acid) and the subsequent reduction of the molybdenum by aminonaphtolsulfonic acid to give a blue mixture (molybdenum blue); the inorganic phosphorus was easily measured in these conditions, while the organic one required a harsher method (i.e., higher temperature and higher acid concentration). Sumner[168] took advantage of this different strength of the phosphate bond and developed a method with ferrous sulfate as reducing agent and lower acidity, providing a greater specificity for the inorganic phosphorus, available also in these conditions. In accordance with these findings, polyphosphoesters require high temperature and low pH to be hydrolyzed. In nature, the dephosphorylation (i.e., removal of the phosphate group from an organic compound by hydrolysis) is catalyzed by specific enzymes, the phosphatases.[169] Our precursors, namely phytic acid dodecasodium salt, D-glucose-6-phosphate sodium salt, and O-phospho-DL-serine have their specific phosphatase, respectively phytase, glucose 6-phosphatase, and phosphoserine phosphatase since they are all involved in important processes for the human body.[170] To the best of our knowledge, the mechanism of formation and the kinetics of precipitation of APM have been so far studied only for different counterions of ammonium salts,[166] but not for different organophosphate sources.

In this section, we also address the influence of the space confinement provided by colloidal systems in the crystallization of APM. More specifically, we study how APM crystallizes within the nanodroplets of water-in-oil miniemulsions. Water droplets of inverse miniemulsions can be exploited as ideal "nanoreactors", as described in Sections 2.2.5 and 4.1. Our working hypothesis is that the synthesis of ammonium phosphomolybdate in the confinement of nanodroplets can provide crystals much smaller than those obtained by bulk crystallization from solution and with enhanced functional properties in the context of heterogeneous catalysis.

4.2.2 Bulk Crystallization from Solution: Effect of the Phosphate Source

The precipitation of ammonium phosphomolybdate starts from an aqueous solution containing ammonium heptamolybdate and a phosphate source, after the addition of a strong acid (HNO_3). In this highly acidic environment (pH < 0, see Table 4.13), phosphomolybdic acid $H_3PO_4(MoO_3)_{12}$ is formed. In the presence of the ammonium ions from the precursor, the yellow ammonium salt hydrate $(NH_4)_3PO_4(MoO_3)_{12} \cdot 4H_2O$ precipitates from solution.

Table 4.13. pH measurements of all the aqueous solutions involved in the bulk synthesis: ammonium heptamolybdate solutions, phosphate source solutions, and mixtures of the two solutions before and after adding nitric acid (pH measured at the end of each reaction).

Sample	pH ammonium heptamolybdate solution	pH phosphate precursor solution	pH mixture of the precursor solutions	pH after adding HNO_3
APM-Na	5.3	4.4	5.8	–0.9
APM-NH$_4$	5.3	4.0	5.7	–0.8
APM-phy	5.3	2.9	5.4	–0.9
APM-glu	5.3	4.2	5.8	–0.8
APM-ser	5.3	1.7	5.5	–0.6

Differently from previous studies,[166, 171] in the present work we investigate the use of different phosphate sources, of both organic and inorganic nature. Five phosphate compounds (see Figure 4.33) were selected to evaluate any potential templating effect of organophosphates with respect to inorganic sources of phosphate, as well as the effect of the phosphate precursor on the kinetics of precipitation and on the final features of the formed materials. Two inorganic phosphate sources (i.e., NaH_2PO_4 and $NH_4H_2PO_4$) and three organic ones (i.e., phytic acid dodecasodium salt hydrate, D-glucose-6-phosphate sodium salt, and O-phospho-DL-serine) were used. In the following, the ammonium phosphomolybdates obtained from the different precursors are labeled as APM-Na (from sodium dihydrogenphosphate), APM-NH$_4$ (from ammonium dihydrogenphosphate), APM-phy (from phytic acid dodecasodium salt), APM-glu (from D-glucose-6-phosphate sodium salt), and APM-ser (from O-phospho-DL-serine).

Differences in the precipitation rates were already macroscopically observable. APM-Na and APM-NH$_4$ started to precipitate immediately upon acid addition and the reaction

medium became deeply yellow. The reaction yield was high in both cases, as reported in Table 4.14. APM-phy precipitated also fast, but the medium was slightly less yellow and the amount of precipitate formed was much lower. In contrast, under the same conditions, the reactions for APM-glu and APM-ser were clearly slower and the yield was still very low after 1 h of reaction.
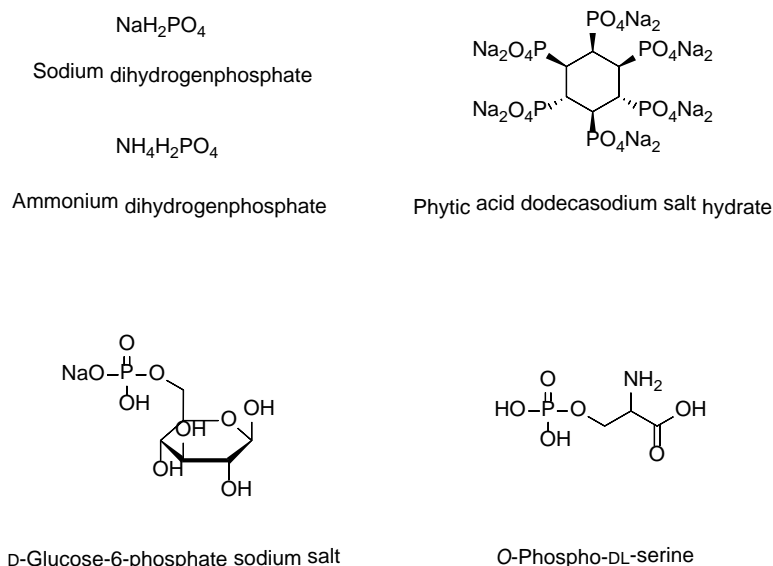
Figure 4.33. Phosphate sources used in this work for the synthesis of ammonium phosphomolybdate.

To quantify the precipitation rates, light transmission was measured by a home-made setup registering the transmitted light of a laser source passing through the reactor vessel in which the crystallization takes place (see Section 6.2.4). As shown in Figure 4.34, different induction times (i.e., time between the mixing of the two solutions and the formation of a crystal that can be detected) are observed for the different systems, following the same trend observed macroscopically. The values of induction time, directly read from the curves and reported in Table 4.14, are very low for the systems containing inorganic phosphate sources (2.7 s for AMP-Na and 0.6 for APM-NH$_4$) and one order of magnitude larger for the APM-glu and APM-ser systems (51.5 and 61.5 s, respectively). Interestingly, when phytic acid dodecasodium salt is used as a phosphate source (APM-phy system), the induction time before precipitation occurs is very similar to the inorganic phosphates (1.1 s).

After the induction time, precipitation takes place and the transmitted intensity decreases rapidly until the medium becomes so turbid that the value approaches to zero. After subtraction of the induction time from the abscissa values, the desupersaturation curves of Figure 4.34 can be well fitted to simple exponential functions of the form:

$$I = I_\infty + Ae^{-kt} \tag{4.10}$$

where the preexponential factor A is fixed to 1 (because the intensity values in the curves are normalized with respect to the value before precipitation starts), I_∞ takes values close to zero, and k is the exponential decay constant (see values in Table 4.14). The values of the desupersaturation constant k differ at least in one order of magnitude when comparing the inorganic sources with the organic APM-glu and APM-ser systems, corresponding to a significantly slower desupersaturation rate in the latter cases. Also in this case, the system APM-phy behaves differently from the other organophosphates, with a desupersaturation constant k more than double than for the inorganic system APM-NH$_4$.

The different induction times and desupersaturation rates can be ascribed to the different availability of the phosphate groups before and at the moment of the precipitation. NaH$_2$PO$_4$ and NH$_4$H$_2$PO$_4$ are inorganic salts that dissociate in water to give phosphate anions, while the organophosphates are phosphoesters in which the phosphate is bound to the rest of the organic part through a C–O bond. In the organophosphates, phosphate groups become available only after hydrolysis of the C–O bond, as mentioned in Section 4.2.1.

Under the reaction conditions, the dephosphorylation of D-glucose-6-phosphate sodium salt and O-phospho-DL-serine requires a certain time to occur, which explains the induction times observed in the turbidity measurements. When the phosphate concentration reaches the required threshold level to form nuclei of a critical size, precipitation starts and the registered light intensity drops rapidly. The precipitation decreases the phosphate concentration in solution and shifts the hydrolysis equilibrium further to the product side. However, as judged from the low yield of the precipitation reaction, the hydrolysis takes place only up to a limited extent. In contrast, at pH 5 (pH of the mixture ammonium heptamolybdate and phosphate) and 80 °C, phytic acid is hydrolyzed very fast.[172] Since there are six phosphate groups (compared to the one single group of D-glucose-6-phosphate sodium salt and O-phospho-DL-serine), the hydrolysis of C–O bond of at least one group can easily occur, making phosphate groups available in the reaction medium. The yield of the precipitation is significantly higher for APM-phy than for APM-glu and APM-ser, but remains far from the values of the inorganic salts (cf. Table 4.14), in which the availability of the phosphate is mainly determined by the solubility equilibrium of salt and not by the hydrolysis of the precursor.

4. Results and Discussion

Table 4.14. Yield (after 60 min), induction time, and empiric parameters of the exponential fitting (cf. eq. (4.10)) of the desupersaturation curves for the crystallization from solution of ammonium phosphomolybdate samples prepared from different phosphate sources (cf. Figure 4.33).

Sample	Yield 60 min (%)	Induction time / s	Exponential fitting of desupersaturation curves	
			I_∞	k / s^{-1}
APM-Na	87	2.7	$(1.2 \pm 0.2) \times 10^{-3}$	1.038 ± 0.005
APM-NH$_4$	92	0.6	$(2.9 \pm 0.7) \times 10^{-4}$	7.333 ± 0.005
APM-phy	28	1.1	$(6.4 \pm 0.2) \times 10^{-4}$	15.035 ± 0.002
APM-glu	3	51.5	$(5.5 \pm 0.2) \times 10^{-3}$	0.10893 ± 0.00012
APM-ser	4	61.5	$(7.6 \pm 0.2) \times 10^{-3}$	0.0806 ± 0.0012
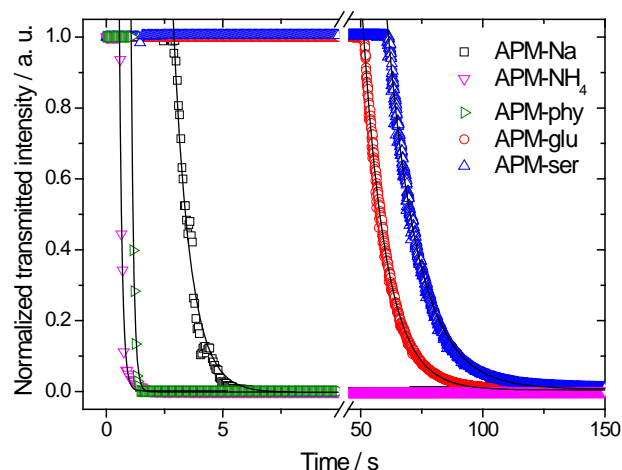
Figure 4.34. Bulk precipitation of the ammonium phosphomolybdate with different phosphate precursors monitored by turbidity measurements: NaH$_2$PO$_4$, NH$_4$H$_2$PO$_4$, phytic acid dodecasodium salt hydrate, D-glucose-6-phosphate, O-phospho-DL-serine.

SEM images of the different samples, presented in Figure 4.35, indicate that the crystals produced in all cases have a rhombododecahedral morphology, but the particle sizes are remarkably different, since the first stages of the reactions (see Table 4.15 for the average particle sizes after different precipitation times), when comparing inorganic and organic phosphate sources (see more detailed discussion on the particles size in the next subsection, Table 4.17). Inorganic phosphate sources lead to particle sizes one order of magnitude larger (average sizes ≥ 10 µm) than organophosphates (average sizes < 3 µm). It is worth to highlight that in the case of particle sizes, the samples prepared with phytic acid dodecasodium salt follow the trend of the other organophosphate and not the one of the inorganic sources. The smaller sizes are consistent with the lower amount of phosphate in the medium (proven by the lower yields of the organophosphates). Phosphate acts as a

limiting reagent and determines the growth of the ammonium phosphomolybdate crystals.
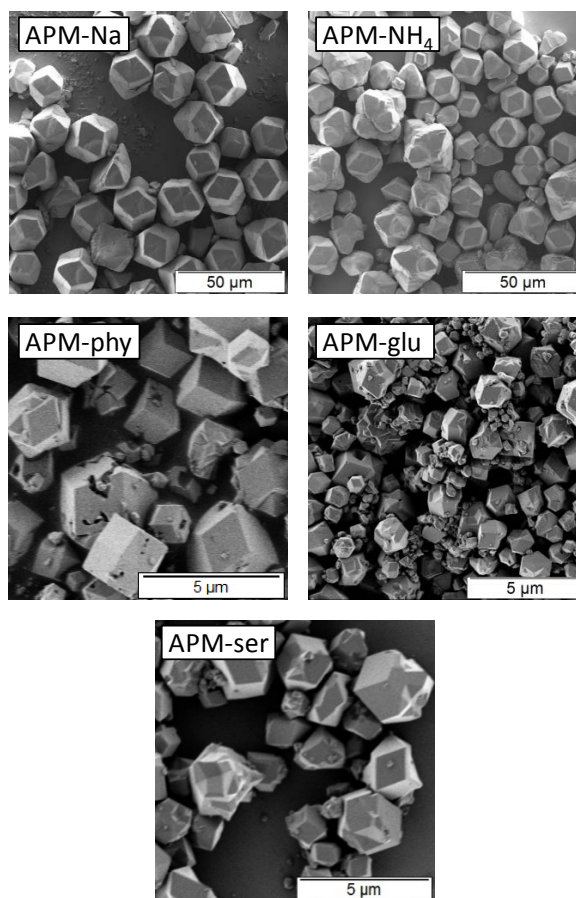
Figure 4.35. SEM micrographs of the ammonium phosphomolybdate particles after 1 h of synthesis. The sample names are reported in the figures.

Sporadically, in SEM images of samples prepared from organophosphates, we observed holes that could point out to the formation of hollow or at least not completely solid structures. To rule out this possibility, we cut a lamella of a crystalline representative sample (APM-glu) under the focused ion beam (FIB) and the corresponding micrograph is shown in Figure 4.36 (see Section 6.4.4). The materials appeared to be solid and we did not observe any hint of hollow structures. High resolution TEM micrographs of the lamella prepared under the FIB indicate clearly the presence of small nanocrystalline domains surrounded by a less crystalline matrix. At the border of the micrometric rhomobododecahedrons the density of the nanocrystalline domains appear to be higher than in the inner part, where the less crystalline matrix becomes more obvious (Figure 4.36(b)-(c)).
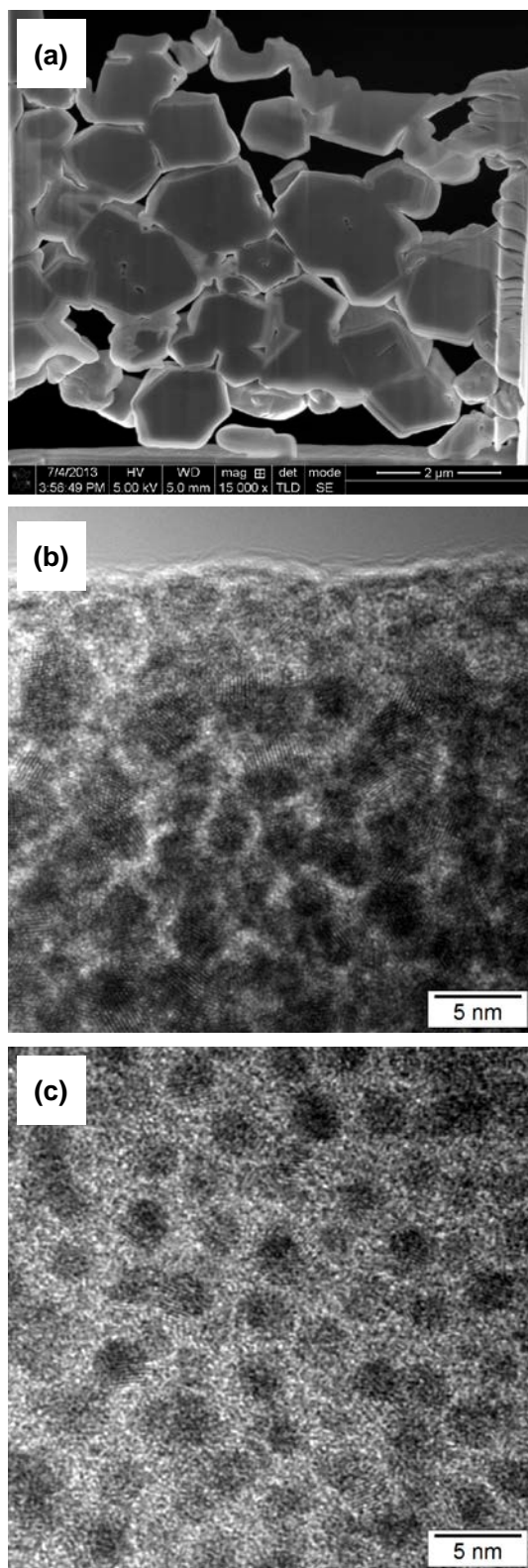
Figure 4.36. (a) FIB micrograph of a lamella of sample APM-glu. (b) High-resolution TEM micrograph of a region close to a border of one of the observed rhombododecahedron microcrystals. (c) High-resolution TEM micrograph of an inner part of the same microcrystal.

Table 4.15. Average size of the ammonium phosphomolybdate particles synthesized in bulk solutions after different precipitation times. The average sizes were calculated on a statistical number of particles measured from SEM micrographs by using the software Fiji ImageJ.

t /min	APM-Na Average size / µm	APM-NH$_4$ Average size / µm	APM-phy Average size / µm	APM-glu Average size / µm	APM-ser Average size / µm
0.5	16 ± 2	10 ± 3	0.5 ± 0.1	—	1.1 ± 0.3
2	14 ± 2	9 ± 2	0.6 ± 0.2	1.1 ± 0.2	1.0 ± 0.4
5	15 ± 1	8 ± 2	1.1 ± 0.2	1.0 ± 0.2	1.1 ± 0.3
20	7 ± 4	10 ± 2	1.4 ± 0.3	1.5 ± 0.3	2.6
60	15 ± 2	10 ± 2	2.5 ± 0.6	0.9 ± 0.2	1.4 ± 0.3

Regardless of the phosphate source used, all the products presented the same X-ray diffraction (XRD) pattern, as shown in Figure 4.37. The reflections match with the reference pattern of cubic $(NH_4)_3PO_4(MoO_3)_{12} \cdot 4H_2O$ (ICDD card no. 00-009-0412). All samples are highly crystalline already in very early stages (see as an example the diffractograms of samples recorded at different reaction times in Figure 4.38). This result is interesting, it evidences how, despite the chemical nature of the used phosphate precursors, the system evolves to the same crystalline structure (i.e., the most thermodynamically stable phase).

Fourier transform infrared (FTIR) spectra were also almost identical for all samples and presented the typical bands of the Keggin structure[173] (Figure 4.39).The vibrational bands of P–O, Mo–O and Mo–O–Mo are positioned at 1063, 963 and 866 cm^{-1}, the P–O deformation vibration at 506 cm^{-1}; the NH_4^+ ions vibration band is assigned to the peak at 1407 cm^{-1}.[174]
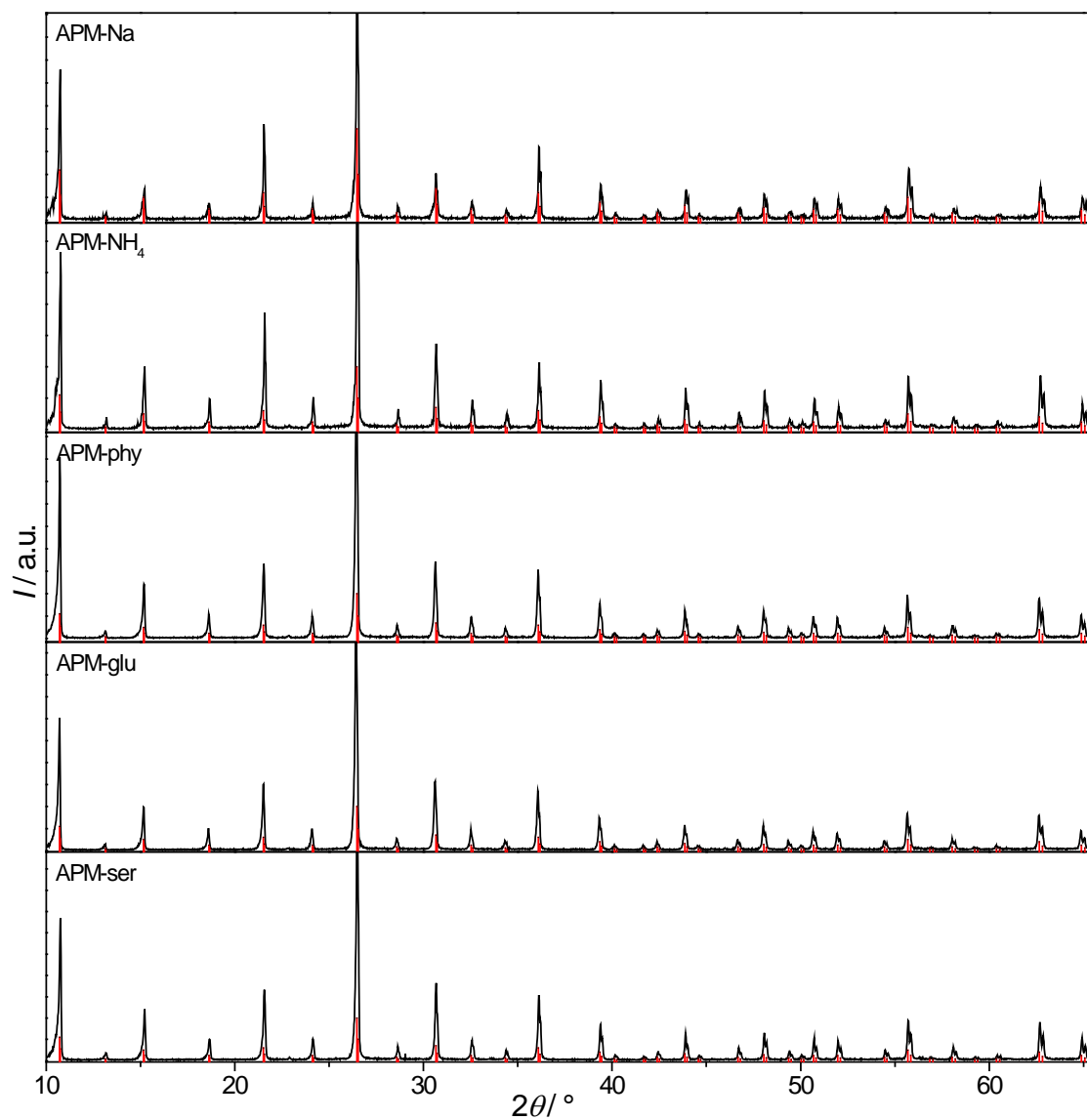
Figure 4.37. X-ray diffractograms of the ammonium phosphomolybdate synthesized in bulk solution for 60 min with different phosphate precursors: the diffraction patterns are perfectly overlapping and matching with the reference pattern ICDD card no. 00-009-0412 (red lines), corresponding to $(NH_4)_3PO_4(MoO_3)_{12}\cdot4H_2O$.
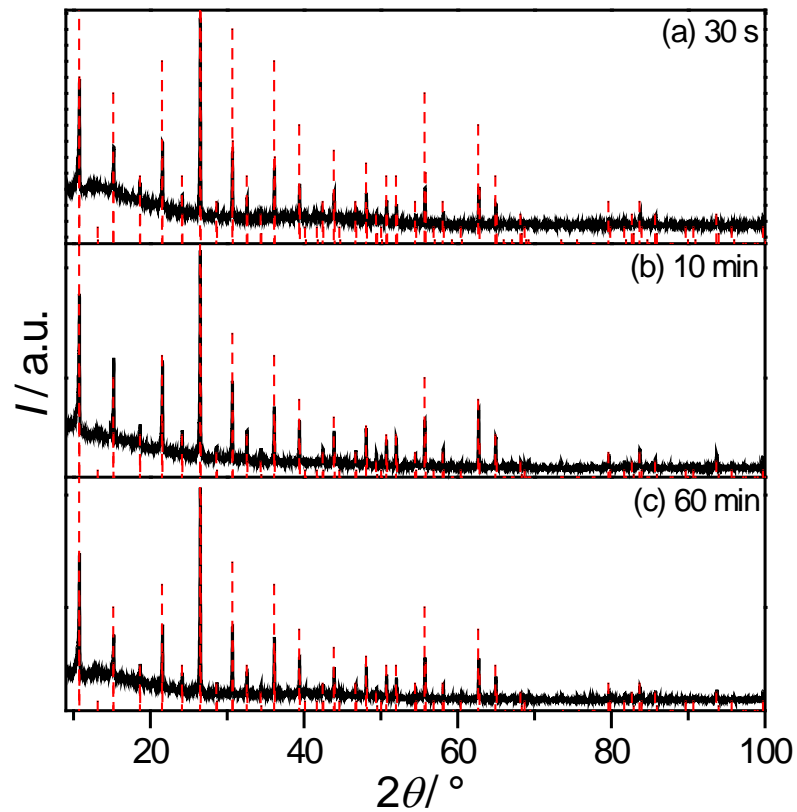
Figure 4.38. Bulk solution synthesis of ammonium phosphomolybdate with $NH_4H_2PO_4$ as phosphate precursor: X-ray diffractograms of samples (a) after 30 s, (b) after 10 min, and (c) after 60 min of reaction, compared with the reference pattern of $(NH_4)_3PO_4(MoO_3)_{12} \cdot 4H_2O$ (ICDD card no. 00-009-0412, dashed red lines).
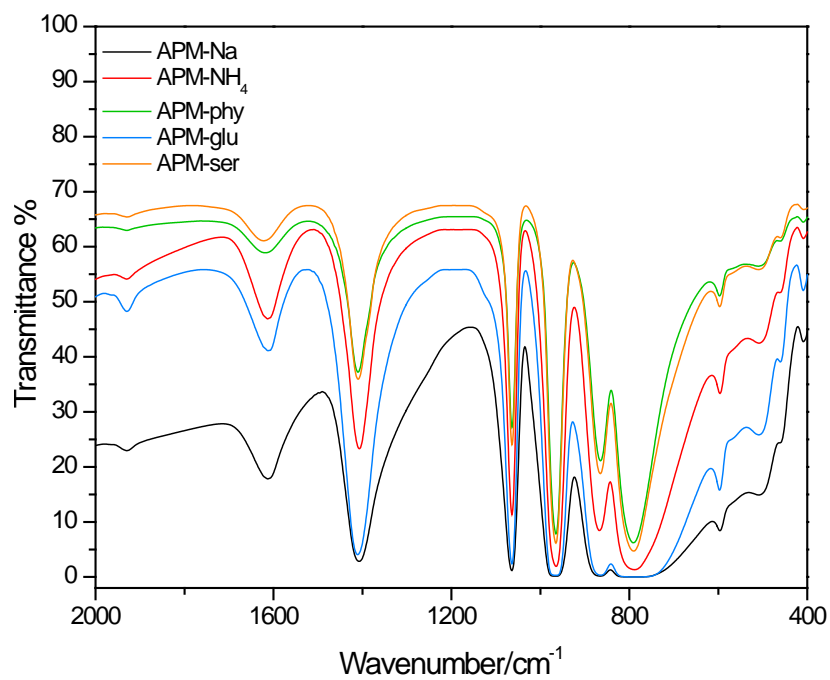
Figure 4.39. FTIR spectra of the ammonium phosphomolybdate synthesized in bulk solution. The bands typical of the Keggin structure can be observed independently from the phosphate employed.

4.2.3 Confined Crystallization within Nanodroplets and Comparison with Bulk Crystallization

The inverse miniemulsion route was employed to study the effect of the space confinement introduced by water nanodroplets on the crystallization of ammonium phosphomolybdate. An inverse miniemulsion is composed of two phases: a dispersed (aqueous) phase and a continuous (organic) phase in which a lipophilic surfactant is dissolved. In our synthesis, the surfactant adopted was a commercial polyglycerol polyricinoleate (PGPR), dissolved in cyclohexane. PGPR, with a low hydrophilic–lipophilic balance (HLB) of around 1.5,[129] was selected as a lipophilic surfactant because it stabilizes efficiently inverse miniemulsions. The disperse phase contained aqueous solutions of our precursors. Ultrasounds were applied to produce high shear forces to drive the miniemulsification of the two-phase system. As in the bulk solution systems, an aqueous solution of nitric acid (14.4 M) was added to the miniemulsion to trigger the precipitation within the water droplets. The system was subsequently ultrasonified a second time to enhance the entrance of the acid in the water droplets (see Section 6.2.3). The droplets behave ideally as independent "nanoreactors" in which the precipitation and the crystallization of the ammonium phosphomolybdate takes place.

The different phosphate sources shown in Figure 4.33 were also used in the miniemulsion approach. The starting miniemulsion of the salts was milky white in all cases after the first emulsification (as common when a transparent solution is miniemulsified). After the addition of nitric acid and the second sonication, the miniemulsion turned immediately intensively yellow for APM-Na-ME and APM-NH$_4$-ME, paler yellow for APM-phy-ME and lightly yellowish white for APM-glu-ME and APM-ser-ME (the label "ME" is used to denote the miniemulsion systems, in contrast to the bulk solution systems).

Light transmission measurements could not be conducted because of the intense scattering resulting from the intrinsic colloidal nature of the miniemulsion, but the yields were comparable to the bulk solution synthesis (APM-NH$_4$-ME: 68%, APM-Na-ME: 72%, APM-phy-ME: 32%, APM-glu-ME: 8%, APM-ser-ME: 8%). As in the bulk samples, although with a much smaller particle size, a rhombododecahedral morphology was obtained in miniemulsion for the inorganic systems APM-Na-ME and APM-NH$_4$-ME. This morphology becomes less evident when organophosphates were employed, as seen in the SEM and TEM micrographs (at different magnifications) presented in Figure 4.40.
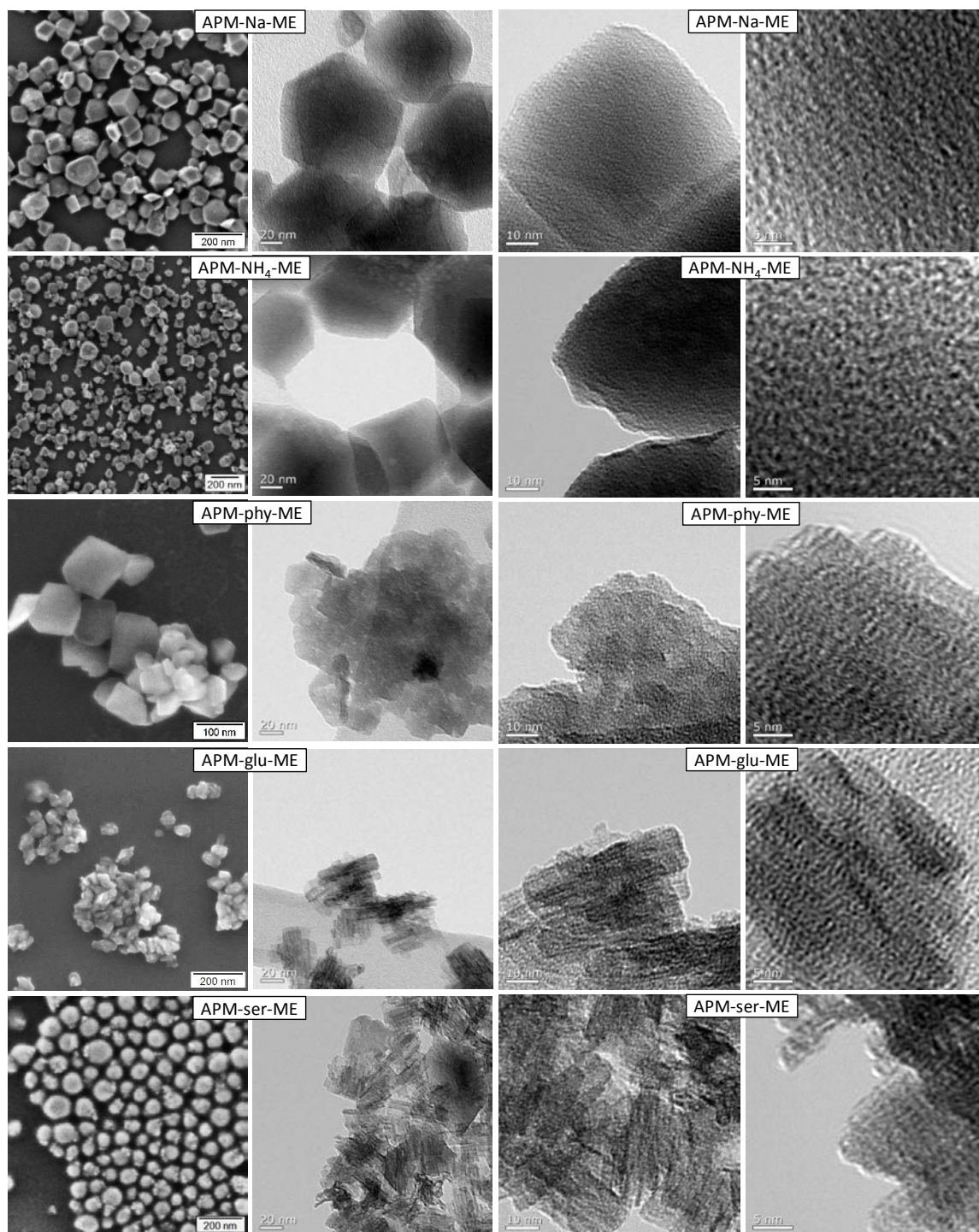
Figure 4.40. SEM and TEM images (first and second column, respectively) of the ammonium phosphomolybdate samples synthesized in miniemulsion with different phosphate precursors. Third and fourth column: higher magnifications of the TEM images of the second column, scale bars at 10 nm and 5 nm.

Also in this case, for all the precursors, the resulting materials were crystalline and the typical reflections of ammonium phosphomolybdate, ICDD card no. 00-009-0412 can be found in the corresponding XRD patterns (Figure 4.41). However, differently from the bulk solution, in the case of APM-glu-ME and APM-ser-ME, additional reflections ascribable to MoO_3 hydrate (ICDD card no. 00-048-0399) and sodium phosphate $Na_2H_2(PO_3)_4$ (ICDD

card no. 00-009-0100) are present. The appearance of theses phases can be explained by the increased pressure within the nanodroplets.
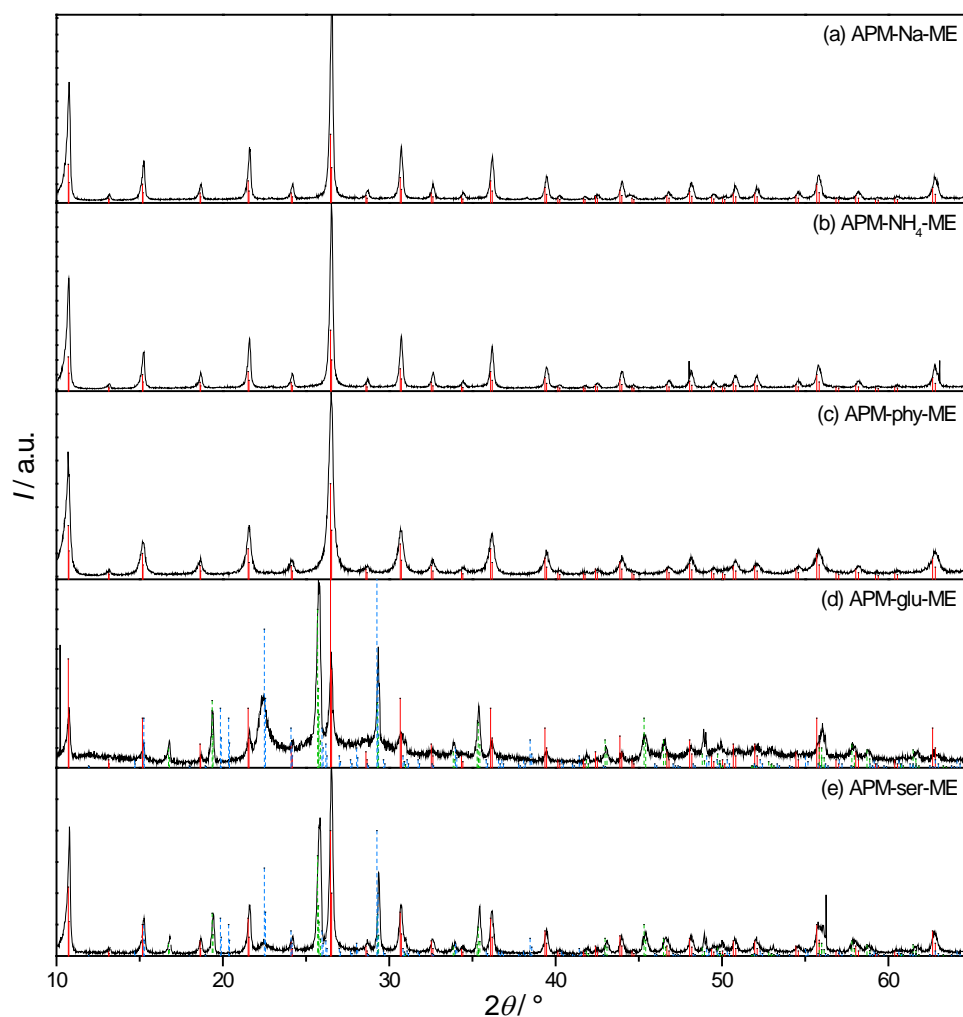
Figure 4.41. X-ray diffractograms of the ammonium phosphomolybdate synthesized with different phosphate precursors in miniemulsion at a reaction time of 60 min. The reflections match with the reference phase $(NH_4)_3PO_4(MoO_3)_{12}\cdot4H_2O$ (ICDD card no. 00-009-0412, red continuous drop lines); (d) and (e) present reflections of MoO_3 hydrate (ICDD card no. 00-048-0399, green dashed lines) and $Na_2H_2(PO_3)_4$ (ICDD card no. 00-009-0100, blue dashed lines).

The crystallization of inorganic materials in the confined space of miniemulsion droplets can occur at milder conditions (lower temperature and pressure) than typically required in bulk, as reported in previous work from our group.[8, 9, 79] Typically, the Laplace pressure (i.e, the pressure difference between the inner and outer part of a curved surface caused by the surface tension at the liquid/liquid interface) is higher for small droplets than for bigger ones, which results in the disappearance of smaller ones in favor of bigger ones (i.e., Ostwald ripening). This molecular diffusion is counteracted in miniemulsion by the presence of an osmotic pressure agent (a substance soluble in the disperse phase—in our case the inorganic salts—but not in the continuous).[5, 6] The interfacial tension between the

two liquid phases (water with the salts and cyclohexane with PGPR) was experimentally determined at 80 °C (i.e., the reaction temperature) with the spinning drop method and a value of 5 mN m^{-1} was obtained (see Table 4.16). The Laplace pressure in the droplets is given by the Young–Laplace equation:

$$\Delta P_{\text{Laplace}} = P_{\text{inside}} - P_{\text{outside}} = \frac{2\gamma_{\text{water/cylclohexane}}}{r_{\text{droplet}}} \tag{4.11}$$

Table 4.16. Interfacial tensions between the two phases of the miniemulsions measured with the spinning drop at 80 °C (reaction temperature) and the Laplace pressures calculated from those values.

Sample	$\gamma_{80\,°C}$ / mN m^{-1}	$\Delta P_{\text{L}\,80\,°C}$ / bar
APM-Na-ME	4.6	1.8
APM-NH$_4$-ME	5.1	2.0
APM-phy-ME	4.1	1.7
APM-glu-ME	5.4	2.2
APM-ser-ME	5.2	2.1

For model spherical droplets of 100 nm of diameter, the resulting value of $\Delta P_{\text{Laplace}}$ is about $2 \cdot 10^5$ Pa (2 bar), doubling the atmospheric pressure, which combined with the presence of the organophosphates can explain the formation of molybdenum oxide in the miniemulsion systems APM-glu-ME and APM-ser-ME.

The average sizes determined by statistical treatment of electron micrographs, reported in Table 4.17, point out that the bulk samples prepared from organophosphates are *significantly* smaller (about one order of magnitude) than the ones prepared from the inorganic phosphates (which has been already explained above), while in the miniemulsion systems there is only a *slight* decrease in size. On the other hand, there is only a small difference in crystallite sizes between organic and inorganic phosphate sources, both in bulk and miniemulsion systems. Interestingly, by comparing crystallite sizes and particles sizes determined by electron microscopy, it can be concluded that the bulk particles are composed by several crystallites, whereas the size of the miniemulsion particles is almost comparable with the corresponding crystallite sizes.

Table 4.17. Average particle size statistically measured from electron micrographs and crystallite size (L) calculated by applying the Scherrer formula for the XRD reflection (222) at 26.5° (reaction time of 60 min).

System	BULK SOLUTION SYNTHESIS		MINIEMULSION	
	Average size / μm	L / nm	Average size / nm	L / nm
APM-Na	15 ± 2	76	90 ± 20	44
APM-NH$_4$	10 ± 2	78	90 ± 20	43
APM-phy	2.5 ± 0.6	67	70 ± 30	36
APM-glu	0.9 ± 0.2	68	43 ± 5	39
APM-ser	1.4 ± 0.3	69	60 ± 20	34

Inductively coupled plasma mass spectrometry (ICP–MS) and elemental analysis were carried out to determine the molybdenum/phosphorus and molybdenum/nitrogen molar ratios for bulk solution and miniemulsion systems. Thermogravimetric analysis (TGA) was also performed to estimate the number of molecules of the hydration water present in the resulting products (see Figure 4.42 and Figure 4.43). The stoichiometry of the ammonium phosphomolybdate corresponding to the reference to which the XRD patterns have been ascribed is $(NH_4)_3PO_4(MoO_3)_{12}\cdot4H_2O$, which should correspond to a Mo/P ratio of 12, a Mo/N ratio of 4, and a hydration of 4 water molecules per formula unit. Table 4.18 presents the experimental values of Mo/P and Mo/N ratios and the hydration stoichiometries for the different samples.

All the TGA thermograms display the same features, independently of the different phosphates used as precursors. The curves are comparable with the typical one of ammonium phosphomolybdate reported in literature.[174] Up to 200 °C, the weight loss is attributed to the removal of the adsorbed and crystallization water; between 400 and 600 °C, the weight loss is associated to the decomposition of the APM and the release of ammonia upon decomposition of ammonium ions. Simultaneously the crystallization of P_2O_5 and MoO_3 takes place, detected above 700 °C.
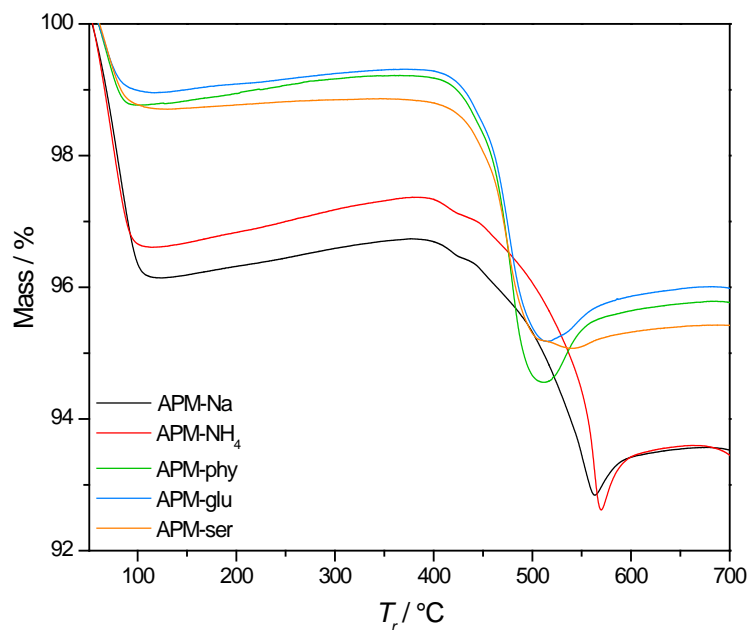
Figure 4.42. TGA diagram of the ammonium phosphomolybdates synthesized in bulk solution with different phosphate sources.
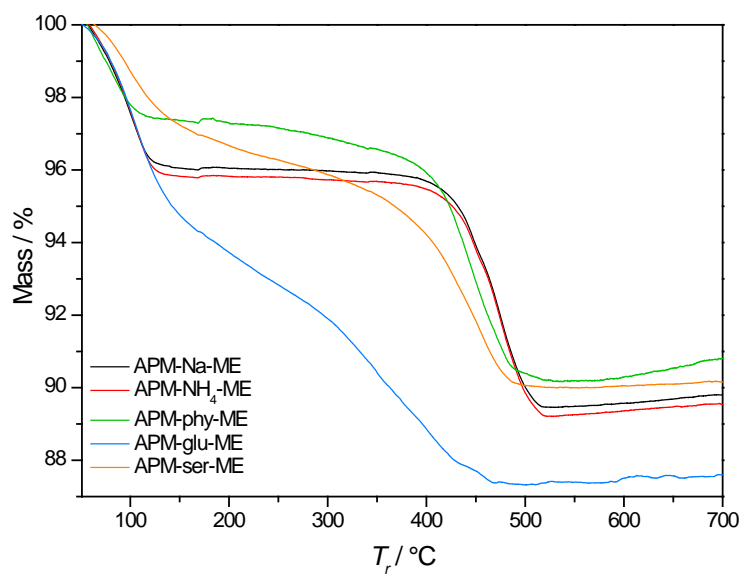
Figure 4.43. TGA diagram of the ammonium phosphomolybdates synthesized in miniemulsion with different phosphate sources.

For all samples, the amount of molybdenum is higher than the expected stochiometric values of the formula $(NH_4)_3PO_4(MoO_3)_{12} \cdot 4H_2O$. Furthermore, the miniemulsion systems show a higher amount of molybdenum compared to the bulk solution systems. From the observation of the TEM micrographs in Figure 4.36, we had argued the presence of a less crystalline phase surrounding nanocrystals. This argument may explain, at least partially, the higher molybdenum content when compared to the theoretical stoichiometric one of the crystalline phase. It is also worthy to mention that samples produced from

organophosphates may crystallize, as mentioned above, under conditions of phosphate deficiency, because of a partial hydrolysis of the precursor. The non-negligible amount of carbon in the samples produced in miniemulsion from organophosphates is ascribable to the unreacted organic precursor trapped in the materials during crystallization within the droplets.

The hydration stoichiometries determined by TGA for bulk samples follow a different trend from those prepared in miniemulsion. In samples prepared in bulk from organophosphates, the calculated number of crystallization water molecules is approximately 2, half than the expected stoichiometry (4), while for the samples prepared from the inorganic phosphates the value is slightly higher than 4. For samples prepared in miniemulsion, the crystallization water is close to 5 for the inorganic systems and close to 4 for the sample prepared from phytic acid. For the other two organophosphates, the presence of additional phases prevents a reliable calculation of the stoichiometry.

Table 4.18. Analysis of the stoichiometry of the samples.

System	BULK SOLUTION SYNTHESIS				MINIEMULSION			
	Hydration stoichiometry[a]	Mo / P	Mo /N	C / at. %	Hydration stoichiometry[a]	Mo / P	Mo /N	C / at. %
APM-Na	4.8	16.4 ± 0.3	5.3 ± 0.2	<LOD[b]	4.9	29.3 ± 0.6	7.12 ± 0.08	0.09 ± 0.01
APM-NH$_4$	4.5	16.6 ± 0.6	5.3 ± 0.2	<LOD[b]	5.1	26.6 ± 0.3	5.91 ± 0.02	0.04 ± 0.02
APM-phy	2.1	14.9 ± 0.6	5.2 ± 0.4	0.02	3.7	19.9 ± 0.4	6.04 ± 0.04	0.616 ± 0.008
APM-glu	1.9	15.1 ± 0.7	5.2 ± 0.5	0.117 ± 0.008	n.d.[c]	441 ± 3	8.30 ± 0.08	0.556 ± 0.008
APM-ser	2.0	14.3 ± 0.3	5.1 ± 0.5	0.06 ± 0.02	n.d.[c]	71 ± 2	6.95 ± 0.06	0.34 ± 0.02

[a] Obtained from TGA measurements;
[b] < LOD: lower than limit of detection;
[c] n.d.: not determined (because there is no definite weight loss step clearly corresponding to the crystallization water).

The prepared materials are exploitable as heterogeneous catalysts and as ion-exchanger for separation and purification. For these applications, the specific surface area and the porosity are key factors. Table 4.19 lists the specific surface area, the average pore size, and total pore volume, calculated according to the physisorption of nitrogen at cryogenic

temperature following the BET theory. All samples are mesoporous, with pore sizes between 2 and 50 nm[94] (Figure 4.45 and Figure 4.44).The specific surface are is in general higher for the inorganic precursors, although the value of the system APM-phy-ME is also comparable to the inorganic systems.

Table 4.19. Specific surface area, average pore size and total pore volume for the ammonium phosphomolybdate produced with different phosphate precursors either in bulk or in miniemulsion with a reaction time of 60 min.

	BULK SOLUTION SYNTHESIS			MINIEMULSION		
	Specific surface area / $m^2\,g^{-1}$	Average pore diameter / nm	Total pore volume / $cm^3\,g^{-1}$	Specific surface area / $m^2\,g^{-1}$	Average pore diameter / nm	Total pore volume / $cm^3\,g^{-1}$
APM-Na	189	2	0.1	126	1	0.45
APM-NH$_4$	152	2	0.08	182	7	0.34
APM-phy	75	4	0.08	164	4	1.48
APM-glu	34	2	0.02	49	6	0.08
APM-ser	68	3	0.05	79	9	0.17
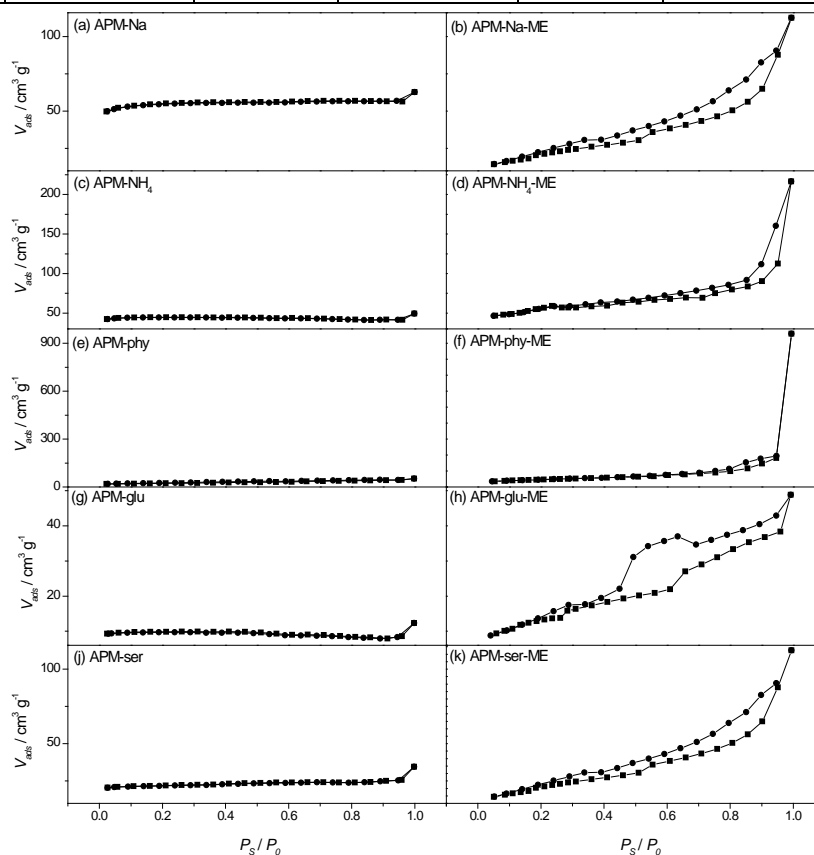
Figure 4.44. Adsorption–desorption BET isotherms of the ammonium phosphomolybdates synthesized in bulk and in miniemulsion with different phosphate precursors. The bulk samples do not present hysteresis instead the miniemulsion samples have a loop similar to the H4 officially defined by IUPAC for the slit-shaped pores.
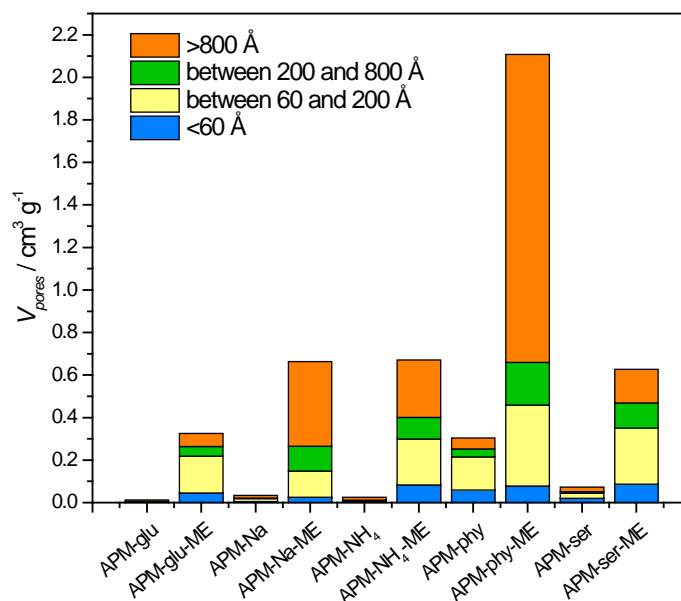
Figure 4.45. Pore size distribution for the ammonium phosphomolybdate samples with different phosphates synthesized in bulk and in miniemulsion.

4.2.4 Catalytic Experiments

Ammonium phosphomolybdates are well known catalysts for oxidation reactions[160, 163] and have been already reported for industrial processes.[175] The oxidation of *cis*-cyclooctene to cyclooctene oxide by *t*-butyl hydroperoxide in chloroform (Figure 4.46) was performed to evaluate the catalytic activity of the ammonium phosphomolybdates synthesized.

Samples synthesized in bulk solution from inorganic phosphates were poorly dispersible in chloroform, compared to the ones synthesized from organic phosphates, much better dispersible. No relevant difference in performances was found in the APM catalysts synthesized in bulk solution: the reactions reached more than 80% of conversion after 10 h, except for APM-Na. The catalysts were recovered, washed in chloroform and reused for a second reaction cycle (Figure 4.46). After the second cycle, the conversion of *cis*-cyclooctene was lower when compared to the first cycle for all catalysts (from 21% less for APM-Na to 8% less for APM-glu).

APM samples prepared by miniemulsion were tested under the same conditions and the conversion of *cis*-cyclooctene reached more than 70% after only 1 h of reaction with all the catalysts (Figure 4.46). The APM-Na-ME has enhanced performance compared to the bulk one (98% of conversion after 10 h instead of 68% of the bulk) as well as APM-phy-ME (100% after 10 h compared to the 84% of the bulk), whereas the APM-NH$_4$-ME is less

active (conversion after 10 h of 89% for the miniemulsion sample instead of 94% for the bulk). APM-glu-ME and APM-ser-ME were considerably active, the *cis*-cyclooctene conversion after only 1 h was respectively of 90% and 98% (compared to the corresponding bulk catalysts with 33% and 28% of conversion after 1 h). It is important to note that, as demonstrated by XRD (Figure 4.41), APM-glu-ME and APM-ser-ME contain also MoO_3, well-known benchmark catalyst for epoxidation;[176] the presence of this side product probably enhances the catalytic performances of the materials. Conversion values for the same epoxidation with commercial MoO_3 are reported, for comparison, in Table 4.20. Possible reasons for the enhanced performances of the APM-ME samples are: (i) their better dispersibility in organic solvents, the particles are solvent-born and, even after several washings, a part of the surfactant employed (PGPR) is still adsorbed on their surface[8]; (ii) the higher porosity, the higher specific surface area (except for APM-NH_4-ME) and the smaller particle size make these samples more suitable for the heterogeneous catalysis, offering more available surface for the adsorption of the substrates. We are aware that the presence of the surfactant might play a negative effect on the catalytic performances by hindering active sites, but, apparently, this is not the case.

As in the previous case, also the APM-ME samples were recovered and used for a 2nd reaction cycle. The performances, contrary to the bulk samples, were comparable (or even better for APM-Na-ME and APM-NH_4-ME) to the 1st cycle. The recyclability, promising both for economic and environmental reasons, is an important difference between the bulk and the miniemulsion samples and, especially the increase of conversion, can be explained with the increase of the active sites at the 2nd cycle as already reported.[160]

The epoxidation of olefins catalyzed by Mo^{VI} can occur following different mechanisms.[177, 178] In aprotic solvents, Mimoun et al.[179] proposed a multiple step process that involves first the coordination of the alkene to the metal of the molybdenum peroxo-complex and then the cycloinsertion of the olefin in the Mo-peroxo bond; Sharpless et al.[180] introduced an alternative mechanism, a concerted reaction via transition state, where the olefin attacks an oxygen atom of a peroxo group. Thus, the Mo catalyzes the reactions mainly coordinating the peroxide and the alkene.
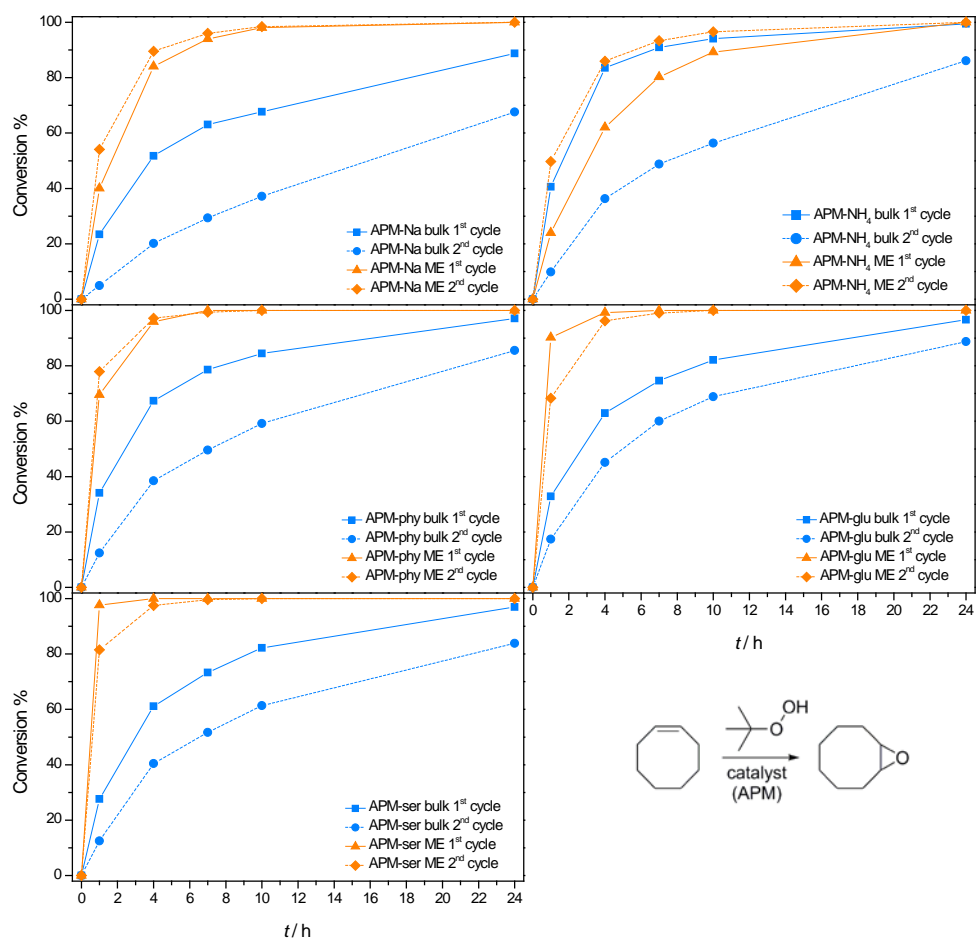
Figure 4.46. Catalytic performance and recyclability of APM produced in bulk and in miniemulsion with different phosphate precursors. Conversions after two cycles with the same catalyst are reported (the solid lines are guiding the eye). Bottom right: epoxidation reaction employed in the catalytic tests.

Table 4.20. *Cis*-cyclooctene oxidation catalyzed by ammonium phosphomolybdates synthesized either in bulk or in miniemulsion: conversion after 1 and 10 h of reaction.

SAMPLE	BULK SOLUTION SYNTHESIS		MINIEMULSION	
	Conversion % 1 h	Conversion % 10 h	Conversion % 1 h	Conversion % 10 h
APM-Na	23	68	40	98
APM-NH$_4$	41	94	24	89
APM-phy	34	84	70	100
APM-glu	33	82	90	100
APM-ser	28	82	98	100
Blank (no catalyst)	2	22	2	25
Commercial MoO$_3$	69	100	—	—

4.2.5 Conclusions

Crystallization of ammonium phosphomolybdates from different phosphate precursors within the water droplets of inverse miniemulsions demonstrated that colloidal confinement controls the crystal growth and determines the particle size. The crystallization in miniemulsion was compared to the one in bulk solution for the same materials to evaluate the effects of the colloidal space confinement. The particles synthesized with both routes have rhombic dodecahedral habit, typical of polyoxometalates with Keggin structure, but the ones produced in bulk have sizes in the range of 1–15 µm, while the one synthesized in miniemulsion are between 40 and 90 nm, three orders of magnitude smaller. Light-transmission measurements were performed during the bulk solution syntheses, assessing that induction times and desupersaturation rates were different when changing the phosphate precursor. This phenomenon is attributed to the different availability of the phosphate ions before and at the moment of the precipitation. NaH_2PO_4 and $NH_4H_2PO_4$ are inorganic salts that dissociate in water to give phosphate anions, while the organophosphates are phosphoesters in which the phosphate is bound to the rest of the organic part through a C–O bond, and is available only after hydrolysis of this bond. Ammonium phosphomolybdate particles synthesized in bulk from inorganic phosphate precursors have bigger sizes than the ones obtained from organic phosphate sources (sizes ≥ 10 µm instead of sizes ≤ 3 µm, respectively) because of the different kinetics of precipitation. The size difference among the samples synthesized in miniemulsion from different phosphate sources is less significant most likely because the different availabilities of the phosphates are less relevant in confinement, where only small amounts of precursors are present. X-ray diffraction (XRD) pointed out that both bulk and miniemulsion samples were crystalline and matching with the pattern of the cubic phase $(NH_4)_3PO_4(MoO_3)_{12}\cdot4H_2O$. Crystallite sizes were calculated by using the Scherrer formula and, comparing them with particles sizes determined by electron microscopy, it can be inferred that bulk particles are composed of several crystallites, whereas the size of the miniemulsion particles is almost comparable with the corresponding crystallite sizes. Furthermore, the ammonium phosphomolybdates synthesized in miniemulsion from D-glucose 6-phosphate sodium salt (APM-glu-ME) and *O*-phospho-DL-serine (APM-ser-ME) contain an amount of MoO_3 (as assessed by XRD), ascribable most likely to the effect of the Laplace pressure in the miniemulsion droplets. The ammonium phosphomolybdates were tested as catalysts for the epoxidation of *cis*-cyclooctene in chloroform and the particles synthesized in miniemulsion were much

more active compared to the samples produced in bulk solution, especially in the case of APM-glu-ME and APM-ser-ME, in which the conversion was more than 90% after only 1 h compared to bulk catalysts with conversion of 30% after the same time. The increase of catalytic activity can be caused by the higher dispersibility of the miniemulsion particles in organic solvent and by their higher porosity and specific surface area, as assessed by the BET determination. The miniemulsion catalysts preserved their performances when employed for a second epoxidation cycle, while the bulk samples lost considerably their catalytic activity. The ammonium phosphomolybdates synthesized in miniemulsion displayed a promising recyclability, which is a further advantage of these materials produced within colloidal confinement.

4.3 Crystallization of Transition Metal Manganites in Miniemulsion–Solvothermal Conditions

In this section, the synergic combination of miniemulsion and solvothermal conditions has been applied to another group of ternary oxides after the ferrites described in Section 4.1, namely the manganites, ternary manganese oxides.

4.3.1 Introduction

The manganites are a class of manganese oxides: the first material named in this way was the perovskite $(Sr, La)MnO_3$.[181] Generally, in perovskite manganites ($MMnO_3$), the manganese has the oxidation state +III or +IV, and, with both of the states being sometimes present at the same time.[182] Perovskite manganites display a remarkable magnetoresistance (i.e., the lowering of electrical resistivity by application of a magnetic field).[126, 183]

The definition of manganites, as in the case of the ferrites, can be extended to all chemical compounds with general formula $M_xMn_yO_z$, where M is another metal, frequently a transition metal. In this section, three different manganites will be described: $ZnMnO_4$, $CuMnO_2$, and $ZnMnO_3$. These three systems were selected because they can be synthesized from easily available precursors and each of them display a different crystal structure, tunable by changing temperature–pressure conditions.

$ZnMn_2O_4$ is a spinel, but, differently from the cubic spinel ferrites, it has a tetragonal structure (space group $I41/amd$) because it presents a tetragonal distortion (Jahn Teller distortion) due to Mn^{III}. The cubic phase (space group $Fd\bar{3}m$) can be achieved at high temperature (i.e., 1323 K), as reported by Åsbrink et al.[184]

$ZnMnO_3$, contrary to $ZnMn_2O_4$, is quite difficult to obtain as a stable phase; typically, it occurs as a mixture of ZnO and $ZnFe_2O_4$, and the hexagonal perovskite structure is reported at high pressure and temperature.[185-188] The exotic $ZnMnO_3$ cubic spinel (space group $Fd\bar{3}m$) was obtained by sol–gel synthesis[187, 188] and subsequent thermal treatment and, recently, through a low temperature hydrothermal route.[189]

$CuMnO_2$ (crednerite[190]) is a delafossite, an oxide with general formula ABO_2, where generally A has the oxidation state +I. The structure of the delafossite is composed by

alternating layers of BO_6 and A cations coordinated.[191] It has a monoclinic crystal structure (space group $C2/m$).

Generally, those manganites are produced through physical methods and solid-state synthesis, involving high temperature thermal treatments.[184, 192] Wet-chemistry routes, such as coprecipitation, sol–gel, reverse micelles and solvothermal conditions, have been recently employed but they also required , in most of the cases, a post-synthesis thermal treatment at high temperature.[193-197] Hydrothermal syntheses can be used to obtain crystalline manganites, but they involve high temperatures (above 200 °C) and long reaction times.[198, 199] Recently, the coprecipitation of oxalates under hydrothermal conditions was reported as a low-temperature route to achieve the three manganites cited above.[189]

The synergic combination of inverse miniemulsion and solvothermal conditions can also be exploited in our case to produce crystalline and phase pure manganites nanoparticles. The confined space of the miniemulsion droplets plays a role in the control of the crystal growth (as already described for the ammonium phosphomolybdate particles) and the combination of Laplace and autogenous pressure can enhance the crystallinity of the products, as shown for the ferrites.[8] In this work, the synergic approach is applied only to the zinc and copper manganites as initial proof-of-concept. The synthesis needs still optimization, but the preliminary results are promising.

4.3.2 Synthesis of Metal Manganites

The synthetic approach designed and optimized for the ferrites (see Section 4.1) has also been implemented for the manganites.

The coprecipitation of the oxalates is reported in literature as an efficient wet-chemistry route for obtaining crystalline manganites under hydrothermal conditions.[189] The coprecipitation of oxalates, however, is not suitable for the synthesis in inverse miniemulsion, as already demonstrated for the ferrites, because the removal of residual oxalic acid precursor from the products is difficult. Thus, also for the manganites, the coprecipitation of the hydroxides was selected.

The inverse miniemulsion was composed of water droplets in cyclohexane, stabilized by the non-ionic surfactant polyglycerol polyricinoleate (PGPR). The inorganic precursors were solubilized in water (disperse phase) and the precipitating agent was a concentrated

aqueous solution of sodium hydroxide. The NaOH solution was added to the miniemulsion, and a second ultrasonication was applied to trigger the penetration of the base in the droplets and promote the precipitation (Figure 4.1).

For the synthesis of both zinc manganites, the precursors were zinc(II) and manganese(II) chloride, with a concentration 0.5 M in the disperse phase. In the case of $ZnMnO_3$, potassium permanganate ($KMnO_4$) was added as oxidizing agent,[200] so that the formation of Mn^{IV} (i.e., the oxidation state required for $ZnMnO_3$) is promoted. The $KMnO_4$ was added before the first emulsification and the reaction started already before the injection of the base. In future experiments, $KMnO_4$ could be added after the NaOH and the second sonication to avoid the oxidation before the precipitation.

For the synthesis of the copper manganite, $Cu(NO_3)_2 \cdot 3H_2O$ and $Mn(OAc)_2 \cdot 4H_2O$ were employed as precursors, as reported in literature.[189] Most probably, the synthesis can also be performed with the corresponding chlorides, to be comparable with the synthesis of the other zinc manganites.

In literature,[189] the reported molar ratio of precipitating agent is Mn : NaOH = 1 : 23, and this was the ratio used for the syntheses described in this section. Such a large amount of base destabilized the miniemulsion system and, at the end of the reaction, phase separation occurred. Many parameters affect the miniemulsion stability and the optimization process requires their variation: the amount of precipitating agent, how it is added, the reaction temperature, and the amount of chemicals.

After the addition of NaOH and the second ultrasonication, the miniemulsion was poured in the Teflon lined solvothermal bomb and placed in an oven at 100 °C. The autogenous pressure was calculated with Antoine's equation, as explained in Section 2.3, and it was estimated to be 3 bar at 100 °C. The miniemulsion was also placed under reflux conditions at 100 °C to compare the results under autogenous pressure and at ambient pressure. The same nomenclature used for the ferrites is here applied to the manganites: the combination miniemulsion–solvothermal conditions is shorten to ME–HP and the miniemulsion at ambient pressure is indicated as ME.

4.3.3 Structural and Morphological Characterization of Metal Manganites

The manganites synthesized with different precursors were characterized by X-ray diffraction (XRD) to evaluate the crystallinity and the crystallite size, and to find out which

crystalline phases are present in the products, in relation to the temperature–pressure parameters.

$ZnMn_2O_4$ was synthesized at 100 °C in miniemulsion both under autogenous pressure and at ambient pressure.
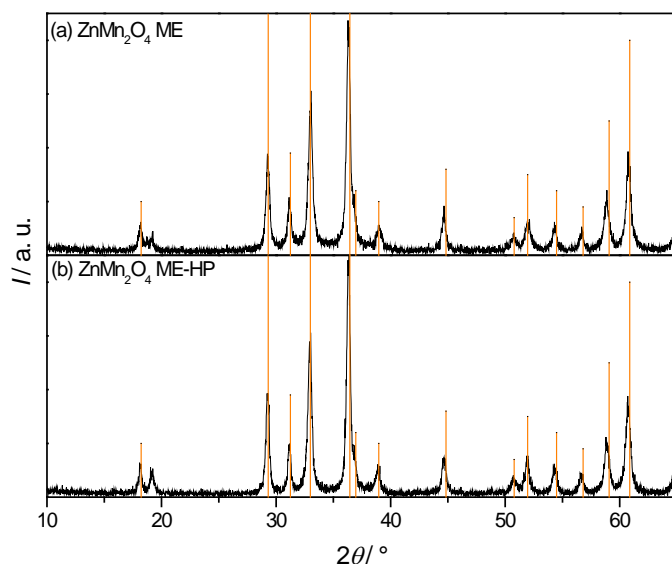
Figure 4.47. X-ray diffraction patterns of zinc manganites $ZnMn_2O_4$ synthesized in (a) miniemulsion at 100 °C and ambient pressure and (b) combination of miniemulsion and solvothermal conditions at 100 °C (3 bar autogenous pressure). The orange vertical lines are the reference pattern of $ZnMn_2O_4$ tetragonal spinel (ICDD card no. 00-024-1133).

The patterns (Figure 4.47) well defined and with sharp reflections match perfectly with the reference pattern of the $ZnMn_2O_4$ tetragonal spinel (ICCD card no. 00-024-1133). The achievement of a crystalline material at low temperature (i.e., 100 °C, compared to the temperatures of solid-state or hydrothermal routes, well above 200 °C) and without post-synthesis thermal treatment should not be underestimated. For instance, $ZnMn_2O_4$ was recently achieved at low temperature (i.e., 180 °C, 80 °C more than our approach) by coprecipitation of oxalates under hydrothermal conditions, but ZnO was also present as a spurious phase.[189]

Small pressure differences, like the one experienced in miniemulsion at ambient pressure, are enough for this system to achieve the crystallinity to achieve the crystallinity; therefore, higher pressure, like the one provided by the solvothermal route, do not have further influence.

The diffraction patterns of the $ZnMnO_3$ produced in miniemulsion indicate that the samples were crystalline but they were composed by a mixture of crystalline phases (Figure

4.48). Cubic (ICDD card no. 00-019-1461) and hexagonal (ICDD card no. 00-028-1468) polymorphs of $ZnMnO_3$ were present in the sample (both reference patterns match with some of the sample reflections). $KMnO_2$ (ICDD card no. 00-018-1035, i.e., product of $KMnO_4$ reduction) and ZnO (ICDD card no. 00-036-1451) were present as spurious phases.
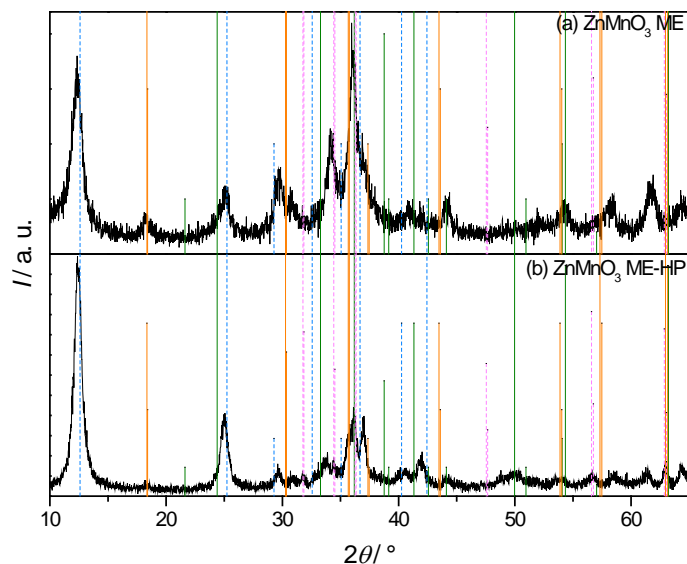
Figure 4.48. X-ray diffraction patterns of zinc manganites $ZnMnO_3$ synthesized in (a) miniemulsion at 100 °C and ambient pressure and (b) combination of miniemulsion and solvothermal conditions at 100 °C (3 bar autogenous pressure). The orange vertical lines are the reference pattern of $ZnMnO_3$ cubic spinel (ICDD card no. 00-019-1461), the green lines of $ZnMnO_3$ hexagonal perovskite (ICDD card no. 00-028-1468), the blue dashed lines of $KMnO_2$ (ICDD card no. 00-018-1035), and the magenta dashed lines of ZnO (ICDD card no. 00-036-1451).

The pure phase synthesis of cubic $ZnMnO_3$ is demanding and, up to now, to the best of our knowledge, only one case of low temperature hydrothermal synthesis has been successful.[189] Probably, reducing the amount of $KMnO_4$ employed and adding it after the base could lower the amount of $KMnO_2$ side product. Apparently, the conditions provided by the miniemulsion droplets, even combined with the solvothermal route, promoted the crystallization, but not the phase selection: a small amount of ZnO was formed in addition to the zinc manganites, most likely because it was kinetically favored. A possible optimization route can be the variation of the precursors amounts and the reaction temperature.

Crystalline crednerite $CuMnO_2$ (ICDD card no. 00-050-0860) was obtained in miniemulsion (Figure 4.49), but a small amount of CuO (ICDD card no. 00-048-1548) was also present in the products. A similar occurrence was also observed for $CuFe_2O_4$ (see Section 4.1.3), which is likely caused by the fast precipitation of CuO at the reaction pH, the same arguments are also applicable to the present system.
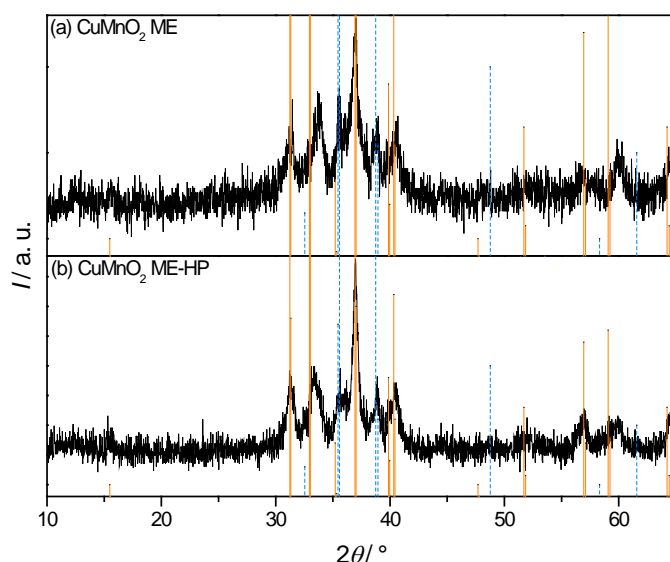
Figure 4.49. X-ray diffractograms of the copper manganite $CuMnO_2$ synthesized in (a) miniemulsion at ambient pressure and (b) miniemulsion under solvothermal conditions (3 bar autogenous pressure). The orange lines are the reference pattern of $CuMnO_2$ crednerite, delafossite monoclinic (ICDD card 00-050-0860). The blue dashed lines are the reference pattern of CuO (ICDD card no. 00-048-1548).

The dimension of the coherent scattering domains (i.e, crystallite size) was calculated for each sample with the Scherrer formula[90] on the most intense reflections (Table 4.21).

The crystallite sizes are bigger for $ZnMn_2O_4$, which is, indeed, the most crystalline sample (Figure 4.47). The sizes of the three manganites, obtained after changing the pressure conditions are not very different, pointing out again that the combination between miniemulsion and solvothermal conditions does not have a significant influence in these concrete systems.

Table 4.21. Crystallite size (L) calculated with the Scherrer formula on the most intense reflection for all the manganites synthesized.

Sample	Reaction conditions	L / nm
$ZnMn_2O_4$	100 °C, ambient P	23
$ZnMn_2O_4$	100 °C, solvothermal	25
$ZnMnO_3$	100 °C, ambient P	11
$ZnMnO_3$	100 °C, solvothermal	8
$CuMnO_2$	100 °C, ambient P	18
$CuMnO_2$	100 °C, solvothermal	20

The morphology of the manganites nanoparticles was investigated by scanning electron microscopy (SEM). The SEM images are reported in Figure 4.50.
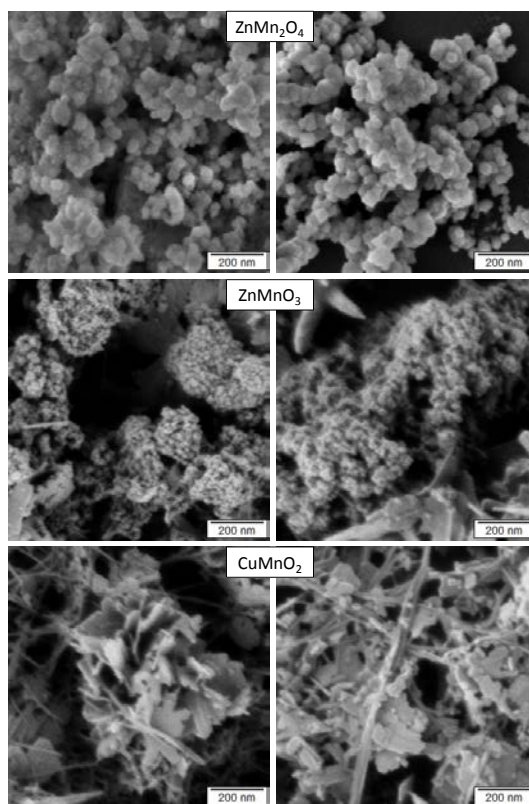
Figure 4.50 SEM images of the manganites synthesized in miniemulsion: on the left side at ambient pressure and on the right side under solvothermal conditions.

In all cases nanoparticles were achieved. In particular, the particles were spherical for both zinc manganites. For the case of the $CuMnO_2$ sample, a mixed morphology is observed: plate-like particles, most likely ascribable to delafossite, are surrounded by other needle-like particles (probably CuO).

4.3.4 Conclusions

The inverse miniemulsion was applied for the crystallization of another class of ternary oxides, the manganites. The synthesis in the confined space of the water droplets promoted the crystallinity at lower temperature than generally reported (i.e., 100 °C against more than 200 °C) and without any post-synthesis thermal treatment. Three different manganites were achieved: pure tetragonal single phase $ZnMn_2O_4$ (without ZnO as spurious phase), $CuMnO_2$ obtained as crystalline crednerite (although with residues of CuO), and $ZnMnO_3$ obtained as a mixture of cubic and the hexagonal phases, both difficult to achieve in mild conditions.

4. Results and Discussion

The confinement controlled the crystal growth and the final particle size. Indeed, all the products were nanoparticles, the zinc manganites with a spherical form and the copper manganite with a plate-like morphology, as evidenced by SEM.

The results shown in this section are an initial proof-of-concept. The synthetic procedure needs optimization to achieve the stability of the miniemulsion systems through the whole process and to promote the phase purity.

In these first experiments, the combination of miniemulsion and solvothermal conditions did not show any significant difference when compared to miniemulsions at ambient pressure. However, as an outlook for future experiments, higher external pressures can be employed to explore the phase selection, especially for $ZnMnO_3$.

5. Conclusions

Crystallization steps are dramatically affected by nanometric confinement. In this work, the synthesis of ferrites, ammonium phosphomolybdates, and manganites within miniemulsion droplets was performed to explore the different aspects of this phenomenon.

Miniemulsion droplets, acting ideally as independent nanoreactors, offered confined spaces where the coprecipitation of metal hydroxides took place, and first-row transition metal ferrites were obtained as spinel. The crystallization was achieved at much lower temperature (i.e., 80 °C) than usually required and without post-synthesis thermal treatment because of the synergetic combination of high autogenous pressures (i.e., 2 bar at 80 °C and 3 bar at 100 °C), provided by the solvothermal route, and the Laplace pressure, typical of the small miniemulsion droplets. Alternatively, iron-rich zinc ferrite was synthesized either in miniemulsion at ambient pressure or in bulk solution (at ambient pressure or under solvothermal conditions). Comparably, the products were not as highly crystalline as the result of the miniemulsion–solvothermal combination, demonstrating the importance of the synergy. The synergetic route yielded crystalline ferrites not only in mild conditions, but also after short reaction times. Indeed, the products were already crystalline after only 3 h of reaction. Iron-rich zinc ferrite was selected as model ferrite material because it is reported as a completely direct spinel in bulk. However, the cationic distribution is highly inverted in the samples produced in miniemulsion, as evidenced by X-ray absorption spectroscopy (XAS). This result also confirms the effect of colloidal confinement on crystallization, although the mechanism of this finding is not yet fully understood. As an outlook, it is suggested that it could be clarified in future with in situ experiments at synchrotron radiation facilities. The synergy between miniemulsion and solvothermal route was also explored at pressure higher than the autogenous and at constant temperature, introducing an external inert gas inside the autoclave reactor. The miniemulsion was colloidally stable at 100 °C and almost 100 bar, outlining its possible employment under severe conditions for materials that require more energy for crystallization. The importance of the synergy was further confirmed by the synthesis of a crystalline and pure phase iron-rich zinc ferrite at room temperature (i.e., 25 °C) and under 80 bar.

5. Conclusions

The effect of nanometric confinement was further studied with ammonium phosphomolybdates produced from different phosphate precursors. The crystal structures obtained in miniemulsion have sizes smaller than 100 nm, while the ones produced in bulk are in the range 1–15 µm, three orders of magnitude bigger. This remarkable difference in size is caused by the crystal growth control: in the small volume of the droplets, only limited amounts of precursors are present, and the material is not exchanged between the droplets, so that the growth can take place only from the initial reduced quantity of precursors. Moreover, the droplets offer a nanometric space constraint to the particle growth. Ammonium phosphomolybdate was obtained crystalline when synthesized both in miniemulsion and in bulk solution. Comparing crystallite sizes calculated with the Scherrer formula and particles sizes determined by electron microscopy, it can be inferred that the bulk particles are composed of several crystallites, whereas the size of the miniemulsion particles is almost comparable with the corresponding crystallite sizes.

High crystallinity and controlled particle size have positive consequences on the functional properties of the materials. Due to their nanometric size, the ferrites synthesized in miniemulsion–solvothermal conditions show superparamagnetic behavior. Furthermore, ferrites and ammonium phosphomolybdates display high specific surface area and porosity. Their high specific surface area combined with their enhanced dispersibility in organic solvent make the particles suitable as catalyst for epoxidation reactions in organic media. The ferrites were active catalysts for the epoxidation of styrene, easily recoverable from the reaction medium by using a magnet, and reusable for several cycles without losing activity. The ammonium phosphomolybdates catalyzed the epoxidation of *cis*-cyclooctene, and the conversion values obtained were remarkably higher compared to the corresponding bulk samples, even after only 1 h of reaction. Furthermore, miniemulsion materials were shown to be recyclable without losing activity, while the corresponding bulk ones yielded much lower conversion values already after the first cycle.

The exploration of the potentialities of inverse miniemulsions for the synthesis of complex inorganic systems was also extended to manganites, a class of materials that was selected because they display many crystalline structures by changing metal precursors and p–T conditions. Zinc and copper manganites are generally difficult to achieve as crystalline materials in mild conditions (i.e., temperature below 200 °C), but in miniemulsion they were already obtained at 100 °C, indicating once more the promotion of crystallinity under colloidal confinement.

In future, this work could be continued by monitoring in situ by EXAFS at synchrotron radiation facilities the crystallization in miniemulsion (at ambient pressure or under solvothermal conditions), which could offer a better understanding on the crystal formation. Moreover, the effect of extremely high pressures, much higher than the 200 bar generally afforded by autoclave reactors, would be also worthy to be investigated.

In summary, this dissertation has demonstrated the remarkable effects of the space confinement provided by miniemulsion on the crystallization of functional materials and on the application of the products as promising catalysts. The miniemulsion is confirmed as a reproducible route to obtain crystalline inorganic nanostructures, and it is shown that it can be applied to a great variety of materials.

6. Experimental Part

6.1 Synergy of Miniemulsion and Solvothermal Conditions for the Crystallization of Transition Metal Ferrites

6.1.1 Materials

Iron(III) chloride hexahydrate (ACS reagent 97%, Sigma Aldrich), iron(II) chloride tetrahydrate (puriss., ≥99.0% (RT), Sigma Aldrich), cobalt(II) chloride hexahydrate (ACS reagent 98%, Sigma Aldrich), copper(II) chloride dihydrate (ACS reagent ≥99.0%, Sigma Aldrich), manganese(II) chloride tetrahydrate (99+% for analysis, Acros Organics), nickel(II) chloride hexahydrate (ReagentPlus, Sigma Aldrich), zinc(II) chloride (98+% anhydrous, Alfa Aesar), and sodium hydroxide (pellets, ACS reagent ≥98%, Sigma Aldrich) were used without further purification. Commercial poly-glycerine polyricinoleate (Grinsted PGPR 90 Kosher, Danisco, offered without charge) was used as received. Cyclohexane (HiPerSolv, Chromanorm, VWR chemicals) and Milli-Q water (Millipore, resistance 18.2 MΩ cm) were used to prepare the solutions and suspensions.

For the preparation of samples for transmission electron microscopy analyses, D-(+)-trehalose dihydrate (Fisher BioReagents), uranyl acetate dihydrate (Riedel de Haën) and 1-ethyl-3-methylimidazolium tetrafluoroborate (ionic liquid EMI-BF4) (Aldrich) were employed.

For the catalytic tests 1,2-dichlorethane (ACS reagent, ≥99.0%, Sigma Aldrich), *tert*-butyl hydroperoxide solution in decane (TBHP, 5.5 mol L^{-1}, Sigma Aldrich) and dichloromethane (HPLC grade, Fisher Scientific) were used as received, styrene (ReagentPlus, containing 4-*tert*butylcatechol as stabilizer, ≥99%, Sigma Aldrich) was purified with liquid chromatography on an aluminum oxide column to remove the stabilizer.

6.1.2 Synthetic Protocol

In a typical synthesis, the inorganic precursors were dissolved in Milli-Q water to prepare a solution with Fe:metal molar ratios of 2:1 or 1:1, as specified later. This aqueous solution

was mixed with the organic phase (1 wt% solution of PGPR in cyclohexane), in a weight ratio of 1:4. Both the aqueous and the organic phase were stirred together to promote a pre-emulsification. The mixture was then ultrasonified by a Branson digital sonifier W-450D (½" tip, 2 min sonication time, 70% amplitude, pulse 1 s, pause 0.1 s). Immediately after the ultrasonication, an excess (i.e., 12 times the moles of Fe) of NaOH 16.6 M aqueous solution was added to the just-prepared stable miniemulsion and this mixture was ultrasonified again with the same parameters described above to trigger the penetration of NaOH inside the droplets and to promote the precipitation of the inorganic precursors within the confined space of the droplets. The miniemulsion was either (i) placed immediately at 80 °C and ambient pressure without stirring in a glass vial or (ii) poured in a Teflon-lined autoclave reactor (45 mL, mod. 4744 Parr Instrument), sealed and placed at 80 °C without stirring for different heating times (3, 6, 12 and 24 h). After the reaction time, the suspension was centrifuged (13 000 rpm, 5 min) to collect the solid product. This product was washed afterwards by centrifuging once with a 1:1 mixture in volume of acetone and ethanol and three times with deionized water. The solid obtained was dried under vacuum at room temperature for 15 h and subsequently ground.

Bulk syntheses (i.e., direct precipitation from an aqueous solution) were performed for the sake of comparison with the materials prepared with our miniemulsion method. A typical bulk procedure started from the aqueous solution of the inorganic salts, keeping the same amount of precursors and NaOH solution of the miniemulsion protocol, but the NaOH was added directly to the salts solution and the precipitation occurred immediately. The mixture was placed at 80 °C without stirring either in the Teflon-lined autoclave reactor for the solvothermal reaction or at ambient pressure in a glass vial, as the miniemulsion synthesis. The same volume of cyclohexane was added to the bulk synthesis to have the same pressure in the reaction vessel. The centrifugation and the washing procedure was the same performed for the samples produced in miniemulsion.

High-pressure syntheses were performed in miniemulsion–solvothermal conditions employing an autoclave equipped with a gas inlet, a manometer, a heating body and a mechanical stirrer, regulated by a digital controller (Compact Micro Reactor with PTFE gasket mod. 5512 and Reactor controller mod. 4848, Parr Instruments). After the addition of the NaOH and the second sonication, the miniemulsion was placed in the Teflon liner of the autoclave, the reactor was sealed and inserted in the heating body. The gas inlet was connected to the gas line and argon was driven inside the reactor, until the desired

pressure was reached. All the valves were closed and the autoclave was detached from the gas line. The heating program started with a rate of $1\,°C\,min^{-1}$ up to the desired temperature, to avoid overheating since Teflon is not a good thermal conductor. The reaction was not stirred to have a comparable situation with the other autoclave under autogenous pressure. After 24 h of reaction, the heating body was turned off and the reactor removed from there to cool down. At room temperature, the outlet valve was opened to purge the remaining pressure. The sample was recovered, washed, centrifuged and dried as reported above.

6.1.3 Catalytic Experiments

The catalytic activity of the ferrites was tested for the oxidation of styrene. The reaction was performed at 70 °C: the catalyst (20 mg, 0.09 mmol), 1,2-dichloroethane (25.4 mmol) and purified styrene (4.3 mmol) were placed in a vial and the addition of the TBHP (13.0 mmol) started the reactions. The closed vial was put in a thermoshaker (HLC, MKR 23) at 600 rpm and 70 °C. Sampling volumes of 100 μL were collected at different times and diluted with 2.4 mL of dichloromethane to quench the reaction. To assure the separation of the catalyst from the reaction solution, a neodymium magnet was used. 80 μL of the dichloromethane solution were withdrawn and poured in a vial with 920 μL of dichloromethane to achieve the concentration range suitable for the following analysis. Decane, present in the TBHP solution, was employed as an internal standard.

The samples were analyzed by a gas chromatograph coupled with a mass spectrometer (GC-MS) to follow the oxidation and to identify the products.

The magnetic catalyst was recovered with a neodymium magnet after the reaction and the powder was washed three times with dichloromethane. The oxidation of the styrene was carried out for three additional cycles using the recovered powder to test the reusability of the catalyst. A blank reaction in the absence of the catalyst was carried out to demonstrate the catalytic activity of ferrite.

6.2 Colloidally Confined Crystallization of Ammonium Phosphomolybdates from Organic and Inorganic Phosphate Sources

6.2.1 Materials

Ammonium molybdate tetrahydrate (ACS reagent ≥99.0% (T), Fluka), sodium phosphate monobasic (bioXtra, ≥99.0% (RT), Sigma Aldrich), ammonium dihydrogen phosphate (for analysis 99+%, Across Organics), phytic acid sodium salt hydrate (from rice, Sigma Aldrich), D-Glucose-6-phosphate sodium salt (≥98%, for biochemistry, Carl Roth), O-phospho-DL-serine (Sigma Aldrich), and nitric acid (puriss. p.a., reag. ISO, ≥65%, Sigma Aldrich) were used without further purification. Commercial polyglycerine polyricinoleate (Grinsted PGPR 90 Kosher, Danisco) was used as received. Cyclohexane (HiPerSolv, Chromanorm, VWR chemicals) and Milli-Q water (Millipore, resistance 18.2 MΩ cm) were used to prepare the solutions and the suspensions.

For the catalytic tests chloroform (Spectronorm, assay 99.2% VWR chemicals), *tert*-butyl hydroperoxide (TBHP) solution in nonane (5.5 M, Sigma Aldrich), chlorobenzene (99.9% for HPLC, Acros Organics) were used as received; *cis*-cyclooctene (95%, Sigma Aldrich, with 100–200 ppm Irganox 1076 FD as antioxidant) was purified by liquid chromatography on an aluminum oxide column to remove the stabilizer.

6.2.2 Bulk Solution Crystallization

In a typical bulk solution synthesis (i.e., direct precipitation from an aqueous solution), ammonium molybdate tetrahydrate and the selected phosphate were dissolved in Milli-Q water to prepare two 0.1 M solutions of equal volume. The two solutions were mixed together in a round bottom flask and placed in an oil bath at 80 °C under magnetic stirring (400 rpm). After 20 min of stirring at 80 °C, nitric acid was added to the system in the same volume of the ammonium molybdate solution (large excess of HNO_3). The acid started the precipitation of the product and the mixture turned yellow. After the selected time (generally 1 h, unless otherwise specified), the reaction was quenched in ice bath and the precipitate recovered by centrifugation (13 000 rpm, 5 min). Afterwards the product was washed three times with deionized water. The solid obtained was dried under vacuum at room temperature for 15 h and subsequently ground.

6.2.3 Miniemulsion Crystallization

In a typical miniemulsion synthesis, ammonium molybdate tetrahydrate and the selected phosphate were dissolved in Milli-Q water, both at a concentration of 0.1 M. This aqueous solution was mixed with the organic phase (1 wt% solution of PGPR in cyclohexane), in a weight ratio of 1:4. The aqueous and the organic phase were stirred together to promote a pre-emulsification. The mixture was then ultrasonified by a Branson digital sonifier W-450D (½" tip, sonication time of 2 min, 70% amplitude, pulse of 1 s, pause of 0.1 s). Immediately after the ultrasonication, an excess (i.e., 12 times with respect to the moles of Mo) of HNO_3 (65 wt%, 14.4 M) was added to the just prepared stable miniemulsion and this mixture was ultrasonified again with the same parameters to trigger the penetration of HNO_3 inside the droplets and to provide the precipitation of the product within that confined space. The miniemulsion was placed immediately at 80 °C under stirring (400 rpm) for 1 h.

After the reaction time, the suspension was centrifuged (13 000 rpm, 5 min) to collect the solid product. This product was washed afterwards once with a 1:1 mixture of acetone and ethanol and three times with deionized water. The solid obtained was dried under vacuum at room temperature for 15 h and subsequently ground.

6.2.4 Light Transmission Measurements

Crystallization kinetics was studied monitoring the desupersaturation curves by turbidity measurements. Light transmission measurements were conducted in the dark with a self-made setup comprised of a He–Ne red laser source (JDSU, model 1145P, 633 nm, 25 mW), a filter (Schott) that reduces the intensity of the transmitted light by a factor of 20, a collimator that align and center the beam and a photodiode detector (photosensitive area = 10×10 mm). The detected current was amplified by a transimpedance amplifier, coupled with a multimeter (Keithley 2700) connected to computer for data acquisition, as in previous works.[201, 202] Typical precipitation experiments were conducted in a glass jacketed reactor at 80 °C controlled with a thermostat (Lauda Ecoline Gold RE415) under magnetic stirring. The laser light passed through the reactor containing the initially transparent precursor solution. After the stabilization of the transmitted light signal, the precipitating agent (nitric acid) was added, which established the time zero for the experiments. The values of intensity of transmitted light were normalized to the initial value.

6.2.5 Catalytic Experiments

The catalytic activity of the ammonium phosphomolybdates was tested for the oxidation of *cis*-cyclooctene with TBHP at 80 °C. The catalyst (11 mg), chloroform (9.7 mmol), chlorobenzene (4.6 mmol), and purified *cis*-cyclooctene (4.6 mmol) were placed in a vial and the reaction was started by addition of TBHP (9.2 mmol). The closed vial was placed in a thermoshaker (HLC, MKR 23) at 80 °C under 500 rpm. Sampling volumes of 50 μL were collected at different times and diluted with 2.45 mL of chloroform to quench the reaction. To assure the separation of the catalyst from the reaction solution, the catalyst was let to sediment for 2 min before the withdrawn. 50 μL of the chloroform solution were withdrawn and poured in a vial with 950 μL of dichloromethane to achieve the concentration range suitable for the following analysis. Chlorobenzene was employed as an internal standard. The samples were analyzed by a gas chromatograph coupled with a mass spectrometer to follow the oxidation and to identify the products. The catalyst was recovered after the reaction and the powder was washed three times with chloroform. The oxidation of the *cis*-cyclooctene was carried out for one additional cycle using the recovered powder to test the reusability of the catalyst. A blank reaction in the absence of the catalyst was carried out to demonstrate the catalytic activity of the ammonium phosphomolybdates.

6.3 Crystallization of Transition Metal Manganites in Miniemulsion–Solvothermal Conditions

6.3.1 Materials

Manganese(II) chloride tetrahydrate (99+% for analysis, Acros Organics), zinc(II) chloride (98+% anhydrous, Alfa Aesar), potassium permanganate (99+%, ACS reagent, Sigma Aldrich), manganese(II) acetate tetrahydrate (purum p. a., Sigma Aldrich), copper(II) nitrate trihydrate (puriss. p. a. 99–104%, Sigma Aldrich), and sodium hydroxide (pellets, ACS reagent ≥98%, Sigma Aldrich) were used without further purification. Commercial poly-glycerine polyricinoleate (Grinsted PGPR 90 Kosher, Danisco, offered without charge) was used as received. Cyclohexane (HiPerSolv, Chromanorm, VWR chemicals) and Milli-Q water (Millipore, resistance 18.2 MΩ cm) were used to prepare solutions and suspensions.

6.3.2 Synthetic Protocol

In a typical synthesis, the inorganic precursors were dissolved in Milli-Q water to prepare a solution with Mn:metal molar ratio of 1:1. This aqueous solution was mixed with the organic phase (1 wt% solution of PGPR in cyclohexane), in a weight ratio of 1:4. Both the aqueous and the organic phase were stirred together to promote a pre-emulsification. The mixture was then ultrasonified by a Branson digital sonifier W-450D (½" tip, 2 min sonication time, 70% amplitude, pulse 1 s, pause 0.1 s). Immediately after the ultrasonication, an excess (i.e., 23 times the moles of Mn) of NaOH 16.6 M aqueous solution was added to the just prepared stable miniemulsion and this mixture was ultrasonified again with the same parameters described above to trigger the penetration of NaOH inside the droplets and to promote the precipitation of the inorganic precursors within the confined space of the droplets. The miniemulsion was either (i) placed immediately at 100 °C under reflux or (ii) poured in a Teflon-lined autoclave reactor (45 mL, mod. 4744 Parr Instrument), sealed and placed at 100 °C without stirring for 24 h. After the reaction time, the suspension was centrifuged (13 000 rpm, 5 min) to collect the solid product. This product was washed afterwards by centrifuging once with a 1:1 mixture in volume of acetone and ethanol and three times with deionized water. The solid obtained was dried under vacuum at room temperature for 15 h and subsequently ground.

6.4 Characterization Techniques

6.4.1 X-Ray Diffraction (XRD)

X-ray diffraction of the washed and vacuum dried powders was conducted with a Philips PW 1820 diffractometer. The diffractometer source was a copper tube with monochromatic K_α radiation ($\lambda_{K_\alpha} = 1.5418$ Å). The generator was operated at 40 kV and 30 mA. The diffractometer was used in reflection mode with a Bragg-Brentano geometry (theta-2theta): the detector moved in steps $\Delta\theta = 0.02°$ and the intensity was measured for 5 s per step.

Dry powders of the synthesized ferrites, ammonium phosphomolybdates, and manganites were carefully ground to avoid isoorientation of the crystallites. The ground powders were placed in an aluminum sample holder for the measurement.

Coherently scattering domain dimensions (crystallite sizes) were calculated for each sample by using the Scherrer formula[88] on the most intense reflection of the diffractograms. The most intense reflections were the (311) for the ferrites, the (222) for the ammonium phosphomolybdates, the (211) for the $ZnMn_2O_4$, and the (111) for the $CuMnO_2$. In the case of $ZnMnO_3$, the most intense reflection can be attributed to both zinc manganite phases present in the sample, since they are almost overlapping. Thus, the reflection can be the (311) of the cubic phase or the (110) of the hexagonal phase.

6.4.2 Scanning Electron Microscopy (SEM)

Scanning electron microscopy was performed with a Leo Gemini Zeiss 1530 microscope. The extractor voltage employed was 700 V for the ammonium phosphomolybdate samples, 3 kV for $ZnMn_2O_4$, and 500 V for $ZnMnO_3$ and $CuMnO_2$.

Samples for SEM characterization were prepared either depositing dry powder on carbon tape for the bulk samples of ammonium phosphomolybdate or by drop-casting diluted dispersions on silicon wafers for the miniemulsion samples (of APM and manganites).

Average particle sizes were calculated for APM samples measuring the dimension of a statistical number of particles from the SEM micrographs, by using the software Fiji ImageJ.

6.4.3 Transmission Electron Microscopy (TEM)

A FEI Tecnai F20 transmission electron microscope operated at an acceleration voltage of 200 kV was used for the TEM measurements. The micrographs were recorded on a 2k CCD camera (Gatan Ultrascan1000).

The ferrite samples were prepared by dropping a dispersion of the materials on a carbon coated grid and by letting the liquid phase to evaporate. Artifacts were avoided by embedding the particles in a matrix of trehalose. Negative staining with uranyl acetate was applied to increase the contrast. Alternatively, by using another preparation method, the samples were embedded in a matrix of the ionic liquid 1-ethyl-3-methylimidazolium tetrafluoroborate, which remains liquid due to the very low vapor pressure under the high vacuum of the electron microscope chamber. Further details of the preparation method are reported elsewhere.[203]

6. Experimental Part

The dispersions of the ammonium phosphomolybdate samples were dropped on a carbon-coated grid, and the liquid phase were evaporated.

Average particle sizes were calculated for both group of materials measuring the dimensions of a statistical number of particles from TEM images by using Fiji-ImageJ software.

6.4.4 Focused Ion Beam (FIB)

Focused Ion Beam (FIB) is a dual beam machine that allows the site-specific milling of the sample by ion beam and simultaneously the imaging by electron beam.

A FEI Nova600Nanolab FIB was employed to cut a lamella from one of the ammonium phosphomolybdate bulk samples (i.e., APM-glu).

Sample lamellae were milled to extensions of about 10×6 μm and thicknesses of about 50–100 nm to be suitable for TEM measurements. Preparation sites were located by secondary electron microscopy (SEM) integrated in the FIB, sputtered with an additional Pt layer as protection (the FIB induced a Pt layer deposition about 1 μm of thickness at 30 kV and 0.5 nA) and milled by Ga-ion sputtering with a beam resolution of 10 nm. The milling process occurred stepwise: two trenches were milled at 30 kV and 3 nA on both sites of the Pt deposition, afterwards both sides were milled at 30 kV and 1 nA to achieve a flat surface. The lamella had a thickness around 1 μm. A further thinning and polishing process at different currents (0.3 nA and 0.1 nA) yielded a lamella with a thickness around 50–100nm, which is necessary for its measurement by TEM. During the lift-out process (Omniprobe nanomanipulator), the sample was transferred to a TEM grid and attached to it with a small Pt spot.

6.4.5 Gas Chromatography (GC)

The gas chromatograph Shimadzu, GCMS–QP2010 Ultra was employed to monitor the oxidation reactions catalyzed by the ferrites and ammonium phosphomolybdate samples.

This device was equipped of an autosampler: the vials containing the solutions to be analyzed were placed in a carousel and a mechanical arm was selecting them according to a computer batch procedure, bringing them to a syringe for the automatic sampling. The solution was injected in the inlet to be vaporized before entering in the column. The

column (Phenomenex, Zebron 5-ms, unipolar) was located inside a temperature controlled oven. The oven was usually kept at 50 °C and during the measurement it was heated up till 310 °C, the injection temperature.

The gas chromatograph detector was a mass spectrometer: the chemical species involved in the reactions were identified by comparison of their mass spectra with the ones present in the data bank. The quantitative determination of the species concentration was performed, employing an internal standard (i.e., decane and chlorobenzene) to correlate the areas of the chromatographic peaks with the concentrations of the relative molecules. The conversion of the starting reagent during the reaction was calculated from the concentrations of the analytes.

6.4.6   Physisorption of Nitrogen at Cryogenic Temperature: Specific Surface Area and Porosity Evaluation

Specific surface area and porosity were determined by measuring the nitrogen physisorption at cryogenic temperature with an Autosorb MP1 instrument (Quantachrome). The specific surface area was calculated according to the Brunauer–Emmett–Teller (BET) theory[95] in the range of P_s/P_0 0–1.0. Before the measurements, the products were degassed either at 200 °C (for the ferrites) or at 150 °C (for the ammonium phosphomolybdates) for 24 h under vacuum to ensure the complete removal of any previously adsorbed material.

6.4.7   Inductive Coupled Plasma–Mass Spectrometry (ICP–MS)

Inductively coupled plasma–mass spectrometry (ICP–MS, Agilent 7900) was conducted to estimate the molar ratio between the iron and the other metal present in the ferrites and between molybdenum and phosphorus present in the ammonium phosphomolybdates. The solid samples were digested in aqua regia (HCl:HNO$_3$ = 3:1 in volume) at 80 °C for 5 h before the analysis.

6.4.8   Elemental Analysis

Elemental analysis was carried out in a CE Instruments EA1110 CHNS spectrometer to quantify the amount of carbon present in the ammonium phosphomolybdate samples and calculate the molar ratio between molybdenum and nitrogen.

6.4.9 Interfacial Tension Measurements

The interfacial tension between the continuous and the disperse phase of a typical miniemulsion was determined using either the pendant drop method with an optical goniometer (OCA35, Dataphysics, Germany) or the spinning drop tensiometer (Dataphysics SVT 20N).

The optical goniometer was employed for the ferrite miniemulsion system and the measurements were performed at room temperature in the following way. The liquid media (liquid of lower density, in our case, cyclohexane–PGPR 0.77 g cm^{-2})) was deposited in a polystyrene cuvette. A drop of the higher density liquid (in our case, water–salts 1.15 g cm^{-2}) was immersed in the cuvette, evaluating the interfacial tension through a drop shape analysis software. Averaged values from data were recorded.

The spinning drop tensiometer was used to measure the interfacial tension at room temperature for the ferrite miniemulsion and at 80 °C (i.e., reaction temperature) for the ammonium phosphomolybdate one. The device is equipped with a thermostatic bath to control the temperature during the measurement.

6.4.10 Magnetization Measurement

Magnetic measurements were performed by a superconductive quantum interference device (SQUID) magnetometer (Quantum Design MPMS II). Gelatin capsules were filled with the weighed samples and mounted in a low magnetic moment sample holder.

The measurements were carried out by Prof. Gerhard Jakob (Institute of Physics, Johannes Gutenberg Universität Mainz).

6.4.11 X-Ray Absorption Spectroscopy (XAS)

Fe (7112 eV) and Zn (9659 eV) K-edge spectra were collected at the bending magnet of the XAFS beamline at the Elettra synchrotron facility (Trieste, Italy), under standard ring conditions (2.0 GeV, 300 mA). For energy selection, a Si (111) double-crystal monochromator was used. Spectra were collected in a detuned configuration of the monochromator. Data collection was carried in transmission mode using an ionization chamber placed downstream with respect to the sample. Internal energy calibration was accomplished by simultaneous measurement of the absorption of a Fe or Zn foil placed

between two ionization chambers located after the sample. Each sample was prepared as a pellet, using cellulose as a dispersant medium.

Data reduction and analysis were performed using the Demeter package;[204] in particular, background removal was performed by the Autobk routine of the Athena software, which was also used for data alignment and calibration. The extracted EXAFS functions were fitted exploiting the software Artemis. Passive electron reduction factors (S_{02}) were obtained from the fit to bulk metallic reference (0.8 for Fe and 0.75 for Zn) and then kept constant in the fits for all the solid solutions.

6.4.12 Thermogravimetric analysis (TGA)

Thermogravimetric analysis (TGA) was carried out with a Mettler Toledo ThermoSTAR TGA/SDTA 851 thermobalance under a nitrogen atmosphere (from 50 to 700 °C with a heating rate of 10 °C min^{-1}).

6.4.13 Fourier transform infrared spectroscopy (FTIR)

Fourier transform infrared spectroscopy (FTIR) was performed with a Spectrum BX spectrometer from PerkinElmer and the absorption of KBr pellets of the samples was measured between 4000 and 400 cm^{-1}.

7. References

1.	Cölfen, H.; Antonietti, M., *Mesocrystals and Nonclassical Crystallization*. Wiley: Chichester, 2008.

2.	Kittel, C., *Introduction to Solid State Physics*. Wiley: USA, 2004.

3.	McNaught, A. D.; Wilkinson, A., *IUPAC. Compendium of Chemical Terminology (Gold Book)*. 2nd ed.; Blackwell Scientific Publications: Oxford, 2014.

4.	Muñoz-Espí, R.; Mastai, Y.; Gross, S.; Landfester, K., Colloidal systems for crystallization processes from liquid phase. *CrystEngComm* **2013,** 15, (12), 2175-2192.

5.	Muñoz-Espí, R.; Weiss, C. K.; Landfester, K., Inorganic nanoparticles prepared in miniemulsion. *Curr. Opin. Colloid Interface Sci.* **2012,** 17, (4), 212-224.

6.	Landfester, K., The Generation of Nanoparticles in Miniemulsions. *Adv. Mater.* **2001,** 13, (10), 765-768.

7.	Landfester, K., Miniemulsions for Nanoparticle Synthesis. *Top. Curr. Chem.* **2003,** 227, 75-123.

8.	Antonello, A.; Jakob, G.; Dolcet, P.; Momper, R.; Kokkinopoulou, M.; Landfester, K.; Muñoz-Espí, R.; Gross, S., Synergy of Miniemulsion and Solvothermal Conditions for the Low-Temperature Crystallization of Magnetic Nanostructured Transition-Metal Ferrites. *Chem. Mater.* **2017,** 29, (3), 985-997.

9.	Singh, I.; Landfester, K.; Chandra, A.; Munoz-Espi, R., A new approach for crystallization of copper(II) oxide hollow nanostructures with superior catalytic and magnetic response. *Nanoscale* **2015,** 7, (45), 19250-19258.

10.	Dolcet, P.; Casarin, M.; Maccato, C.; Bovo, L.; Ischia, G.; Gialanella, S.; Mancin, F.; Tondello, E.; Gross, S., Miniemulsions as chemical nanoreactors for the room temperature synthesis of inorganic crystalline nanostructures: ZnO colloids. *J. Mater. Chem.* **2012,** 22, (4), 1620-1620.

11.	Dolcet, P.; Mambrini, A.; Pedroni, M.; Speghini, A.; Gialanella, S.; Casarin, M.; Gross, S., Room temperature crystallization of highly luminescent lanthanide-doped CaF_2 in nanosized droplets: first example of the synthesis of metal halogenide in miniemulsion with effective doping and size control. *RSC Adv.* **2015,** 5, (21), 16302-16310.

12.	Mullin, J. W., *Crystallization*. Elsevier Science: 2001.

13.	Ostwald, W., Studien über die Bildung und Umwandlung fester Körper. *Z. Phys. Chem.* **1897,** 22, 289-330.

14.	Nývlt, J., The Ostwald Rule of Stages. *Cryst. Res. Technol.* **1995,** 30, (4), 443-449.

15.	Chung, S.-Y.; Kim, Y.-M.; Kim, J.-G.; Kim, Y.-J., Multiphase transformation and Ostwald's rule of stages during crystallization of a metal phosphate. *Nat. Phys.* **2009,** 5, (1), 68-73.

16.	Wulff, G., Zur Frage der Geschwindigkeit des Wachstums und der Auflösung von Krystallflächen. *Z. Kristallogr.* **1901,** 34, 449-530.

17.	Volmer, M., *Kinetik der Phasenbildung*. Theodor Steinkopff: Dresden und Leipzig, 1939; Vol. IV.

18.	Kossel, W., Zur Theorie des Kristallwachstums. *Nachrichten von der Gesellschaft der Wissenschaften zu Gottingen. Mathematisch-physikalische Klasse* **1927**, 135-143.

19.	Kossel, W., Zur Energetik von Oberflächenvorgängen. *Z. Phys. Chem.* **1934,** 21, 457-480.

20.	Stranski, I. N., Zur Theorie des Kristallwachstums. *Z. Phys. Chem.* **1928,** 136, 259-278.

21.   Woodruff, D. P., How does your crystal grow? A commentary on Burton, Cabrera and Frank (1951) 'The growth of crystals and the equilibrium structure of their surfaces'. *Philos. Trans. R. Soc. A* **2015,** 373, (2039).

22.   Burton, W. K.; Cabrera, N.; Frank, F. C., Role of dislocations in crystal growth. *Nature* **1949,** 163, 398-399.

23.   Burton, W. K.; Cabrera, N.; Frank, F. C., The Growth of Crystals and the Equilibrium Structure of their Surfaces. *Philos. Trans. R. Soc. A* **1951,** 243, (866), 299-358.

24.   Ostwald, W., *Lehrbuch der allgemeinen Chemie*. Wilhelm Engelmann: Leipzig, 1896; Vol. 2.

25.   Liesegang, R. E., Über die Reifung von Silberhaloidemulsionen. *Z. Phys. Chem.* **1911,** 75, 374-377.

26.   Kolthoff, I. M.; Sandell, F. B.; Meehan, E. J.; Bruckenstein, S., *Quantitative chemical analysis*. The Macmillan Co,: New York, 1969.

27.   Cushing, B. L.; Kolesnichenko, V. L.; O'Connor, C. J., Recent Advances in the Liquid-Phase Syntheses of Inorganic Nanoparticles. *Chem. Rev.* **2004,** 104, (9), 3893-3946.

28.   Kolthoff, I. M., Theory of Coprecipitation. The Formation and Properties of Crystalline Precipitates. *J. Phys. Chem.* **1931,** 36, (3), 860-881.

29.   Lu, A.-H.; Salabas, E. L.; Schüth, F., Magnetic Nanoparticles: Synthesis, Protection, Functionalization, and Application. *Angew. Chem., Int. Ed.* **2007,** 46, (8), 1222-1244.

30.   Diodati, S.; Nodari, L.; Natile, M. M.; Caneschi, A.; de Julián Fernández, C.; Hoffmann, C.; Kaskel, S.; Lieb, A.; Di Noto, V.; Mascotto, S.; Saini, R.; Gross, S., Coprecipitation of Oxalates: An Easy and Reproducible Wet-Chemistry Synthesis Route for Transition-Metal Ferrites. *Eur. J. Inorg. Chem.* **2014,** 2014, (5), 875-887.

31.   Diodati, S.; Pandolfo, L.; Caneschi, A.; Gialanella, S.; Gross, S., Green and low temperature synthesis of nanocrystalline transition metal ferrites by simple wet chemistry routes. *Nano Res.* **2014,** 7, (7), 1027-1042.

32.   Zhao, D.; Wu, X.; Guan, H.; Han, E., Study on supercritical hydrothermal synthesis of $CoFe_2O_4$ nanoparticles. *J. Supercrit. Fluids* **2007,** 42, (2), 226-233.

33.   Kołodziejczyk, K.; Tarnacka, M.; Kamińska, E.; Dulski, M.; Kamiński, K.; Paluch, M., Crystallization Kinetics under Confinement. Manipulation of the Crystalline Form of Salol by Varying Pore Diameter. *Cryst. Growth Des.* **2016,** 16, (3), 1218-1227.

34.   Jiang, Q.; Ward, M. D., Crystallization under nanoscale confinement. *Chem. Soc. Rev.* **2014,** 43, (7), 2066-2079.

35.   Gong, X.; Wang, Y.-W.; Ihli, J.; Kim, Y.-Y.; Li, S.; Walshaw, R.; Chen, L.; Meldrum, F. C., The Crystal Hotel: A Microfluidic Approach to Biomimetic Crystallization. *Adv. Mater.* **2015,** 27, (45), 7395-7400.

36.   Pileni, M. P., Reverse micelles as microreactors. *J. Phys. Chem.* **1993,** 97, (27), 6961-6973.

37.   Nicholson, C. E.; Chen, C.; Mendis, B.; Cooper, S. J., Stable Polymorphs Crystallized Directly under Thermodynamic Control in Three-Dimensional Nanoconfinement: A Generic Methodology. *Cryst. Growth Des.* **2011,** 11, (2), 363-366.

38.   Christenson, H., K. , Confinement effects on freezing and melting. *J. Phys.: Condens. Matter* **2001,** 13, (11), R95.

39.   Stephens, C. J.; Ladden, S. F.; Meldrum, F. C.; Christenson, H. K., Amorphous Calcium Carbonate is Stabilized in Confinement. *Adv. Funct. Mater.* **2010,** 20, (13), 2108-2115.

40.   Wang, Y.-W.; Christenson, H. K.; Meldrum, F. C., Confinement Leads to Control over Calcium Sulfate Polymorph. *Adv. Funct. Mater.* **2013,** 23, (45), 5615-5623.

41.   Wang, Y.-W.; Christenson, H. K.; Meldrum, F. C., Confinement Increases the Lifetimes of Hydroxyapatite Precursors. *Chem. Mater.* **2014,** 26, (20), 5830-5838.

7. References

42.   Stephens, C. J.; Kim, Y.-Y.; Evans, S. D.; Meldrum, F. C.; Christenson, H. K., Early Stages of Crystallization of Calcium Carbonate Revealed in Picoliter Droplets. *J. Am. Chem. Soc.* **2011,** 133, (14), 5210-5213.

43.   Cantaert, B.; Beniash, E.; Meldrum, F. C., Nanoscale Confinement Controls the Crystallization of Calcium Phosphate: Relevance to Bone Formation. *Chem. Eur. J.* **2013,** 19, (44), 14918-14924.

44.   Anduix-Canto, C.; Kim, Y.-Y.; Wang, Y.-W.; Kulak, A.; Meldrum, F. C.; Christenson, H. K., Effect of Nanoscale Confinement on the Crystallization of Potassium Ferrocyanide. *Cryst. Growth Des.* **2016,** 16, (9), 5403-5411.

45.   Mollet, H.; Grubenmann, A., *Formulation Technology: Emulsions, Suspensions, Solid Forms*. 1st ed.; Wiley-VCH: Weinheim, 2001.

46.   Cosgrove, T., *Colloid Science: Principles, Methods and Applications*. John Wiley & Sons: 2010.

47.   Petit, C.; Pileni, M. P., Synthesis of cadmium sulfide in situ in reverse micelles and in hydrocarbon gels. *J. Phys. Chem.* **1988,** 92, (8), 2282-2286.

48.   Cooper, S.; Cook, O.; Loines, N., Crystallization in Microemulsions: A Generic Route to Thermodynamic Control and the Estimation of Critical Nucleus Size. In *Crystallization - Science and Technology*, Andreeta, M. R. B., Ed. InTech: 2012; p 578.

49.   El-Aasser, M. S.; Sudol, D. E., Miniemulsion: Overview of Research and Applications. *JCT Res.* **2004,** 1, (1), 20-31.

50.   Pashley, R. M.; Karaman, M. E., *Applied Colloid and Surface Chemistry*. John Wiley & Sons Ltd: West Sussex, England, 2004.

51.   Tanford, C., *The Hydrophobic Effect: Formation of Micelles and Biological Membranes*. 2nd ed.; Wiley: 1980; p 233.

52.   Griffin, W. C., Classification of surface-active agents by "HLB". *J Cosmet Sci* **1949,** 1, (5), 311-326.

53.   Davies, J. T. In *A quantitative kinetic theory of emulsion type. I. Physical chemistry of the emulsifying agent*, 2nd International Congress Surface Activity, Butterworths, London, 1957; Butterworths, London, 1957; pp 426-438.

54.   Landfester, K., Recent developments in Miniemulsions - Formation and Stability Mechanisms. *Macromol. Symp.* **2000,** 150, 171-178.

55.   Higuchi, W. I.; Misra, J., Physical degradation of emulsions via the molecular diffusion route and the possible prevention thereof. *J. Pharm. Sci.* **1962,** 51, (5), 459-466.

56.   Webster, A. J.; Cates, M. E., Stabilization of Emulsions by Trapped Species. *Langmuir* **1998,** 14, (8), 2068-2079.

57.   Webster, A. J.; Cates, M. E., Osmotic Stabilization of Concentrated Emulsions and Foams. *Langmuir* **2001,** 17, (3), 595-608.

58.   Landfester, K.; Bechthold, N.; Tiarks, F.; Antonietti, M., Formulation and stability mechanisms of polymerizable miniemulsions. *Macromolecules* **1999,** 32, (16), 5222-5228.

59.   Pileni, M.-P., Water in oil colloidal droplets used as microreactors. *Adv. Colloid Interface Sci.* **1993,** 46, 139-163.

60.   Diodati, S.; Dolcet, P.; Casarin, M.; Gross, S., Pursuing the Crystallization of Mono- and Polymetallic Nanosized Crystalline Inorganic Compounds by Low-Temperature Wet-Chemistry and Colloidal Routes. *Chem. Rev.* **2015,** 115, (20), 11449-11502.

61.   Sanchez-Dominguez, M.; Pemartin, K.; Boutonnet, M., Preparation of inorganic nanoparticles in oil-in-water microemulsions: A soft and versatile approach. *Curr. Opin. Colloid Interface Sci.* **2012,** 17, (5), 297-305.

62.   Sanchez-Dominguez, M.; Boutonnet, M.; Solans, C., A novel approach to metal and metal oxide nanoparticle synthesis: the oil-in-water microemulsion reaction method. *J. Nanopart. Res.* **2009,** 11, (7), 1823.

63.   Pemartin, K.; Solans, C.; Alvarez-Quintana, J.; Sanchez-Dominguez, M., Synthesis of Mn–Zn ferrite nanoparticles by the oil-in-water microemulsion reaction method. *Colloids Surf. A* **2014,** 451, 161-171.

64.   Cooper, S. J.; Nicholson, C. E.; Liu, J., A simple classical model for predicting onset crystallization temperatures on curved substrates and its implications for phase transitions in confined volumes. *J. Chem. Phys.* **2008,** 129, (12), 124715.

65.   Chen, C.; Cook, O.; Nicholson, C. E.; Cooper, S. J., Leapfrogging Ostwald's Rule of Stages: Crystallization of Stable γ-Glycine Directly from Microemulsions. *Cryst. Growth Des.* **2011,** 11, (6), 2228-2237.

66.   Nicholson, C. E.; Cooper, S. J., Crystallization of Mefenamic Acid from Dimethylformamide Microemulsions: Obtaining Thermodynamic Control through 3D Nanoconfinement. *Crystals* **2011,** 1, (3), 195.

67.   Boutonnet, M.; Kizling, J.; Stenius, P.; Maire, G., The preparation of monodisperse colloidal metal particles from microemulsions. *Colloids Surf.* **1982,** 5, (3), 209-225.

68.   Pileni, M.-P., The role of soft colloidal templates in controlling the size and shape of inorganic nanocrystals. *Nat. Mater.* **2003,** 2, (3), 145-150.

69.   López-Quintela, M. A., Synthesis of nanomaterials in microemulsions: formation mechanisms and growth control. *Curr. Opin. Colloid Interface Sci.* **2003,** 8, (2), 137-144.

70.   Moran, P. D.; Bartlett, J. R.; Bowmaker, G. A.; Woolfrey, J. L.; Cooney, R. P., Formation of TiO_2 Sols, Gels and Nanopowders from Hydrolysis of $Ti(O^iPr)_4$ in AOT Reverse Micelles. *J. Sol-Gel Sci. Technol.* **1999,** 15, (3), 251-262.

71.   Aubery, C.; Solans, C.; Sanchez-Dominguez, M., Tuning High Aqueous Phase Uptake in Nonionic Water-in-Oil Microemulsions for the Synthesis of Mn–Zn Ferrite Nanoparticles: Phase Behavior, Characterization, and Nanoparticle Synthesis. *Langmuir* **2011,** 27, (23), 14005-14013.

72.   Aubery, C.; Solans, C.; Prevost, S.; Gradzielski, M.; Sanchez-Dominguez, M., Microemulsions as Reaction Media for the Synthesis of Mixed Oxide Nanoparticles: Relationships between Microemulsion Structure, Reactivity, and Nanoparticle Characteristics. *Langmuir* **2013,** 29, (6), 1779-1789.

73.   Montenegro, R.; Antonietti, M.; Mastai, Y.; Landfester, K., Crystallization in Miniemulsion Droplets. *J. Phys. Chem. B* **2003,** 107, (21), 5088-5094.

74.   Willert, M.; Rothe, R.; Landfester, K.; Antonietti, M., Synthesis of Inorganic and Metallic Nanoparticles by Miniemulsification of Molten Salts and Metals. *Chem. Mater.* **2001,** 13, (12), 4681-4685.

75.   Rossmanith, R.; Weiss, C. K.; Geserick, J.; Hüsing, N.; Hörmann, U.; Kaiser, U.; Landfester, K., Porous Anatase Nanoparticles with High Specific Surface Area Prepared by Miniemulsion Technique. *Chem. Mater.* **2008,** 20, (18), 5768-5780.

76.   Nabih, N.; Schiller, R.; Lieberwirth, I.; Kockrick, E.; Frind, R.; Kaskel, S.; Weiss, C. K.; Landfester, K., Mesoporous CeO_2 nanoparticles synthesized by an inverse miniemulsion technique and their catalytic properties in methane oxidation. *Nanotechnology* **2011,** 22, (13), 135606.

77.   Dolcet, P.; Maurizio, C.; Casarin, M.; Pandolfo, L.; Gialanella, S.; Badocco, D.; Pastore, P.; Speghini, A.; Gross, S., An Effective Two-Emulsion Approach to the Synthesis of Doped ZnS Crystalline Nanostructures. *Eur. J. Inorg. Chem.* **2015,** 2015, (4), 706-714.

78.   Hajir, M.; Dolcet, P.; Fischer, V.; Holzinger, J.; Landfester, K.; Muñoz-Espí, R., Sol–gel processes at the droplet interface: hydrous zirconia and hafnia nanocapsules by interfacial inorganic polycondensation. *J. Mater. Chem.* **2012,** 22, (12), 5622-5628.

79.   Varol, H. S.; Álvarez-Bermúdez, O.; Dolcet, P.; Kuerbanjiang, B.; Gross, S.; Landfester, K.; Muñoz-Espí, R., Crystallization at Nanodroplet Interfaces in Emulsion Systems: A Soft-Template Strategy for Preparing Porous and Hollow Nanoparticles. *Langmuir* **2016**.

80.   Byrappa, K.; Yoshimura, M., *Handbook of Hydrothermal Technology*. Noyes Publications, Park Ridge, New Jersey, U.S.A: 2001.

81.   Rabenau, A., The Role of Hydrothermal Synthesis in Preparative Chemistry. *Angew. Chem., Int. Ed. Engl.* **1985,** 24, (12), 1026-1040.

7. References

82.   Schubert, U.; Hüsing, N., *Synthesis of inorganic materials, 2ⁿᵈ Ed.* Wiley-VCH: Weinheim, 2005.

83.   Mao, Y.; Park, T.-J.; Zhang, F.; Zhou, H.; Wong, S. S., Environmentally Friendly Methodologies of Nanostructure Synthesis. *Small* **2007,** 3, (7), 1122-1139.

84.   Yoshimura, M.; Byrappa, K., Hydrothermal processing of materials: past, present and future. *J. Mater. Sci.* **2008,** 43, (7), 2085-2103.

85.   Antoine, C., Tensions des vapeurs; vouvelle relation entre les tensions et les températures. *C. R. Acad. Sci.* **1888,** 107, 681-684.

86.   Kerns, W. J.; Anthony, R. G.; Eubank, P. T., Volumetric Properties of Cyclohexane Vapor. *AIChE Symp. Ser.* **1974,** 70, (140), 14-21.

87.   Bragg, W. H.; Bragg, W. L., The Reflection of X-rays by Crystals. *Proc. R. Soc. London, A* **1913,** 88, (605), 428-438.

88.   Klug, H. P.; Alexander, L. E., *X-Ray Diffraction Procedures for Polycrystalline and Amorphous Materials.* 2ⁿᵈ ed.; J. Wiley & Sons: New York, 1974.

89.   Rietveld, H., A profile refinement method for nuclear and magnetic structures. *J. Appl. Crystallogr.* **1969,** 2, (2), 65-71.

90.   Scherrer, P., Bestimmung der Größe und der inneren Struktur von Kolloidteilchen mittels Röntgenstrahlen. *Göttinger Nachrichten Math. Phys.* **1918,** 2, 98-100.

91.   Scardi, P.; Leoni, M.; Delhez, R., Line broadening analysis using integral breadth methods: a critical review. *J. Appl. Crystallogr.* **2004,** 37, (3), 381-390.

92.   Goldstein, J.; Newbury, D. E.; Joy, D. C.; Lyman, C. E.; Echlin, P.; Lifshin, E.; Sawyer, L.; Michael, J. R., *Scanning Electron Microscopy and X-ray Microanalysis.* 3ʳᵈ ed.; Springer US: 2003; p 689.

93.   Williams, D. B.; Carter, C. B., *Transmission Electron Microscopy. A Textbook for Materials Science.* Springer US: 2009; p 775.

94.   Thommes, M.; Kaneko, K.; Neimark Alexander, V.; Olivier James, P.; Rodriguez-Reinoso, F.; Rouquerol, J.; Sing Kenneth, S. W., Physisorption of gases, with special reference to the evaluation of surface area and pore size distribution (IUPAC Technical Report). In *Pure Appl. Chem.,* 2015; Vol. 87, p 1051.

95.   Brunauer, S.; Emmett, P. H.; Teller, E., Adsorption of Gases in Multimolecular Layers. *J. Am. Chem. Soc.* **1938,** 60, (2), 309-319.

96.   Sing, K. S. W.; Everett, D.; Haul, R.; Moscou, L.; Pierotti, R.; Rouquerol, J.; Siemieniewska, T., Reporting physisorption data for gas/solid systems with special reference to the determination of surface area and porosity. *Pure Appl. Chem.* **1985,** 57, (4), 603-619.

97.   Coey, J. M. D., *Magnetism and Magnetic Materials, 1ˢᵗ Ed.* Cambridge University Press: New York, 2010.

98.   Kleiner, R.; Koelle, D.; Ludwig, F.; Clarke, J., Superconducting quantum interference devices: State of the art and applications. *Proc. IEEE* **2004,** 92, 1534-1548.

99.   Gross, S.; Bauer, M., EXAFS as Powerful Analytical Tool for the Investigation of Organic-Inorganic Hybrid Materials. *Adv. Funct. Mater.* **2010,** 20, (23), 4026-4047.

100.   Bauer, M.; Bertagnolli, H., X-Ray Absorption Spectroscopy - the method and its applications. *Bunsen Magazin* **2007,** 9, 216-231.

101.   Greenwood, N. N.; Earnshaw, A., *Chemistry of the Elements.* 2ⁿᵈ ed.; Butterworth-Heinemann: 1998.

102.   Kung, H. H., *Transition Metal Oxides: Surface Chemistry and Catalysis.* Elsevier: Amsterdam, 1989.

103.   Dionne, G. F., *Magnetic oxides, 1ˢᵗ Ed.* Springer: London, 2009.

104.   Muscas, G.; Yaacoub, N.; Concas, G.; Sayed, F.; Hassan, R. S.; Greneche, J. M.; Cannas, C.; Musinu, A.; Foglietti, V.; Casciardi, S.; Sangregorio, C.; Peddis, D., Evolution of the magnetic structure with chemical composition in spinel iron oxide nanoparticles. *Nanoscale* **2015,** 7, (32), 13576-13585.

105.   Fernández-García, M.; Martínez-Arias, A.; Hanson, J. C.; Rodriguez, J. A., Nanostructured Oxides in Chemistry: Characterization and Properties. *Chem. Rev.* **2004,** 104, (9), 4063-4104.

106.   Karimi, B.; Mansouri, F.; Mirzaei, H. M., Recent Applications of Magnetically Recoverable Nanocatalysts in C-C and C-X Coupling Reactions. *ChemCatChem* **2015,** 7, (12), 1736-1789.

107.   Hudson, R.; Feng, Y.; Varma, R. S.; Moores, A., Bare magnetic nanoparticles: sustainable synthesis and applications in catalytic organic transformations. *Green Chem.* **2014,** 16, (10), 4493-4505.

108.   Casbeer, E.; Sharma, V. K.; Li, X.-Z., Synthesis and photocatalytic activity of ferrites under visible light: A review. *Sep. Purif. Technol.* **2012,** 87, 1-14.

109.   Sreekumar, K.; Sugunan, S., Ferrospinels based on Co and Ni prepared via a low temperature route as efficient catalysts for the selective synthesis of o-cresol and 2,6-xylenol from phenol and methanol. *J. Mol. Catal. A: Chem.* **2002,** 185, (1–2), 259-268.

110.   Shi, F.; Tse, M. K.; Pohl, M.-M.; Radnik, J.; Brückner, A.; Zhang, S.; Beller, M., Nano-iron oxide-catalyzed selective oxidations of alcohols and olefins with hydrogen peroxide. *J. Mol. Catal. A: Chem.* **2008,** 292, (1–2), 28-35.

111.   PalDey, S.; Gedevanishvili, S.; Zhang, W.; Rasouli, F., Evaluation of a spinel based pigment system as a CO oxidation catalyst. *Appl. Catal., B* **2005,** 56, (3), 241-250.

112.   Guin, D.; Baruwati, B.; Manorama, S. V., A simple chemical synthesis of nanocrystalline AFe_2O_4 (A = Fe, Ni, Zn): An efficient catalyst for selective oxidation of styrene. *J. Mol. Catal. A: Chem.* **2005,** 242, (1–2), 26-31.

113.   Zhang, D.-H.; Li, H.-B.; Li, G.-D.; Chen, J.-S., Magnetically recyclable Ag-ferrite catalysts: general synthesis and support effects in the epoxidation of styrene. *Dalton Trans.* **2009,** (47), 10527-10533.

114.   Florea, M.; Alifanti, M.; Parvulescu, V. I.; Mihaila-Tarabasanu, D.; Diamandescu, L.; Feder, M.; Negrila, C.; Frunza, L., Total oxidation of toluene on ferrite-type catalysts. *Catal. Today* **2009,** 141, (3–4), 361-366.

115.   Tsoncheva, T.; Manova, E.; Velinov, N.; Paneva, D.; Popova, M.; Kunev, B.; Tenchev, K.; Mitov, I., Thermally synthesized nanosized copper ferrites as catalysts for environment protection. *Catal. Commun.* **2010,** 12, (2), 105-109.

116.   Dillert, R.; Taffa, D. H.; Wark, M.; Bredow, T.; Bahnemann, D. W., Research Update: Photoelectrochemical water splitting and photocatalytic hydrogen production using ferrites (MFe_2O_4) under visible light irradiation. *APL Mater.* **2015,** 3, (10), 104001.

117.   Kim, J. H.; Kim, J. H.; Jang, J.-W.; Kim, J. Y.; Choi, S. H.; Magesh, G.; Lee, J.; Lee, J. S., Awakening Solar Water-Splitting Activity of $ZnFe_2O_4$ Nanorods by Hybrid Microwave Annealing. *Adv. Energy Mater.* **2015,** 5, (6), 1401933.

118.   Zhu, Y.; Stubbs, L. P.; Ho, F.; Liu, R.; Ship, C. P.; Maguire, J. A.; Hosmane, N. S., Magnetic Nanocomposites: A New Perspective in Catalysis. *ChemCatChem* **2010,** 2, (4), 365-374.

119.   Braga, D.; Grepioni, F., Reactions Between or Within Molecular Crystals. *Angew. Chem., Int. Ed.* **2004,** 43, (31), 4002-4011.

120.   Chinnasamy, C. N.; Narayanasamy, A.; Ponpandian, N.; Chattopadhyay, K.; Shinoda, K.; Jeyadevan, B.; Tohji, K.; Nakatsuka, K.; Furubayashi, T.; Nakatani, I., Mixed spinel structure in nanocrystalline $NiFe_2O_4$. *Phys. Rev. B: Condens. Matter* **2001,** 63, (18), 184108.

121.   Harris, V. G.; Fatemi, D. J.; Cross, J. O.; Carpenter, E. E.; Browning, V. M.; Kirkland, J. P.; Mohan, A.; Long, G. J., One-step processing of spinel ferrites via the high-energy ball milling of binary oxides. *J. Appl. Phys.* **2003,** 94, (1), 496-501.

7. References

122.   Javadi, S.; Masoudpanah, S. M.; Zakeri, A., Conventional versus microwave combustion synthesis of $CoFe_2O_4$ nanoparticles. *J. Sol-Gel Sci. Technol.* **2016,** 79, (1), 176-183.

123.   Niederberger, M.; Antonietti, M., Nonaqueous Sol–Gel Routes to Nanocrystalline Metal Oxides. In *Nanomaterials Chemistry*, Rao, C. N. R.; Müller, A.; Cheetham, A. K., Eds. Wiley-VCH Verlag GmbH & Co. KGaA: 2007; pp 119-137.

124.   Bilecka, I.; Kubli, M.; Amstad, E.; Niederberger, M., Simultaneous formation of ferrite nanocrystals and deposition of thin films via a microwave-assisted nonaqueous sol-gel process. *J. Sol-Gel Sci. Technol.* **2011,** 57, 313-322.

125.   Pinna, N.; Niederberger, M., Surfactant-free nonaqueous synthesis of metal oxide nanostructures. *Angew. Chem., Int. Ed.* **2008,** 47, 5292-5304.

126.   Modeshia, D. R.; Walton, R. I., Solvothermal synthesis of perovskites and pyrochlores: crystallisation of functional oxides under mild conditions. *Chem. Soc. Rev.* **2010,** 39, (11), 4303-4325.

127.   Zarur, A. J.; Ying, J. Y., Reverse microemulsion synthesis of nanostructured complex oxides for catalytic combustion. *Nature* **2000,** 403, (6765), 65-67.

128.   Lobachev, A. N., *Crystallization Processes under Hydrothermal Conditions, 1st Ed.* Consultants Bureau: New York, 1973.

129.   McClements, D. J., *Food Emulsions: Principles, Practices, and Techniques, Third Edition*. CRC Press: 2015.

130.   Niederberger, M.; Pinna, N., *Metal Oxide Nanoparticles in Organic Solvents - Synthesis, Formation, Assembly and Applications*. Springer: New York, 2009.

131.   Hiemenz, P. C.; Rajagopalan, R., *Principles of Colloid and Surface Chemistry*. 3rd ed.; CRC Press: New York, 1997.

132.   Carta, D.; Marras, C.; Loche, D.; Mountjoy, G.; Ahmed, S. I.; Corrias, A., An X-ray absorption spectroscopy study of the inversion degree in zinc ferrite nanocrystals dispersed on a highly porous silica aerogel matrix. *J. Chem. Phys.* **2013,** 138, (5), 054702.

133.   Boubnov, A.; Lichtenberg, H.; Mangoldc, S.; Grunwaldt, J.-D., Identification of the iron oxidation state and coordination geometry in iron oxide- and zeolite-based catalysts using pre-edge XAS analysis. *J. Synchrotron Radiat.* **2015,** 22, 410-426.

134.   Wilke, M.; Farges, F.; Petit, P.-E.; Brown, G. E.; Martin, F., Oxidation state and coordination of Fe in minerals: An Fe K-XANES spectroscopic study. *Am. Mineral.* **2001,** 86, (5), 714-730.

135.   Waychunas, G. A.; Brown, G. E.; Apted, M. J., X-ray K-edge absorption spectra of Fe minerals and model compounds: II. EXAFS. *Phys. Chem. Miner.* **1986,** 13, (1), 31-47.

136.   Nilsen, M. H.; Nordhei, C.; Ramstad, A. L.; Nicholson, D. G.; Poliakoff, M.; Cabañas, A., XAS (XANES and EXAFS) Investigations of Nanoparticulate Ferrites Synthesized Continuously in Near Critical and Supercritical Water. *J. Phys. Chem. C* **2007,** 111, (17), 6252-6262.

137.   Rouquerol, F.; Rouquerol, J.; Sing, K., *Adsorption by Powders & Porous Solids*. Academic Press: London, 1999.

138.   Bannwarth, M. B.; Camerlo, A.; Ulrich, S.; Jakob, G.; Fortunato, G.; Rossi, R. M.; Boesel, L. F., Ellipsoid-shaped superparamagnetic nanoclusters through emulsion electrospinning. *Chem. Commun.* **2015,** 51, (18), 3758-3761.

139.   Zuo, X.; Yang, A.; Vittoria, C.; Harris, V. G., Computational study of copper ferrite ($CuFe_2O_4$). *J. Appl. Phys.* **2006,** 99, (8), 08M909/1-3.

140.   Jiang, J. Z.; Goya, G. F.; Rechenberg, H. R., Magnetic properties of nanostructured $CuFe_2O_4$. *J. Phys.: Condens. Matter* **1999,** 11, (20), 4063.

141.   Guo, P.; Cui, L.; Wang, Y.; Lv, M.; Wang, B.; Zhao, X. S., Facile Synthesis of $ZnFe_2O_4$ Nanoparticles with Tunable Magnetic and Sensing Properties. *Langmuir* **2013,** 29, (28), 8997-9003.

142.   Gonzalez-Sandoval, M. P.; Beesley, A. M.; Miki-Yoshida, M.; Fuentes-Cobas, L.; Matutes-Aquino, J. A., Comparative study of the microstructural and magnetic properties of spinel ferrites obtained by co-precipitation. *J. Alloys Compd.* **2004,** 369, (1–2), 190-194.

143.   Zi, Z.; Sun, Y.; Zhu, X.; Yang, Z.; Dai, J.; Song, W., Synthesis and magnetic properties of $CoFe_2O_4$ ferrite nanoparticles. *J. Magn. Magn. Mater.* **2009,** 321, (9), 1251-1255.

144.   Espinal, L.; Suib, S. L.; Rusling, J. F., Electrochemical Catalysis of Styrene Epoxidation with Films of MnO_2 Nanoparticles and H_2O_2. *J. Am. Chem. Soc.* **2004,** 126, (24), 7676-7682.

145.   Kooti, M.; Afshari, M., Magnetic cobalt ferrite nanoparticles as an efficient catalyst for oxidation of alkenes. *Sci. Iran.* **2012,** 19, (6), 1991-1995.

146.   Pardeshi, S. K.; Pawar, R. Y., $SrFe_2O_4$ complex oxide an effective and environmentally benign catalyst for selective oxidation of styrene. *J. Mol. Catal. A: Chem.* **2011,** 334, (1–2), 35-43.

147.   Pardeshi, S. K.; Pawar, R. Y., Optimization of reaction conditions in selective oxidation of styrene over fine crystallite spinel-type $CaFe_2O_4$ complex oxide catalyst. *Mater. Res. Bull.* **2010,** 45, (5), 609-615.

148.   Rayati, S.; Zakavi, S.; Koliaei, M.; Wojtczak, A.; Kozakiewicz, A., Electron-rich salen-type Schiff base complexes of Cu(II) as catalysts for oxidation of cyclooctene and styrene with tert-butylhydroperoxide: A comparison with electron-deficient ones. *Inorg. Chem. Commun.* **2010,** 13, (1), 203-207.

149.   Berzelius, J. J., Beitrag zur näheren Kenntniss des Molybdäns. *Annalen der Physik* **1826,** 82, (4), 369-392.

150.   Fiske, C. H.; Subbarow, Y., The Colorimetric Determination Of Phosphorus. *J. Biol. Chem.* **1925,** 66, (2), 375-400.

151.   Nagul, E. A.; McKelvie, I. D.; Worsfold, P.; Kolev, S. D., The molybdenum blue reaction for the determination of orthophosphate revisited: Opening the black box. *Anal. Chim. Acta* **2015,** 890, 60-82.

152.   Keggin, J. F., The Structure and Formula of 12-Phosphotungstic Acid. *Proc. R. Soc. London, A* **1934,** 144, (851), 75-100.

153.   Smit, J. V. R., Ammonium Salts of the Heteropolyacids as Cation Exchangers. *Nature* **1958,** 181, (4622), 1530-1531.

154.   Buchwald, H.; Thistlethwaite, W. P., Some cation exchange properties of ammonium 12-molybdophosphate. *J. Inorg. Nucl. Chem.* **1958,** 5, (4), 341-343.

155.   Deng, H.; Li, Y.; Huang, Y.; Ma, X.; Wu, L.; Cheng, T., An efficient composite ion exchanger of silica matrix impregnated with ammonium molybdophosphate for cesium uptake from aqueous solution. *Chem. Eng. J.* **2016,** 286, 25-35.

156.   Cavani, F., Heteropolycompound-based catalysts:: A blend of acid and oxidizing properties. *Catal. Today* **1998,** 41, (1–3), 73-86.

157.   Patel, A., *Environmentally Benign Catalysts: For Clean Organic Reactions*. Springer Netherlands: 2013.

158.   Kozhevnikov, I. V., Catalysis by Heteropoly Acids and Multicomponent Polyoxometalates in Liquid-Phase Reactions. *Chem. Rev.* **1998,** 98, (1), 171-198.

159.   de Angelis, A.; Pollesel, P.; Molinari, D.; O'Neal Parker Jr., W.; Frattini, A.; Cavani, F.; Martins, S.; Perego, C., Heteropolyacids as effective catalysts to obtain zero sulfur diesel. *Pure Appl. Chem.* **2009,** 79, (11), 1887-1894.

160.   Cavani, F.; Etienne, E.; Mezzogori, R.; Pigamo, A.; Trifirò, F., Improvement of Catalytic Performance in Isobutane Oxidation to Methacrylic Acid of Keggin-Type Phosphomolybdates by Preparation via Lacunary Precursors: Nature of the Active Sites. *Catal. Lett.* **2001,** 75, (1), 99-105.

161.   Misono, M.; Nojiri, N., Recent progress in catalytic technology in japan. *Appl. Catal.* **1990,** 64, 1-30.

162.   Mizuno, N.; Misono, M., Heterogeneous Catalysis. *Chem. Rev.* **1998,** 98, (1), 199-218.

7. References

163.   Basu, M.; Sarkar, S.; Pande, S.; Jana, S.; Kumar Sinha, A.; Sarkar, S.; Pradhan, M.; Pal, A.; Pal, T., Hydroxylation of benzophenone with ammonium phosphomolybdate in the solid state via UV photoactivation. *Chem. Commun.* **2009**, (46), 7191-7193.

164.   Rezaei Ghalebi, H.; Aber, S.; Karimi, A., Keggin type of cesium phosphomolybdate synthesized via solid-state reaction as an efficient catalyst for the photodegradation of a dye pollutant in aqueous phase. *J. Mol. Catal. A: Chem.* **2016,** 415, 96-103.

165.   Okamoto, K.; Uchida, S.; Ito, T.; Mizuno, N., Self-Organization of All-Inorganic Dodecatungstophosphate Nanocrystallites. *J. Am. Chem. Soc.* **2007,** 129, (23), 7378-7384.

166.   He, J.; Pang, H.; Wang, W.; Zhang, Y.; Yan, B.; Li, X.; Li, S.; Chen, J., Uniform $M_3PMo_{12}O_{40} \cdot nH_2O$ (M = NH_4^+, K^+, Cs^+) rhombic dodecahedral nanocrystals for effective antibacterial agents. *Dalton Trans.* **2013,** 42, (44), 15637-15644.

167.   Mothé-Esteves, P.; Pereira, M. M.; Arichi, J.; Louis, B., How Keggin-Type Polyoxometalates Self-Organize into Crystals. *Cryst. Growth Des.* **2010,** 10, (1), 371-378.

168.   Sumner, J. B., A Method For The Colorimetric Determination Of Phosphorus. *Science* **1944,** 100, (2601), 413-414.

169.   Tazisong, I. A.; Senwo, Z. N.; He, Z., Phosphatase Hydrolysis of Organic Phosphorus Compounds. *Advances in Enzyme Research* **2015,** 03, (02), 39–51.

170.   Nelson, D. L.; Cox, M. M., *Lehninger Principles of Biochemistry*. 7th ed.; 2017; p 1328.

171.   Alcañiz-Monge, J.; Trautwein, G.; Román-Martínez, M. C., Effect of counteranion of ammonium salts on the synthesis of porous nanoparticles $(NH_4)_3[PMo_{12}O_{40}]$. *Solid State Sci.* **2011,** 13, (1), 30-37.

172.   Tangendjaja, B.; Buckle, K. A.; Wootton, M., Dephosphorylation of Phytic Acid in Rice Bran. *J. Food Sci.* **1981,** 46, (4), 1021-1024.

173.   Rocchiccioli-Deltcheff, C.; Fournier, M.; Franck, R.; Thouvenot, R., Vibrational investigations of polyoxometalates. 2. Evidence for anion-anion interactions in molybdenum(VI) and tungsten(VI) compounds related to the Keggin structure. *Inorg. Chem.* **1983,** 22, (2), 207-216.

174.   Dermeche, L.; Thouvenot, R.; Hocine, S.; Rabia, C., Preparation and characterization of mixed ammonium salts of Keggin phosphomolybdate. *Inorg. Chim. Acta* **2009,** 362, (11), 3896-3900.

175.   Cavani, F.; Teles, J. H., Sustainability in Catalytic Oxidation: An Alternative Approach or a Structural Evolution? *ChemSusChem* **2009,** 2, (6), 508-534.

176.   da Palma Carreiro, E.; Burke, A. J., Catalytic epoxidation of olefins using MoO_3 and TBHP: Mechanistic considerations and the effect of amine additives on the reaction. *J. Mol. Catal. A: Chem.* **2006,** 249, (1–2), 123-128.

177.   Deubel, D. V.; Sundermeyer, J.; Frenking, G., Mechanism of the Olefin Epoxidation Catalyzed by Molybdenum Diperoxo Complexes: Quantum-Chemical Calculations Give an Answer to a Long-Standing Question. *J. Am. Chem. Soc.* **2000,** 122, (41), 10101-10108.

178.   Wang, X.-Y.; Shi, H.-C.; Xu, S.-Y., Kinetics and mechanism on the epoxidation of *cis*-1-propenylphosphonic acid in H_2O catalyzed by tungstate(VI) or molybdate(VI). *J. Mol. Catal. A: Chem.* **2003,** 206, (1–2), 213-223.

179.   Mimoun, H., Oxygen Transfer from Inorganic and Organic Peroxides to Organic Substrates: A Common Mechanism? *Angew. Chem., Int. Ed. Engl.* **1982,** 21, (10), 734-750.

180.   Sharpless, K. B.; Townsend, J. M.; Williams, D. R., Mechanism of epoxidation of olefins by covalent peroxides of molybdenum(VI). *J. Am. Chem. Soc.* **1972,** 94, (1), 295-296.

181.   Kaplan, T. A.; Mahanti, S. D., *Physics of Manganites*. 1st ed.; Springer US: 2002; p 296.

182.   Coey, J. M. D.; Viret, M.; von Molnár, S., Mixed-valence manganites – ten years on. *Adv. Phys.* **2009,** 58, (6), 567-569.

183.   Chatterji, T., *Colossal Magnetoresistive Manganites*. 1st ed.; Springer Netherlands: Netherlands, 2004; p 447.

184.   Åsbrink, S.; Waśkowska, A.; Gerward, L.; Staun Olsen, J.; Talik, E., High-pressure phase transition and properties of spinel $ZnMn_2O_4$. *Phys. Rev. B: Condens. Matter* **1999,** 60, (18), 12651-12656.

185.   Chamberland, B. L.; Sleight, A. W.; Weiher, J. F., Preparation and characterization of $MgMnO_3$ and $ZnMnO_3$. *J. Solid State Chem.* **1970,** 1, (3), 512-514.

186.   Rui, M.; Li, X.; Gan, L.; Zhai, T.; Zeng, H., Ternary Oxide Nanocrystals: Universal Laser-Hydrothermal Synthesis, Optoelectronic and Electrochemical Applications. *Adv. Funct. Mater.* **2016,** 26, (28), 5051-5060.

187.   Saraf, L. V.; Nachimuthu, P.; Engelhard, M. H.; Baer, D. R., Stabilization of $ZnMnO_3$ phase from sol–gel synthesized nitrate precursors. *J. Sol-Gel Sci. Technol.* **2010,** 53, (2), 141-147.

188.   Rall, J. D.; Thota, S.; Kumar, J.; Seehra, M. S., Synthesis, structure, and magnetic behavior of nanoparticles of cubic $ZnMnO_3$. *Appl. Phys. Lett.* **2012,** 100, (25), 252407.

189.   Minelli, A.; Dolcet, P.; Diodati, S.; Gardonio, S.; Innocenti, C.; Badocco, D.; Gialanella, S.; Pastore, P.; Pandolfo, L.; Caneschi, A.; Trapananti, A.; Gross, S., Pursuing the stabilisation of crystalline nanostructured magnetic manganites through a green low temperature hydrothermal synthesis. *J. Mater. Chem. C* **2017,** 5, (13), 3359-3371.

190.   Credner, H., Über das Vorkommen des vanadinsauren Kupfers und des Mangankupfers bei Friedrichsrode am Thüringer Wald. *Annalen der Physik* **1848,** 150, (8), 546-558.

191.   Marquardt, M. A.; Ashmore, N. A.; Cann, D. P., Crystal chemistry and electrical properties of the delafossite structure. *Thin Solid Films* **2006,** 496, (1), 146-156.

192.   Trari, M.; Töpfer, J.; Dordor, P.; Grenier, J. C.; Pouchard, M.; Doumerc, J. P., Preparation and physical properties of the solid solutions $Cu_{1+x}Mn_{1-x}O_2$ (0⩽x⩽0.2). *J. Solid State Chem.* **2005,** 178, (9), 2751-2758.

193.   Peiteado, M.; Caballero, A. C.; Makovec, D., Phase evolution of $Zn_{1-x}Mn_xO$ system synthesized via oxalate precursors. *J. Eur. Ceram. Soc.* **2007,** 27, (13–15), 3915-3918.

194.   Peiteado, M.; Caballero, A. C.; Makovec, D., Diffusion and reactivity of $ZnO–MnO_x$ system. *J. Solid State Chem.* **2007,** 180, (9), 2459-2464.

195.   Peiteado, M.; Kodre, A.; Arčon, I.; Caballero, A. C.; Makovec, D., Structure of Spinel-Type Phases in the $ZnO–Mn_xO_y$ System. *J. Am. Ceram. Soc.* **2010,** 93, (2), 590-595.

196.   Deng, Y.; Tang, S.; Zhang, Q.; Shi, Z.; Zhang, L.; Zhan, S.; Chen, G., Controllable synthesis of spinel nano-$ZnMn_2O_4$ via a single source precursor route and its high capacity retention as anode material for lithium ion batteries. *J. Mater. Chem.* **2011,** 21, (32), 11987-11995.

197.   Zhang, G.; Yu, L.; Wu, H. B.; Hoster, H. E.; Lou, X. W., Formation of $ZnMn_2O_4$ Ball-in-Ball Hollow Microspheres as a High-Performance Anode for Lithium-Ion Batteries. *Adv. Mater.* **2012,** 24, (34), 4609-4613.

198.   Sheets, W. C.; Mugnier, E.; Barnabé, A.; Marks, T. J.; Poeppelmeier, K. R., Hydrothermal Synthesis of Delafossite-Type Oxides. *Chem. Mater.* **2006,** 18, (1), 7-20.

199.   Javed, Q.-u.-a.; Wang, F.; Toufiq, A. M.; Rafiq, M. Y.; Iqbal, M. Z.; Kamran, M. A., Preparation, Characterizations and Optical Property of Single Crystalline $ZnMn_2O_4$ Nanoflowers via Template-Free Hydrothermal Synthesis. *J. Nanosci. Nanotechnol.* **2013,** 13, (4), 2937-2942.

200.   Querejeta, A.; Varela, A.; Parras, M.; Monte, F. d.; García-Hernández, M.; González-Calbet, J. M., Hydrothermal Synthesis: A Suitable Route to Elaborate Nanomanganites. *Chem. Mater.* **2009,** 21, (9), 1898-1905.

201.   Fischer, V.; Landfester, K.; Muñoz-Espí, R., Stabilization of Calcium Oxalate Metastable Phases by Oligo(l-glutamic acid): Effect of Peptide Chain Length. *Cryst. Growth Des.* **2011,** 11, (5), 1880-1890.

202.   Preiss, L. C.; Werber, L.; Fischer, V.; Hanif, S.; Landfester, K.; Mastai, Y.; Muñoz-Espí, R., Amino-Acid-Based Chiral Nanoparticles for Enantioselective Crystallization. *Adv. Mater.* **2015,** 27, (17), 2728-2732.

7. References

203. Renz, P.; Kokkinopoulou, M.; Landfester, K.; Lieberwirth, I., Imaging of Polymeric Nanoparticles: Hard Challenge for Soft Objects. *Macromol. Chem. Phys.* **2016,** 217, (17), 1879-1885.

204. Ravel, B.; Newville, M., ATHENA, ARTEMIS, HEPHAESTUS: data analysis for X-ray absorption spectroscopy using IFEFFIT. *J. Synchrotron Radiat.* **2005,** 12, (4), 537-541.

A. List of Figures

A. List of Figures

A. List of Figures

B. List of Tables

C. Acronyms and Symbols

APM	ammonium phosphomolybdate
S	saturation level (nucleation) or specific surface area (BET method)
IP	ionic product
K_{sp}	equilibrium solubility product
ΔG	Gibbs free energy
R	universal gas constant
T	temperature
ΔG_S	surface free energy
γ	interfacial tension
r	radius
v or V	volume
ΔG_V	volume free energy
ΔG_v	free energy difference for the transition from solution to solid particle per unit volume
k	Boltzmann constant
ΔG_{crit}	critical nucleation energy
r_c	critical nucleation radius
J	nucleation rate or angular momentum (magnetization)
a	area
h	height
c	concentration
ν	number of ions per formula unit
D	diffusion coefficient
SDS	sodium dodecyl sulfate
CTAB	cetyltrimethylammonium bromide
CMC	critical micellar concentration
O/W	oil in water emulsion
W/O	water in oil emulsion
HLB	hydrophilic–lypophilic balance
P	pressure

ΔP_L	Laplace pressure
π_{osm}	osmotic pressure
n	number of moles or integer number
ρ	density
MW	molecular weight
XRD	X-ray diffraction
λ	wavelength
d	distance between parallel crystalline planes (XRD) or sample thickness (XAS) or diameter
θ	diffraction angle
I	intensity
(hkl)	Miller indices
a, b, c	crystallographic axes
α, β, γ	crystallographic angles
L	size of the coherently scattering domain (crystallite size)
K	constant of the Scherrer formula
β	full width at the half maximum (FWHM) of a reflection in the x-ray diffractogram
SEM	scanning electron microscopy
TEM	transmission electron microscopy
EDX	energy-dispersive X-ray spectroscopy
HR-TEM	high resolution transmission electron microscopy
GC	gas chromatography
MS	mass spectrometry
BET	Brunauer–Emmett–Teller
ICP	inductive coupled plasma
M	magnetization
B	magnetic flux density (also called overall magnetic field)
H	magnetic field intensity (also named magnetic field strength)
μ_0	magnetic constant
C	curie constant
SQUID	superconductive quantum interference device
XAS	X-ray absorption spectroscopy
XANES	X-ray absorption near edge structure
EXAFS	extended X-ray absorption fine structure

C. Acronyms and Symbols

$I(E)$	incident X-ray intensities
$I_0(E)$	transmitted X-ray intensities
$\mu(E)$	linear absorption coefficient
PGPR	polyglycerol polyricinoleate
ME–HP	miniemulsion under solvothermal conditions
ME	miniemulsion at ambient pressure
bulk–HP	bulk solution synthesis under solvothermal conditions
t	time
σ^2	Debye-Waller factors
R	absorber-backscatterer distance
E_0	energy correction
O_h	octahedral site
T_d	tetrahedral site
POM	polyoxometalate
APM-Na	ammonium phosphomolybdate from sodium dihydrogenphosphate
APM-NH$_4$	ammonium phosphomolybdate from ammonium dihydrogenphosphate
APM-phy	ammonium phosphomolybdate from phytic acid dodecasodium salt
APM-glu	ammonium phosphomolybdate from D-glucose-6-phosphate sodium salt
APM-ser	ammonium phosphomolybdate from O-phospho-DL-serine
APM-Na–ME	ammonium phosphomolybdate from sodium dihydrogenphosphate
APM-NH$_4$–ME	ammonium phosphomolybdate from ammonium dihydrogenphosphate
APM-phy–ME	ammonium phosphomolybdate from phytic acid dodecasodium salt
APM-glu–ME	ammonium phosphomolybdate from D-glucose-6-phosphate sodium salt
APM-ser–ME	ammonium phosphomolybdate from O-phospho-DL-serine
A	preexponential factor
k	exponential decay constant or kinetic constant
FIB	focused ion beam
FTIR	Fourier transform infrared spectroscopy
TGA	Thermogravimetric analysis
EMI-BF4	1-ethyl-3-methylimidazolium tetrafluoroborate
TBHP	*tert*-butyl hydroperoxide solution

D. Acknowledgements

E. Curriculum Vitae

Personal Information

Name	Alice Antonello
Date of Birth	10/2/1989
Place of Birth	Busto Arsizio, Italy

Education

2/2014 – 6/2017

Doctoral Candidate

Max Planck Institute for Polymer Research

Supervisors: Prof. Dr. K. Landfester, Dr. Rafael Muñoz-Espí, and Dr. Silvia Gross

10/2011 – 10/2013

Master of Science in Chemistry

Università degli Studi di Milano

Final Grade: 110/110 cum laude

Thesis: "Transparent TiO_2 Films. Wettability Modulation and Photocatalytic Activity"

Supervisors: Prof. Silvia Ardizzone and Prof. Giuseppe Cappelletti

10/2008 – 10/2011

Bachelor of Science in Chemistry

Università degli Studi di Milano

Final Grade: 110/110 cum laude

Thesis: "Determination of the Surface Free Energy of Siloxane Films and Their Employment to Functionalize TiO_2"

Supervisors: Prof. Silvia Ardizzone and Prof. Giuseppe Cappelletti

9/2003 – 7/2008

Scientific High School Degree

Liceo Scientifico "Marie Curie", Tradate

Final Grade: 98/100

F. Scientific Contributions

F1. Publications

Antonello, A.; Soliveri, G.; Meroni, D.; Cappelletti, G.; Ardizzone, S., Photocatalytic remediation of indoor pollution by transparent TiO_2 films. *Catal. Today* **2014**, 230, 35-40.

Antonello, A.; Jakob, G.; Dolcet, P.; Momper, R.; Kokkinopoulou, M.; Landfester, K.; Muñoz-Espí, R.; Gross, S., Synergy of Miniemulsion and Solvothermal Conditions for the Low-Temperature Crystallization of Magnetic Nanostructured Transition-Metal Ferrites. *Chem. Mater.* **2017**, 29, (3), 985-997.

Antonello, A.; Benedetti, C; Kokkinopoulou, M; Kirchhoff, K; Fischer, V; Landfester, K.; Gross, S; Muñoz-Espí, R., Colloidally Confined Crystallization of Ammonium Phosphomolybdate Catalysts from Organic and Inorganic Phosphate Sources *(in prepration)*.

Benedetti, C.; Flouda, P; **Antonello, A.**; Rosenauer, C.; Pérez-Pla, F.F.; Landfester, K.; Gross, S.; Muñoz-Espí, R., Zirconium Oxocluster/Polymer Hybrid Nanoparticles Prepared by Photoactivated Miniemulsion Copolymerization *(submitted)*.

Antonello, A.; Benedetti, C; Landfester, K.; Gross, S; Muñoz-Espí, R., Crystallization of Transition Metal Manganites in Miniemulsion–Solvothermal Conditions *(in preparation)*.

Benedetti, C.; Kokkinopoulou, M.; Jo, S.-M.; **Antonello, A**.; Rosenauer, C.; Landfester, K.; Gross, S.; Muñoz-Espí, R., Hybrid Cross-Linked Nanocapsules with Zirconium Oxocluster as Galileo-like Nano-Thermometer *(in preparation)*.

F2. Conferences

Oral presentation "Exploring the Combination of Miniemulsion and Solvothermal Conditions for the Low Temperature Synthesis of Catalytically Active Transition Metal Ferrites" at the "**Congresso Nazionale di Chimica Inorganica**" in Padova, September 2016.

Poster presentation "Synergic Combination of Miniemulsion and Solvothermal Routes for the Synthesis of Highly Crystalline Transition Metal Ferrites" at the **"European Colloid and Interface Society Conference" (ECIS)** in Rome, September 2016.

Poster presentation "Complex Inorganic Systems in the Confined Space of Miniemulsion Droplets" at the **"European Winter School on Physical Organic Chemistry"** **(E-WiSPOC)** in Bressanone, February 2015.